

Dynamics of Granular Material on Small Bodies

Von der Fakultät für Elektrotechnik, Informationstechnik, Physik
der Technischen Universität Carolo-Wilhelmina zu Braunschweig

zur Erlangung des Grades eines
Doktors der Naturwissenschaften (Dr. rer. nat.)

genehmigte Dissertation

von Marc Hofmann

aus Pinneberg

eingereicht am: 11.07.2014

Disputation am: 29.09.2014

1. Referent: Prof. Dr. Jürgen Blum
2. Referent: Prof. Dr. Jürgen Oberst

Druckjahr: 2014

Bibliografische Information der Deutschen Nationalbibliothek

Die Deutsche Nationalbibliothek verzeichnet diese Publikation in der Deutschen Nationalbibliografie; detaillierte bibliografische Daten sind im Internet über <http://dnb.d-nb.de> abrufbar.

1. Referentin oder Referent: Prof. Dr. Jürgen Blum
 2. Referentin oder Referent: Prof. Dr. Jürgen Oberst
- eingereicht am: 11.07.2014
Disputation am: 29.09.2014

Dissertation an der Technischen Universität Braunschweig,
Fakultät für Elektrotechnik, Informationstechnik, Physik

ISBN 978-3-944072-08-1

uni-edition GmbH 2014

<http://www.uni-edition.de>

© Marc Hofmann



This work is distributed under a
Creative Commons Attribution 3.0 License

Printed in Germany

Contents

Zusammenfassung	9
Abstract	11
1 Introduction	13
1.1 Why study asteroids?	13
1.2 Asteroids in the context of this work	13
2 Regolith	15
2.1 Definition	15
2.2 Genesis	15
2.3 Space weathering	16
2.4 Regolith in the Solar System	17
2.4.1 Moon	17
2.4.2 Asteroids	18
2.4.3 Comets	18
3 Avalanches	19
3.1 Characteristics of Granular Material	19
3.1.1 Angle of repose	19
3.1.2 Dilatancy	20
3.1.3 Friction	20
3.2 Granular material in space	21
3.2.1 Lack of interstitial fluid	21
3.2.2 Possible deprivation of small particles	21
3.3 Possible trigger mechanisms for avalanches on small bodies	22
4 ROSETTA	25
4.1 The Mission	25
4.2 OSIRIS	27
4.3 (21) Lutetia	28
4.3.1 (21) Lutetia - Pre fly-by	28
4.3.2 (21) Lutetia - Post fly-by	29
4.3.2.1 Physical and orbital properties	30
4.3.2.2 Geography	31
4.3.2.3 Cratering History	31
4.3.2.4 Regolith and granular flow on (21) Lutetia	34

5	Experiments on Avalanche Triggering	35
5.1	Introduction	35
5.2	Material Analysis	36
5.2.1	HED	36
5.2.2	JSC MARS-1 Martian Soil Simulant	37
5.2.3	Determining the angle of repose	37
5.3	Experimental Campaign	38
5.3.1	Accomplishing low gravity	39
5.3.2	Design of the experiment	41
5.3.3	Schedule	44
5.3.4	Data analysis	45
5.3.5	Results	50
5.3.5.1	Avalanche Dynamics	50
5.3.6	Performance	53
5.3.6.1	Mechanical limitations	53
5.3.6.2	Cannon induced vibrations	53
5.4	Importance of minor impact events	56
6	Simulations of Avalanches	61
6.1	DEM Simulation	61
6.2	Setup of Simulation Environment	62
6.3	Analysis	66
6.3.1	Description of analysis variables	67
6.3.1.1	Energy time series	67
6.3.1.2	Energy depth histogram and penetration depth	67
6.3.1.3	Mean velocity vector	69
6.3.1.4	Energy surface density	70
6.3.1.5	Porosity	72
6.4	Results	73
7	Summary and conclusions	79
8	Outlook	81
A	Appendix - Experiments on Avalanche Triggering	83
A.1	Details on experimental campaigns	83
A.2	The smoothing algorithm	98
	Bibliography	101
	Publications	111
	Acknowledgements	113
	Curriculum Vitae	115

List of Figures

3.1	Tumbler	20
4.1	Trajectory of ROSETTA	26
4.2	(2867) Šteins as imaged by OSIRIS	27
4.3	(21) Lutetia	29
4.4	ROSETTA- (21) Lutetia-distance and phase angle	30
4.5	(21) Lutetia geological map	32
4.6	The North Polar Crater Cluster	33
5.1	HED grains	36
5.2	Mass fraction of the HED and MARS-1	38
5.3	Time series of a tumbler experiment	38
5.4	Exemplary distribution of the angle of repose/rest	39
5.5	ZARM facility	40
5.6	Photos of the experimental setup	41
5.7	Cannon used to accelerate the impactor	42
5.8	Calibration plot of the magnet cannon for a 2 mm-sized impactor.	42
5.9	Variation of centrifugal force	43
5.10	Effect of Coriolis force	44
5.11	Difference images	46
5.12	Noise for the <i>HB</i> -Campaign	47
5.13	Signal strength in difference images	48
5.14	Rotated image with crop outlines for mirror (dotted box) and direct (dash-dotted box) view.	49
5.15	Smoothing results for better area estimation	49
5.16	Exemplary time series of surface area covered with moving grains	50
5.17	Avalanche occurrence (MARS-1)	51
5.18	Avalanche occurrence (HED)	52
5.19	Exponential fit to box plot	54
5.20	Smoothing results for better area estimation	55
5.21	Range of impact ejecta	57
5.22	Monte Carlo simulations of impact events triggering avalanches	58
5.23	Impact histograms for the Monte Carlo simulations	59
5.24	Mean number of impacts per m ² for different resurfacing ratios and distances to the ridge	59

5.25	Mean number of impacts per m ² for 100% resurfacing ratio as a function of the distance from the ridge	60
6.1	Histograms for <i>RadomBoxPacker</i>	62
6.2	Mass fractions for MARS-1 and <i>RandomBoxPacker</i>	63
6.3	Depth histograms for particle mixture	64
6.4	Influence of wall friction on the particle dynamics	65
6.5	Impact geometry	66
6.6	Exemplary time series of energy of the target and the impactor and the sum of both	68
6.7	Exemplary energy-depth-histogram	69
6.8	Exemplary mean velocity change over time	70
6.9	x and z coordinates for particles in an exemplary surface layer	71
6.10	Projection of a sphere with a fixed energy density onto a plane	72
6.11	Resulting exemplary energy area density field.	73
6.12	Comparison of energy	74
6.13	Number of neighbors in the target block	74
6.14	Comparison of energy penetration depth	76
6.15	Comparison of mean downhill velocity in the surface layer	77
6.16	Comparison of the semimajor axis of the 10 ⁻⁴ energy contour	78
A.1	Determining the area of the avalanche	99

List of Tables

4.1	Orbital and physical parameters of (21) Lutetia from ground based observations.	28
4.2	Physical parameters of (21) Lutetia from OSIRIS and RSI measurements .	30
4.3	Ages of geological units from crater size frequency distribution	32
5.1	Diameter ranges used in the experiments with MARS-1.	37
5.2	Measured static angle of repose and angle of rest.	39
5.3	The change in centrifugal acceleration due to different distances from the rotation center for different positions on the granular surface.	44
5.4	Details on the different Seasons of the Experimental Campaign	45
5.5	Avalanche frequency for the different sievings of the MARS-1 material for tilt angles between 40° and 50°	53
6.1	Diameter ranges used to create the particle mixing.	63
A.1	Details on the <i>HB</i> -Campaign (HED).	83
A.2	Details on the <i>HB</i> -Campaign (MARS-1).	84
A.3	Details on the <i>BS-1</i> -Campaign.	85
A.4	Details on the <i>BS-2</i> -Campaign.	86
A.5	Details on the <i>BS-3</i> -Campaign.	87
A.6	Details on the <i>BS-4</i> -Campaign.	88
A.7	Continued: Details on the <i>BS-4</i> -Campaign.	89
A.8	Details on the <i>BS-5</i> -Campaign.	90
A.9	Continued: Details on the <i>BS-5</i> -Campaign.	91
A.10	Details on the <i>BS-6</i> -Campaign.	92
A.11	Continued: Details on the <i>BS-6</i> -Campaign.	93
A.12	Details on the <i>BS-7</i> -Campaign.	94
A.13	Continued: Details on the <i>BS-7</i> -Campaign.	95
A.14	Details on the <i>BS-8</i> -Campaign.	96
A.15	Continued: Details on the <i>BS-8</i> -Campaign.	97

Zusammenfassung

Die ROSETTA Sonde der Europäischen Raumfahrtorganisation ESA startete im Jahre 2004 zu ihrer Mission: der Untersuchung des Kometen 67P/Tschurjumow-Gerasimenko, die mit dem Rendezvous-Manöver im August 2014 in die Hauptphase eintreten wird. Auf dem Weg zum Kometen passierte die Sonde am 10. Juli 2010 den Asteroiden (21) Lutetia. Dabei näherte sich die Sonde dem Asteroiden bis auf 3170 km. Das Kamera-System der Sonde, OSIRIS (*Optical, Spectroscopic, and Infrared Remote Imaging System*), machte während des Vorbeiflugs 462 Photoaufnahmen. Dabei kamen 21 breitband und schmalband Filter zum Einsatz, welche einen Wellenlängenbereich zwischen 240 und 1000 nm abdeckten.

Anhand der Daten die von der Sonde gesammelt wurden, fand man heraus, dass (21) Lutetia von einer Schicht aus Regolith bedeckt ist, die teilweise mehrere Hundert Meter dick ist. An einigen Kraterhängen ließen sich lawinenartige Abrutsche erkennen. Ein möglicher Auslösemechanismus für solche Lawinen in niedriger Schwerkraft ist der Einschlag von langsamen Partikeln in einem Größenbereich von mm bis cm.

Es wurde ein Experiment durchgeführt, in dem Proben körniger Materialien zunächst auf verschiedene Kippwinkel (relativ zum Gravitationsvektor) geneigt wurden. Dann wurde eine 2 mm durchmessende Metallkugel auf Geschwindigkeiten von bis zu 2 m/s beschleunigt und in das granulare Medium geschossen. Die so erzeugten Einschläge wurden mit Hilfe einer Hochgeschwindigkeitskamera gefilmt, um die Auswirkungen dieser Einschläge zu untersuchen.

Das Experiment wurde am Fallturm des *Zentrum für angewandte Raumfahrttechnik und Mikrogravitation* (ZARM) in Bremen durchgeführt. Dort wurde der Aufbau in einem Vakuumgefäß platziert und auf einer Zentrifuge befestigt, sodass durch die Drehbewegung der Zentrifuge eine Beschleunigung simuliert werden konnte, die der auf einem Asteroiden gleicht.

Zwanzig der oben beschriebenen Experimente wurden durchgeführt, wobei der Neigungswinkel des Materials und die künstliche Gravitation variiert wurden. Untersucht wurden zwei Materialien: ein zermahlener HED Meteorit und das JSC MARS-1, ein Analogmaterial zum Mars-Sand. Zusätzlich dazu wurden weitere Experimente bei normaler Schwerkraft durchgeführt.

Die aufgenommenen Bilder wurden mit Hilfe eines Differenzbildverfahrens analysiert, das es erlaubt Bewegungen besser zu verfolgen. In weiteren Untersuchungsschritten wurde die Reaktion des Materials auf den Einschlag, sowohl an der Oberfläche wie auch in tieferen Schichten, untersucht. Dabei wurde auf den Einfluss der Schwerebeschleunigung, des Neigungswinkels und der Einschlagsgeschwindigkeit geachtet.

Die Analyse der Experimente ergab, dass kleinskalige Einschläge, unter bestimmten Voraussetzungen, in der Lage sind, sowohl unter normaler, als auch unter reduzierter

Schwerkraft, Lawinen auszulösen. Die Wahrscheinlichkeit im MARS-1 Material eine Lawine auszulösen ist dabei abhängig davon, wie grob das Material gesiebt wurde.

Mit Hilfe einer Monte-Carlo-Simulation wurde zudem gezeigt, dass Lawinen mit dem im Experiment beobachteten Länge-zu-Breite-Verhältnis in der Lage sind eine $1 \times 1 \text{ m}^2$ große Fläche, die sich genügend weit unterhalb des Kamms eines ausreichend steilen Hangs befindet, zu bedecken, wenn die Einschlagsdichte der hier betrachteten Teilchen Sieben Einschläge pro Quadratmeter erreicht. Die Häufigkeit kleiner Einschläge in dem hier betrachteten Geschwindigkeitsintervall ist nicht genau bekannt. Eine Abschätzung dessen ist möglich, wenn man als Grundlage den Fluss von Teilchen geringer Masse in Erdnähe und die Erzeugung von Auswurfprodukten bei Experimenten mit Hochgeschwindigkeitseinschlägen heranzieht. Man erhält eine Zeitspanne von Hunderttausend Jahren, bis die genannte Einschlagsdichte erreicht ist.

Die mikrophysikalischen Prozesse während eines kleinskaligen Einschlags wurden mit Hilfe der so genannten *Discrete Element Method* (DEM) untersucht. Dazu wurde die Software *ESyS-Particle* benutzt. DEM Codes simulieren granulare Systeme als Ensemble sphärischer Teilchen die mit externen Kräften und miteinander Wechselwirken können. Die oben beschriebenen Experimente wurden mit Hilfe der Software simuliert. Dabei wurde die Größe des simulierten Volumens verringert, um den Rechenaufwand zu verringern.

Die Ergebnisse zeigen, dass die Energie, die durch den Einschlag in das System eingebracht wird, größtenteils in Partikeln, die sich an der Oberfläche befinden, verbleibt. Die Energie wird durch inelastische Stöße zwischen den Körnern des Target-Materials dissipiert. Diese Stoßprozesse geschehen häufiger in tieferen Schichten des Materials, wo die mittlere Zahl von Stoßpartnern höher ist als an der Oberfläche. Die Energie, die in der Oberflächenschicht verbleibt, wird vom Einschlagspunkt ausgehend radialsymmetrisch verteilt. Für einen hohen Wert von g wird dieser Prozess von der Gravitation dominiert, für kleine Werte von g spielt die Geometrie der Teilchen im Target die größere Rolle.

Diese Erkenntnisse bestätigen den Schluss, dass kleinskalige Einschläge, sowohl in reduzierter wie auch in normaler Schwerkraft, geeignet sind, Erdbeben und Lawinen auszulösen.

Abstract

The European Space Agency's ROSETTA spacecraft was launched in 2004 and will rendezvous with comet 67P/Churyumov-Gerasimenko in August 2014. On its route towards the comet, it flew by asteroid (21) Lutetia on 10 July 2010, with a closest approach distance of 3170 km. OSIRIS - the *Optical, Spectroscopic, and Infrared Remote Imaging System* on board Rosetta - took 462 images of Lutetia, using 21 broad- and narrow band filters covering a wavelength range from 240 to 1000 nm.

The surface of (21) Lutetia is covered with a thick layer of regolith. On slopes of several craters this regolith layer collapsed in landslide-like events. A possible trigger mechanism for these low-gravity avalanches is the slow impact of a small mm to cm-sized body.

An experiment was conducted where samples of different granular materials were tilted at different angles with respect to the vector of gravity. We accelerated a small mm-sized metal sphere to velocities up to 2 m/s and shot it into the sloped granular material. The impacts and any events triggered by the impact were recorded using a high-speed high-resolution camera.

The experiment was implemented at the *Center of Applied Space Technology and Microgravity (ZARM)* vacuum drop tower in Bremen in August 2012. The experiment was placed in an evacuated cylinder and mounted on a centrifuge that was spun with varying rotation rates to accommodate the vacuum and low gravity present on the surfaces of asteroids.

A total of 20 experiments as described above were realized during 10 drops. The tilt angle and the magnitude of artificial gravity were varied for two different materials, a ground HED meteorite and the JSC MARS-1 Martian soil simulant. Additional ground-based experiments in 1g environment were conducted at a later time.

The images were analyzed using an image subtraction algorithm to track movement from one frame to the next. In subsequent steps the behavior of the material on the surface as well as in deeper layers were observed to characterize the effects of the impact with changing gravitational acceleration, impactor velocity and tilt angle of the material.

The analysis of the experimental data indicates that small scale impacts can, under certain conditions, trigger avalanches in both normal and reduced gravity. The probability to induce an avalanche in the MARS-1 material is lower for coarser sievings.

Monte Carlo simulations show that landslides with the length-to-width ratio observed in the experiments could serve to resurface a unit area of $1 \times 1 \text{ m}^2$ on a high-tilt slope that is sufficiently far below the ridge after 7 impact events per square meter. The flux of impactors in the considered size and velocity regime is not well constrained. Estimations on the time scale can be done by assuming a high-speed low-mass impactor flux similar to the Earth's and ejecta creation factors from high-speed impact experiments. The results suggest that these 7 events could be reached on (21) Lutetia within about 10^5 yr.

To gain a better understanding the microphysical processes governing the distribution of energy in low-energy impacts, a suite of simulations was performed, using a *Discrete Element Method* (DEM) software called *ESyS-Particle*. DEM codes simulate granular systems by creating an ensemble of spherical particles that interact with external forces and with one another. The experiments described above were recreated within the program in a reduced size to make the calculations less computationally demanding.

The results show that energy introduced into the target material by the impactor is largely retained at the surface of the target. The energy gets dissipated in inelastic collisions that happen more frequently in the depth of the material where the mean number of contacts per particle is higher than at the surface. The energy retained at the surface gets distributed radially away from the impact site. This distribution can be governed by gravity (when g is large) or the local arrangement of the particles (when gravity is low).

These findings reinforce the conclusion that low-energy impacts are a viable trigger mechanism for avalanches, both in low and normal gravity.

1 Introduction

1.1 Why study asteroids?

The main asteroid belt, situated between about 2.0 and 3.4 au¹, contains more than a million small bodies of size larger than 1 km (Tedesco and Desert 2002) but contains a mass of only $6 \cdot 10^{-4} M_{\text{Earth}}$ (Krasinsky *et al.* 2002).

While the Titius-Bode-Law predicts the existence of a large mass concentration at about 2.8 au, no body was known at that heliocentric distance until the discovery of (1) Ceres by Piazzi (1802).

The newly discovered body was thought to be a planet and only after several more bodies were found in the space between Mars and Jupiter, Herschel (1802) suggested that these bodies should not be termed planets but *asteroids*, after the Greek word *Ἀστεροειδής* (*asteroides*, meaning “star-like”), because of their much smaller size.

By now a large number of small bodies has been found, not only in the main asteroid belt but in large parts of the solar system, including near-Earth space.

Asteroids are an important field of study, as it is believed that they represent a relatively pristine sample of the conditions in the proto-planetary disk (PPD). Modeling by Morbidelli *et al.* (2012) suggests that the planetesimals that formed in the region of the current main belt did not further accrete into a larger planetary body because of the disturbing influence of Jupiter and Saturn. Their evolution stopped thus very early in the process of planet formation and so they contain a record of the state of the PPD during this early phase of solar system formation.

1.2 Asteroids in the context of this work

The evolution of asteroids is largely governed by inter-asteroidal impacts that can reshape, fracture or disrupt the body. But other factors, like space weathering, can influence a small but important part of an asteroid: the superficial layer of regolith.

All asteroids that have been visited by spacecraft have been found to retain a layer of regolith on their surfaces (e.g. Veverka *et al.* 1994, Belton *et al.* 1996, Sierks *et al.* 2011) and modeling (Housen and Wilkening 1982) and remote sensing measurements (Gundlach and Blum 2013) suggest that this state is representative of the entire asteroid belt.

¹One astronomical unit (au) is the mean Sun-Earth distance, fixed by the IAU to have a value of 149 597 870 700 m.

The surface of an asteroid is the part of the body that is most easily probed by remote sensing. Understanding the dynamics and evolution of the surface covering regolith is thus key to interpret any finding from Earth- or spacecraft-based investigation. The processes responsible for the creation and evolution of regolith on small bodies will be discussed in chapter 2.

The way asteroids are seen through remote sensing efforts is strongly depending on the age of the regolith covering their surface. Any process that can alter the appearance of the body needs to be understood in order to correctly interpret remotely gathered findings.

Avalanches are a common sight on small bodies. Apart from locally changing the topography of their host body, they also mix and stir up the regolith bringing fresh or less weathered material to the top. The physical processes and interactions that govern avalanches as well as the most important trigger mechanisms for avalanches will be reviewed in chapter 3.

The ROSETTA mission, currently orbiting the comet 67P/Churyumov-Gerasimenko flew by two main belt asteroids, (2867) Šteins and (21) Lutetia, and collected a large dataset on both bodies. This work has been done in the framework of the ROSETTA-OSIRIS team, thus a detailed description of the the ROSETTA mission will be given in chapter 4.

As previously stated, avalanches play a significant role in the context of temporal change of the surfaces of asteroids. It is key to understand not only the dynamics of avalanches and landslides but also to find the relative importance of different trigger mechanisms that can start landslides on small bodies. This will help assess the timescales over which the processes act and to evaluate the importance for remote sensing efforts.

One particular potential trigger mechanism for avalanches is the slow impact of small particles. The effectiveness and possible importance of this process is investigated in chapter 5.

The experimental data are augmented through the use of *Discrete Element Method* computer simulations that address the question of the microphysical processes operation during a low velocity small scale impacts. The results of these are described in detail in chapter 6.

2 Regolith

A lot of research is focusing on regolith, which can be found on the surface of almost every solar system object. This thesis is concerned with the regolith covering airless bodies in the main asteroid belt. Therefore any influence of an atmosphere or liquid on the formation or alteration of regolith shall be neglected. While the definition of regolith is universal regardless of the parent body, the generation processes and modes of modification over time differ significantly for bodies with or without atmosphere.

2.1 Definition

Regolith is a “superficial layer or blanket of loose particulate rock material found on planet earth or any other hard celestial object” (Fairbridge 1967). By this definition almost every body in the solar system has a layer of regolith covering its surface. This particulate or granular material can be of different size, depth and composition depending on the body it resides upon and the history of its creation and evolution.

Regolith has a range of grain sizes from micrometer sized dust to ejecta blocks of up to several hundreds meters (e.g. Thomas *et al.* 2000, Sullivan *et al.* 2002, Sierks *et al.* 2011). It is comprised of grains (fractured rock) and agglutinates (glass from impact melting of grains) (Lee 1997).

Based on astronomic measurements it has long been speculated that asteroids might be covered by a regolith (e.g. Dollfus 1971, Jurgens and Goldstein 1976). While the production and retention of regolith on the surfaces of asteroids had been the subject of theoretical work since the 1970s (e.g. Chapman 1972, 1976, Housen *et al.* 1979) the first direct confirmation of its existence was not until the Galileo fly-by at (951) Gaspra in 1991 (Veveřka *et al.* 1994) and (243) Ida in 1993 (Belton *et al.* 1996).

2.2 Genesis

The creation of regolith is a very dynamic process and shall be described in a greater detail in this section.

Assume a solar system object without an atmosphere that is made up of a monolithic rock. This rock will be impacted by other solar system objects. These impactors will have different sizes and velocities. Assume further that these impacts will not destroy¹ the primary object, meaning that the impactors do not exceed a critical velocity or mass.

¹A body will be considered as shattered or destroyed, if the largest remaining fragment has less than half of the mass of the primary object.

The collisional lifetime of an asteroid (the time before it gets disrupted by an impact) can be calculated. Bottke *et al.* (1994) compute the collisional lifetime of a 200 km sized main belt object to be larger than the age of the solar system. This lifetime will become shorter for smaller objects.

Nevertheless, before a body gets catastrophically disrupted it will be subject to numerous non-disrupting impacts. Any of these impacts will excavate material with a given velocity distribution. Any matter with a speed exceeding the escape velocity

$$v_{\text{escape}} = \sqrt{\frac{2GM}{r}} \quad (2.1)$$

where M is the mass of the parent body, r is the distance from the barycenter of the parent body, and G is the gravitational constant, will be lost to the parent body. Ejecta with a speed below the escape velocity, however, will eventually fall back onto the surface.

The relative velocity of bodies in the present asteroid belt is of the order 5 km/s (Bottke *et al.* 1994), while the relative velocities in the early solar system were well below that, allowing for easier retention of impact ejecta on small bodies as slow impacts create low-velocity ejecta (Armitage 2010).

The retained part of the impact ejecta will cover an increasing fraction of the body's surface until such a point in time where the entire body is covered. Following impacts will then not only excavate bedrock material but also affect ejecta from older impacts.

While the bedrock gets eroded by this process the thickness of the regolith layer increases. Impact experiments suggest that a pre-existing regolith layer favors the retention of impact ejecta rather than a depletion of the regolith (Stöffler *et al.* 1975, Hartmann 1978).

The regolith layer can become so deep that impacts below a given size (or to be more precise: below a given energy) can no longer penetrate it, at which point no new regolith is produced anymore. Further impacts will then only serve to comminute and garden the existing regolith (Housen *et al.* 1979).

Theoretical modeling predicts that asteroids of the size of (21) Lutetia could accumulate a regolith layer that is several kilometers thick (Housen *et al.* 1979). Direct observations by the ROSETTA spacecraft resulted in an estimation of the thickness of the regolith layer of about 600 m (Vincent *et al.* 2012).

Delbo *et al.* (2014) suggest that break up of rock caused by thermal fatigue should be the main regolith production mechanism on small asteroids and should also play a role in the regolith formation on asteroids of any size.

2.3 Space weathering

The term space weathering refers to a number of different processes that can change

- the physical structure,
- the chemical properties,
- the mineralogical properties,
- the optical properties

of the surface of an airless body. Since the surface is the one part of a body that is exposed to remote sensing efforts, its alteration by space weathering can therefore impede the efforts of understanding its nature (Clark *et al.* 2002).

Processes that are subsumed under the term *space weathering* include (Chapman 2004)

1. Impingement of solar and galactic cosmic rays
2. Impacts of small meteorites and micrometeorites
3. Solar irradiation

and can introduce new elements and chemical compounds into the surface material in a direct manner, create a thin, vapor-deposited coating on the surface particles (Pieters *et al.* 2000) or change the ratio of grains to glass (which, for example, is $\leq 50\%$ by volume for the moon (Lee 1997)).

Consequences that are observable by remote sensing include an overall lower albedo, a reddening of the spectrum and reduction in the band depth and slope of different spectral absorption features.

Space weathering could explain the so-called “S-type conundrum”, the fact that the most common asteroid type (S-type) has no meteorite class with a matching spectrum while the most common meteorites (ordinary chondrites, *OC*) appear to have no spectral parent body in the asteroid belt. This mismatch could be resolved if space weathering changed the spectral signature of *OC* asteroids to look like an S-type (Chapman 2004).

The degree to which a surface is altered by space weathering will depend on the time since the last resurfacing event (e.g. major impact) and its heliocentric distance (as the solar radiation can play a major role in the space weathering process).

2.4 Regolith in the Solar System

2.4.1 Moon

The Lunar regolith is by far the best studied extraterrestrial regolith. The close proximity to the Earth allows for detailed remote sensing studies as well as in situ measurements through the Apollo missions and other lander and sample return missions.

The regolith layer covering the lunar surface is thought to have a thickness 5 – 10 m in the *mare* regions and may be even deeper in the highlands (Quaide and Oberbeck 1968).

The grain size ranges from micron sized particles to boulders of several tens of meters with most of the particles being less than 1 mm in diameter. The median particle diameter is 40 – 130 μm . The lunar regolith is deficient in particles below 1 μm yet 10-25% of the mass is concentrated in particles below 20 μm in diameter (Lee 1995).

The grains consist of minerals (mostly basalt in the mare regions and *breccia*² in the highlands) or glass (Housen and Wilkening 1982).

The bulk density of the material was determined from Apollo samples to be (1500 \pm 50) kg/m^3 with a porosity of (35 \pm 3)%. The angle of repose is estimated to be between 35° and 40° (Heiken *et al.* 1991, Lee 1995).

²*Breccia* consists of fragmented rocks or minerals that are embedded in a fine-grained matrix.

2.4.2 Asteroids

As described in section 2.1, the existence of regolith on asteroidal surfaces has been directly proven by the Galileo spacecraft in the 1990s. The knowledge about the properties of asteroidal regolith has been increased by ongoing investigations ever since.

By now there have been a large number of missions dedicated to study asteroids and their surfaces. A few missions stand out of the list:

- The NEAR Shoemaker mission to (433) Eros was the first mission dedicated to study an asteroid and yielding images with a resolution of up to 1 cm/px during its descent upon the surface (Veverka *et al.* 2001b). Images taken during a low-altitude fly-over show a mixture of fine grains with larger blocks (Veverka *et al.* 2001a).
- The Hayabusa sample return mission to asteroid (25143) Itokawa photographed the surface at a resolution of 6 mm/px (Miyamoto *et al.* 2007).
- The ROSETTA mission to comet 67P/Churyumov-Gerasimenko flew by two main belt objects and yielded high quality scientific data about (2867) Šteins and (21) Lutetia (Keller *et al.* 2010, Sierks *et al.* 2011).

The existence and abundance of asteroidal regolith spanning several orders of magnitude in size have been impressively proven by these missions.

Yet, the properties of the grains can only locally be studied with these high resolution images. Global properties are derived from remote sensing data with the help of theoretical modeling. E.g. Gundlach and Blum (2013) calculated the mean grain size of the regolith covering different bodies from the measured thermal inertias. They find a coarser average grain size for bodies with smaller gravitational acceleration. They argue that low mass (small) impact ejecta gain the highest velocities during an impact event and are thus preferentially lost on bodies with lower gravity.

2.4.3 Comets

Theoretical modeling predict the existence of a regolith on cometary surfaces with grain sizes ranging in the centimeter and decimeter regime (Möhlmann 1994).

The Deep Impact mission collided a 364 kg impactor consisting of 49% copper with the nucleus of comet 9P/Tempel (Tempel 1) excavating parts of the surface. The analysis of the impact led to the conclusion that the nucleus is covered with 1 – 100 μm sized particles of negligible strength (A'Hearn *et al.* 2005). The cometary dust samples collected by the Stardust spacecraft at comet 81P/Wild 2 had a similar size range (Hörz *et al.* 2006). Findings from the EPXOXI mission to comet 103P/Hartley found icy chunks of 1 to 15 cm radius and larger dirty chunks of up to 150 cm (A'Hearn *et al.* 2011).

These findings point to a rather fine grained cometary regolith that could be intermixed with larger grains.

3 Avalanches

It is important to understand the physical processes governing the behavior of granular material to correctly interpret results from experiments and simulations. This chapter will provide an overview of the quantities characterizing granular matter, both in the microscopic and the macroscopic regime.

We will define an avalanche as the flow of particulate material down a slope that can be triggered by any process and that is self amplifying without any outside driving force other than gravity and that will cease when a given predetermined criterion is met (see below for details).

3.1 Characteristics of Granular Material

3.1.1 Angle of repose

The critical angle of repose ϑ_c of a granular material is that angle towards which the material can be tilted before it will fail by avalanching. The material will stop avalanching when the angle between the surface and the horizontal arrives at the angle of rest ϑ_r (Carriquiry 1970). The tilt angle of particulate material falls into one of three categories:

1. $\vartheta < \vartheta_r$ If the tilt angle lies below the angle of rest, the material will not avalanche.
2. $\vartheta_r < \vartheta < \vartheta_c$ If the tilt angle lies between the angle of rest and the angle of repose, the slope is meta stable, i.e. any outside force strong enough to agitate a large enough portion of the material can trigger an avalanche.
3. $\vartheta_c < \vartheta$ If the tilt angle lies above the angle of repose the slope is unstable and the material will avalanche without outside interference.

Both ϑ_c and ϑ_r can be conveniently measured by the use of a so called *tumbler*; a drum partly filled with the material under investigation, slowly rotating around its symmetry axis as is shown in figure 3.1(a).

By rotating the drum at a very low frequency the change of the angle of the material is quasi-static. When the slope angle exceeds ϑ_c the material will start to flow and this flow will cease when the slope reaches ϑ_r . This process is recorded with a camera. The slope angle as a function of time will have the shape of a sawtooth wave with a ramp that corresponds to the rotation frequency of the drum (compare to figure 3.1(b)).

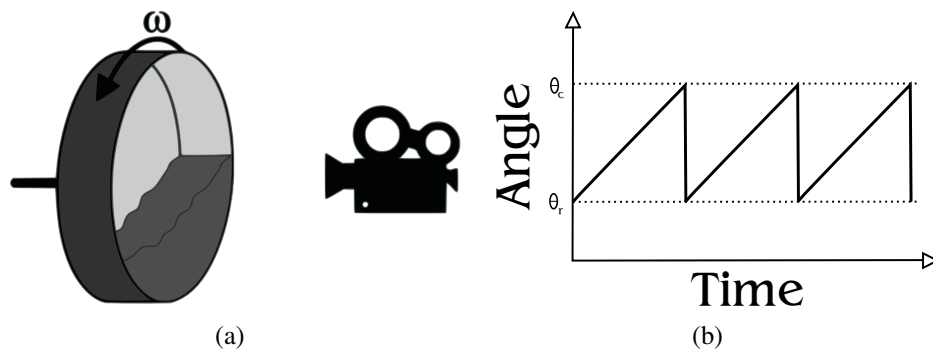


Figure 3.1: On the tumbler experiment to determine the angle of repose. (a) Setup, (b) idealized time series of the measured slope angles.

The angle at which the material starts flowing will not be the same for every onset of flow but will vary due to irregularities in the packing of the particles¹. A sufficiently large number of flows must be observed and the desired angles can then be estimated by a statistical analysis.

The rotating drum can also be used to measure another useful quantity called the dynamic angle of repose ϑ_{dyn} . When the angular velocity exceeds a certain threshold² there will be a continuous downflow of material. This range of rotational velocity is therefore called *continuous regime* in contrast to the *discrete avalanching regime* that was the focus of the previous considerations. In the continuous regime the flowing material forms an angle with the horizontal that is the dynamic angle of repose.

3.1.2 Dilatancy

The dilation of granular material under external stress has first been investigated by Reynolds (1885). The author illustrates the effect of dilatancy with the example of wet sand on the beach that suddenly appears dry when stepped upon.

Before the foot is set down the water level is at the same height as the sand due to capillary forces. When the foot is set down it applies pressure to the sand which then dilates. The sand level rises above the water level, leaving it dry as the water needs time to be transported upwards by the capillary forces. When the foot is raised the sand immediately gets wet again as the sand contracts upon removal of the external force.

3.1.3 Friction

Friction between the surfaces of two solid bodies hinders the relative motion of these bodies. It arises from adhesive forces between two bodies. This can be on macroscopic

¹This can be considered as a hysteresis effect. The way the material behaves in a given situation is partly determined by the way it got there.

²This threshold is determined by e.g. material properties like grain size and shape (Dury *et al.* 1998), the presence and viscosity of the interstitial fluid (Carrigy 1970) and the gravitational acceleration (Brucks *et al.* 2007).

level by interlocking of rough surfaces or on the atomic level by induced dipole-dipole interaction (*van-der-Waals force*) or through the formation of molecular bonds.

Friction is obvious when a block tries to slide on a surface but is also present with small grains that are in contact. If the two touching bodies are at rest, the force necessary to move one over the other³ is proportional to the normal force that holds them together but independent of the apparent contact area.

$$F_{\text{static}} = \mu_s \cdot F_{\text{normal}} \quad (3.1)$$

where μ_s is the empiric coefficient of static friction. For a granular material μ_s is related to the static angle of repose by

$$\tan \vartheta_c \approx \mu_s. \quad (3.2)$$

This was first formulated by Coulomb (1773), who equated the coefficient of static friction in a sand pile to the ratio of shear to normal stress.

Once the frictional force is overcome the bodies will slide relative to each other (the slope of the sandpile will flow) and the force necessary to maintain this sliding motion is

$$F_{\text{dynamic}} = \mu_k \cdot F_{\text{normal}} \quad (3.3)$$

where μ_k is the empiric coefficient of kinetic friction with $\mu_k \leq \mu_s$.

3.2 Granular material in space

3.2.1 Lack of interstitial fluid

Interstitial fluids such as air (or any type of gas) or liquids can drastically change the way granular matter behaves. Bagnold (1954, 1966) discriminates the dynamic behavior of a granular system by the ratio of the forces created by collisions between the particles and the forces created by viscous effects of the interstitial fluid.

This ratio (which was later termed the *Bagnold number* N (Hunt *et al.* 2002)) determines whether a granular flow is dominated by inertia of the grains ($N > 450$) or by the viscosity of the interstitial fluid ($N < 40$) with a transition region between the two values (Mehta and Barker 1994).

The behavior of granular matter in airless space is thus governed by the grain inertia.

3.2.2 Possible deprivation of small particles

Several findings of theoretical and observational nature indicate that regolith on small bodies may be deprived of the finest particle fraction.

The particle size distribution found in meteorite regolith breccia display a deficiency in fine grains (radius between 10 and 70 μm) compared to lunar samples (Bhattacharya *et al.* 1975).

³This force is called *static friction* or *Coulomb friction* in honor of the ground breaking work of Coulomb (1773).

Hörz and Schaal (1981) argue that spallation products could play a major role in regolith creation on small bodies. These spalls are usually more coarse and ejected at lower velocities than impact ejecta and thus more easily retained. Additionally, the volume of spallation products surpasses that of impact ejecta making the regolith creation from spall more effective.

Electrostatic levitation might be a possible mechanism that removes fine grains from the surfaces of asteroids. If a sufficiently large electric field is generated (e.g. through impingement of charged solar wind particles), the smallest grains (micron size) could directly be accelerated to velocities in excess of the escape velocity. Grains of sizes up to $100\ \mu\text{m}$ could be transported to and trapped in areas of the body that are permanently shadowed (Lee 1996).

The resulting deprivation in fine grains is confirmed by a theoretical model that relates the thermal inertia of regolith-covered bodies with the mean grain size of the regolith (Gundlach and Blum 2013). The authors infer that smaller bodies have coarser regolith because the ejection speed of fine ejecta particles is, on average, higher than for more massive grains and they are thus preferentially lost on bodies with low gravitational acceleration, i.e. bodies with low escape velocity.

3.3 Possible trigger mechanisms for avalanches on small bodies

There are many ways in which an avalanche may be triggered. A qualitative description of the most important trigger mechanisms will be given here to gain an understanding of their overall influence. The focus of this chapter will lie on trigger mechanisms on atmosphereless small bodies.

Precipitation of ejected material. During any kind of impact material is ejected off the target body. If the ejecta particles travel faster than the escape velocity v_e of the target body they will leave never to return. If their velocity is smaller than v_e they will eventually fall back onto surface. This precipitation of ejected particles can increase a preexisting slope to a point where the slope angle exceeds the local static angle of repose. Then a landslide will occur.

Vibrations. The high energy impact of a body onto a surface can lead to the creation of seismic waves traveling through the target body. Like earthquakes on Earth these vibrations can destabilize a slope to a point where the material starts flowing.

Large scale impacts. Impacts of bodies that are either massive enough or fast enough to directly reshape the surroundings of their impact site shall be considered as *large scale* or *major* impacts. These impacts create a shock wave that will agitate the material in the immediate surroundings and can thus trigger an avalanche if the impact is close enough to a slope where the tilt angle is between the static and dynamic angle of repose.

Small scale impacts. Impacts of bodies that are much smaller than their target and much slower than the average collision velocity at the target shall be called *small scale* or *minor* impacts. This kind of impact can excite the movement of a few initial particles that can then collide with further ones in a cascade initiating an exponential increase in moving particles. The effects of this kind of impacts and the necessary prerequisites will be investigated in chapters 5 and 6.

Close encounter with another body. If the body in question is passed by a sufficiently large body in close proximity, the local gravity field on both bodies will change due to the attractive force of the masses passing as well as possible changes in the rotational and orbital state of either body. This can change both the magnitude as well as the direction of the gravity vector. A slope that had a given tilt with respect to the gravity vector before the encounter can have a different tilt angle during the encounter because the direction of the total force vector changes. If the temporary tilt angle exceeds the static angle of repose the slope will collapse.

Spin-up. Among the non-gravitational effects acting upon a small body is the so called *YORP*-effect, named after Iwan O. Yarkovsky, John A. O’Keefe, Vladimir V. Radzievskii and Stephen J. Paddack, the researchers that postulated it. The *YORP*-effect is the change of the rotational state of a body that is caused by anisotropic emission of thermal radiation. This anisotropic emission creates a torque that can lead to an acceleration or a deceleration of the bodies rotation. Any change of the rotational state of a body will change its gravitational acceleration and will alter the slope angles on its surface through the change of the direction of the total acceleration vector (sum of gravitational and non-gravitational forces such as centrifugal force) (Rubincam 2000, Lowry *et al.* 2007). The asteroid (2867) Šteins is believed to have been reshaped by spin-up due to *YORP*-induced avalanching (Keller *et al.* 2010).

Tidal forces. Consider an asteroid that is part of a binary system (either with another asteroid or with a larger body). Then this asteroid will experience tidal forces. If it is not within the Roche limit of the other body (Chandrasekhar 1969) the asteroid will not be disrupted but only experience deformation. Modeling of the Mars moon Phobos by Shi *et al.* (2013) suggests that these tidal deformations could have increased crater slopes to values exceeding the angle of repose, causing the down-slope movement observed by the Mars Orbiter Camera (Thomas *et al.* 2000).

4 ROSETTA

ROSETTA, a planetary corner stone mission in ESA's Horizon 2000 long-term program (Bonnet 1985), is targeting to rendezvous with comet 67P/Churyumov-Gerasimenko in 2014 to investigate the origin of comets and by that the origin of the solar system (Schwehm and Schulz 1999).

4.1 The Mission

The information about the international ROSETTA mission described in the following section is mostly taken from Glassmeier *et al.* (2007), other sources are indicated correspondingly.

The main goal of the ROSETTA spacecraft is to study the comet 67P/Churyumov-Gerasimenko through remote sensing (from the orbiter) and in-situ measurements (by instruments on the orbiter and the PHILAE lander).

ROSETTA was originally planned to be launched in January 2003 to be sent to comet 46P/Wirtanen. But after the failure of an Ariane rocket shortly before the launch, the mission was postponed. A new target was searched and found in 67P/Churyumov-Gerasimenko and ROSETTA was finally launched on March 2, 2004 from the Guyana Space Center in Kourou.

To be able to push forward into deep space beyond 5 au and reach the comet, ROSETTA had to gain velocity through four swing-by maneuvers (three at Earth, one at Mars). The spacecraft journeyed twice through the main asteroid belt to finally meet with 67P/Churyumov-Gerasimenko at a heliocentric distance of about 3.5 au in August 2014 (Schulz 2012).

ROSETTA will orbit the comet nucleus throughout its perihelion passage in August 2015 (distance to the Sun 1.25 au) and continue investigation until the end of the nominal mission on December 31, 2015.

The trajectory of ROSETTA as well as the orbits of Earth, Mars, (2867) Šteins, (21) Lutetia and 67P/Churyumov-Gerasimenko are traced in figure 4.1¹.

During its cruise through interplanetary space towards the comet ROSETTA passed through the main asteroid belt twice. Its first passage led the spacecraft by the asteroid (2867) Šteins, a 5 km large fragment of a once larger body (Schulz 2012), on September 5, 2008 with a closest approach distance of 803 km and a relative velocity of 8.6 km/s (Keller *et al.* 2010). The image taken at closest approach is shown in figure 4.2.

¹The plot was created with data obtained from NASA JPL Solar System Dynamics *Horizons Web Interface* <http://ssd.jpl.nasa.gov/?horizons>.

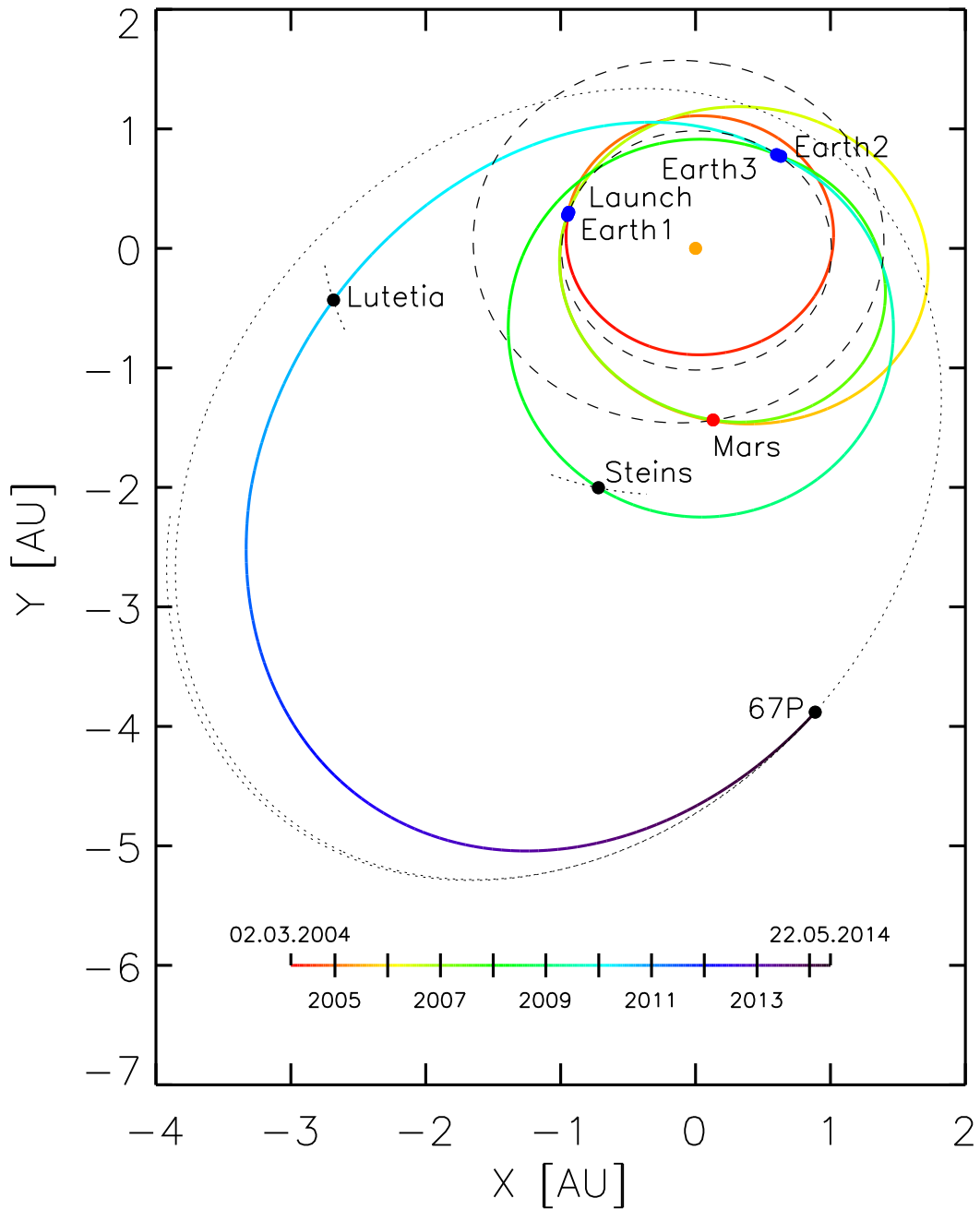


Figure 4.1: Trajectory of ROSETTA (rainbow colored solid line; color indicates the passage of time from launch to rendezvous with the comet) with the orbits of Earth (inner dashed line), Mars (outer dashed line), 67P/Churyumov-Gerasimenko (dotted) and parts of the orbits (around ROSETTA closest approach) of (21) Lutetia and (2867) Šteins (short dotted lines). Important events are indicated: Launch (March 2, 2004), Earth fly-bys (March 4, 2005; November 13, 2007; November 13, 2009), Mars fly-by (February 25, 2007), (2867) Šteins fly-by (September 5, 2008), (21) Lutetia fly-by (July 10, 2010), rendezvous maneuver at 67P/Churyumov-Gerasimenko (May 22, 2014) (similar to Fig. 2 in Glassmeier *et al.* 2007).



Figure 4.2: (2867) Šteins as imaged by OSIRIS during closest approach (September 5, 2008).

The second pass through the main belt led ROSETTA by the asteroid (21) Lutetia, one of the largest asteroids in the asteroid belt. For details of this fly-by see chapter 4.3 below.

4.2 OSIRIS

Among the scientific instruments flown on ROSETTA, OSIRIS will be described in detail in this section as the images it took of (21) Lutetia show the regolith covered surface of the asteroid and the landslides that were the impetus for the research described in this thesis.

The details about OSIRIS presented here are taken from Keller *et al.* (2007).

The *Optical, Spectroscopic, and Infrared Remote Imaging System* (OSIRIS) is the camera system on-board ROSETTA, named for the ancient Egyptian god Osiris who is identified by the all-seeing eye.

OSIRIS was built by an international collaboration of scientific institutions from six different European countries, all designing, building, integrating or supporting different parts of the camera system.

OSIRIS comprises two cameras:

The narrow angle camera (NAC). The NAC has a high angular resolution of $18.6 \mu\text{rad}/\text{px}$ resulting in a spatial resolution of $1.86 \text{ cm}/\text{px}$ at 1 km distance but a small field of view of $2.20^\circ \times 2.22^\circ$. The detector is a 2048×2048 Pixel CCD. The NAC covers a wavelength range of $250 - 1000 \text{ nm}$ and has a total of 12 filters with a band pass of typically 40 nm that can be placed in front of the optical system by means of a filter wheel. The main task of the NAC during prime mission is high resolution imaging of the comet's nucleus to investigate the structure and mineralogy of the surface and the dust ejection process.

The wide angle camera (WAC). The WAC has a lower angular resolution than the NAC; $101 \mu\text{rad}/\text{px}$ resulting in a spatial resolution of $10.1 \text{ cm}/\text{px}$ at 1 km distance. Its field of view, though, is larger than the NAC's: $11.35^\circ \times 12.11^\circ$. The detector is a 2048×2048 Pixel CCD. The WAC covers a wavelength range of $240 - 720 \text{ nm}$ and has a total of 14 filters with a band pass of typically 5 nm that can be placed in front of the optical system by means of a filter wheel. The main task of the WAC during prime mission is imaging of the three-dimensional flow field of dust and gas in the coma of the comet.

During the asteroid fly-by OSIRIS's scientific goals were the determination of their physical parameters (including shape and rotation state) and investigation of their surface morphology and mineralogy.

4.3 (21) Lutetia

(21) Lutetia was ROSETTA's second target in the main asteroid belt. The fly-by took place on July 10, 2010, with a closest approach distance of 3168 km and a relative speed of $15 \text{ km}/\text{s}$ (Schulz *et al.* 2012).

During this fly-by, both remote and in-situ measurements, were carried out starting from 9 hours 30 minutes before closest approach (CA) to 16 minutes after CA (Sierks *et al.* 2011, Schulz 2012).

4.3.1 (21) Lutetia - Pre fly-by

(21) Lutetia was discovered on November 15, 1852 by German-French amateur astronomer M. Hermann Goldschmidt from the balcony of his apartment in Paris (Lardner 1867) and later confirmed by observations made at the Paris Observatory; at the time classified as a "small planet". It was named Lutetia by Goldschmidt's colleague François Arago in honor of the place of its discovery, Paris or *Lutetia Parisorum* in Latin (Goldschmidt 1852).

Ground based observations (Barucci and Fulchignoni 2007, and references therein) determined the physical characteristics of (21) Lutetia as given in table 4.1. These measurements were found to be in good agreement with the results of the data analysis of the spacecraft measurements (Schulz *et al.* 2012)

Table 4.1: Orbital and physical parameters of (21) Lutetia from ground based observations.

Semimajor axis [au]	2.435
Eccentricity	0.164
Inclination [$^\circ$]	3.064
Synodical rotation period [h]	8.17
IRAS Diameter [km]	95.5



Figure 4.3: (21) Lutetia imaged by OSIRIS at 15:43:19.5 UT on July 10, 2010.

4.3.2 (21) Lutetia - Post fly-by

ROSETTA flew by (21) Lutetia on July 10, 2010 at a heliocentric distance of 2.43 au and geocentric distance of 3.05 au (Schulz *et al.* 2012). The point of closest approach (CA) was reached at 15:45:53.3 UT with a spacecraft-to-target distance of 3168 km (Preusker *et al.* 2012) and a relative velocity of 15 km/s (Sierks *et al.* 2011). Figure 4.3 shows (21) Lutetia at 15:43:19.5 UT.

Figure 4.4² plots the distance between the spacecraft and the asteroid as well as the phase angle (the angle between the sun and the spacecraft as seen from the asteroid) as a function of time from 40 minutes before to 30 minutes after closest approach.

²The plot was created with data obtained from NASA JPL Solar System Dynamics *Horizons Web Interface* <http://ssd.jpl.nasa.gov/?horizons>.

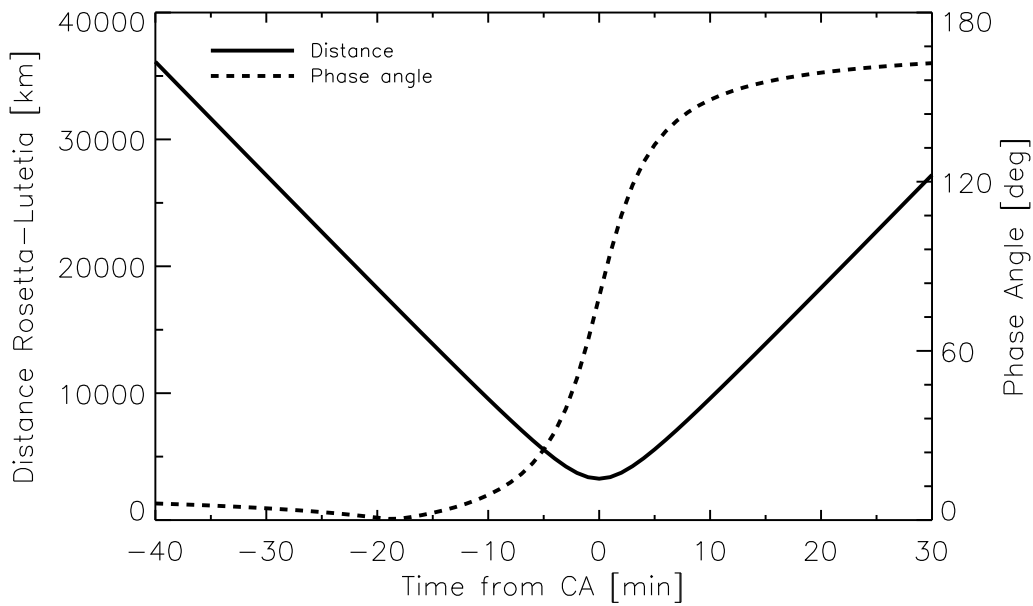


Figure 4.4: ROSETTA- (21) Lutetia-distance and phase angle (Sun-Lutetia-Rosetta) as a function of time around closest approach (similar to Fig. 2 in Schulz *et al.* 2012).

Scientific instruments on ROSETTA and the PHILAE lander were in operation between July 5 and July 14, 2010. (Schulz *et al.* 2012). Among these, OSIRIS took 400 images of varying spatial resolution (60 m/px at CA).

(21) Lutetia’s northern hemisphere was mainly illuminated and thus visible during the fly-by. Results of the fly-by consequently focus on that region of (21) Lutetia.

The most important findings shall be reported in greater detail in the following sections.

4.3.2.1 Physical and orbital properties

OSIRIS images and the Radio Science Experiment (RSI) on board ROSETTA were used to determine basic physical properties of (21) Lutetia. These are summarized in table 4.2. (21) Lutetia can be approximated by a triaxial ellipsoid with the given dimensions measured along the principal axes of rotation (Sierks *et al.* 2011, Pätzold *et al.* 2011).

Table 4.2: Physical parameters of (21) Lutetia from OSIRIS and RSI measurements

Dimensions	$(121 \pm 1) \times (101 \pm 1) \times (75 \pm 13) \text{ km}^3$
Volume	$(5.0 \pm 0.4) \cdot 10^{14} \text{ m}^3$
Mass	$(1.7 \pm 0.017) \cdot 10^{18} \text{ kg}$
Bulk density	$(3.4 \pm 0.3) \cdot 10^3 \text{ kg/m}^3$
Obliquity	96°

The measured bulk density is among the highest bulk densities of all the known asteroids. Comparing this to the density of primitive C-type asteroids ($1700 - 2700 \text{ kg/m}^3$), (21) Lutetia needs a rather low macro porosity of $\varphi_{\text{Lut}} = 0 - 13 \%$ to be still compatible with the C-type density. This low porosity indicates that (21) Lutetia was heated in the past, possibly to a point where it melted and differentiated and is also consistent with (21) Lutetia being fractured rock. This is suggestive of (21) Lutetia being primordial, i.e. the asteroid is an intact planetesimal rather than an evolved rubble pile (Sierks *et al.* 2011, Weiss *et al.* 2012).

Hydrocode simulations of the impact that formed the large 57 km *Massilia* crater suggest that this event fractured (21) Lutetia's interior, enforcing the conclusion that (21) Lutetia is indeed primordial. This is furthered by the lack of a collisional family around (21) Lutetia that would have existed, if (21) Lutetia was the fragment of a larger body (Cremonese *et al.* 2012).

This conclusion is supported by theoretical modeling which suggests that bodies of the size of (21) Lutetia have a collisional lifetime larger than the age of the solar system (Bottke *et al.* 2005, Morbidelli *et al.* 2009).

The high obliquity (96° mean) that the axis of rotation almost lies in the orbital plane) means that the pole in the summer hemisphere stays illuminated for half an orbit rotation while the pole in the winter hemisphere remains in complete darkness for the same time. This causes large differences in temperature on both hemispheres. The dual-band radiometer/spectrometer instrument, named MIRO, measured the temperature on the summer and winter hemisphere to be between $197 - 208 \text{ K}$ and $62 - 72 \text{ K}$, respectively (Gulkis *et al.* 2012).

4.3.2.2 Geography

Boundaries for several geographic regions on (21) Lutetia have been deduced on the basis of local topography, surface texture, crater density, geological features and stratigraphic relationships (Thomas *et al.* 2012) which are superimposed on the NAC image taken at 15:42:41.240 in figure 4.5.

4.3.2.3 Cratering History

The crater size frequency distribution (SFD) of the different regions of (21) Lutetia can be used to constrain the age of the surface. Using the framework of the model production function chronology (Marchi *et al.* 2009)³, Marchi *et al.* (2012) derive ages (given in table 4.3) for the four geological units where the resolution of the images was sufficiently high to allow crater counting to be performed.

A flexure in the SFD (depletion in small craters, $D < 1 \text{ km}$) of all four regions can only be reproduced by the models if a stratified target is assumed. This stratification occurs most likely in the form of a fractured surface layer of $\sim 3 \text{ km}$ depth covering more competent rock (Marchi *et al.* 2012, Sierks *et al.* 2011). The existence of such a fractured

³In this framework the number of craters produced per unit area and unit time is modeled with the help of (21) Lutetia's theoretically derived impactor size and velocity distribution. A model size frequency distribution is then calculated and compared to the observed one to find the correct age that reproduces the observation.

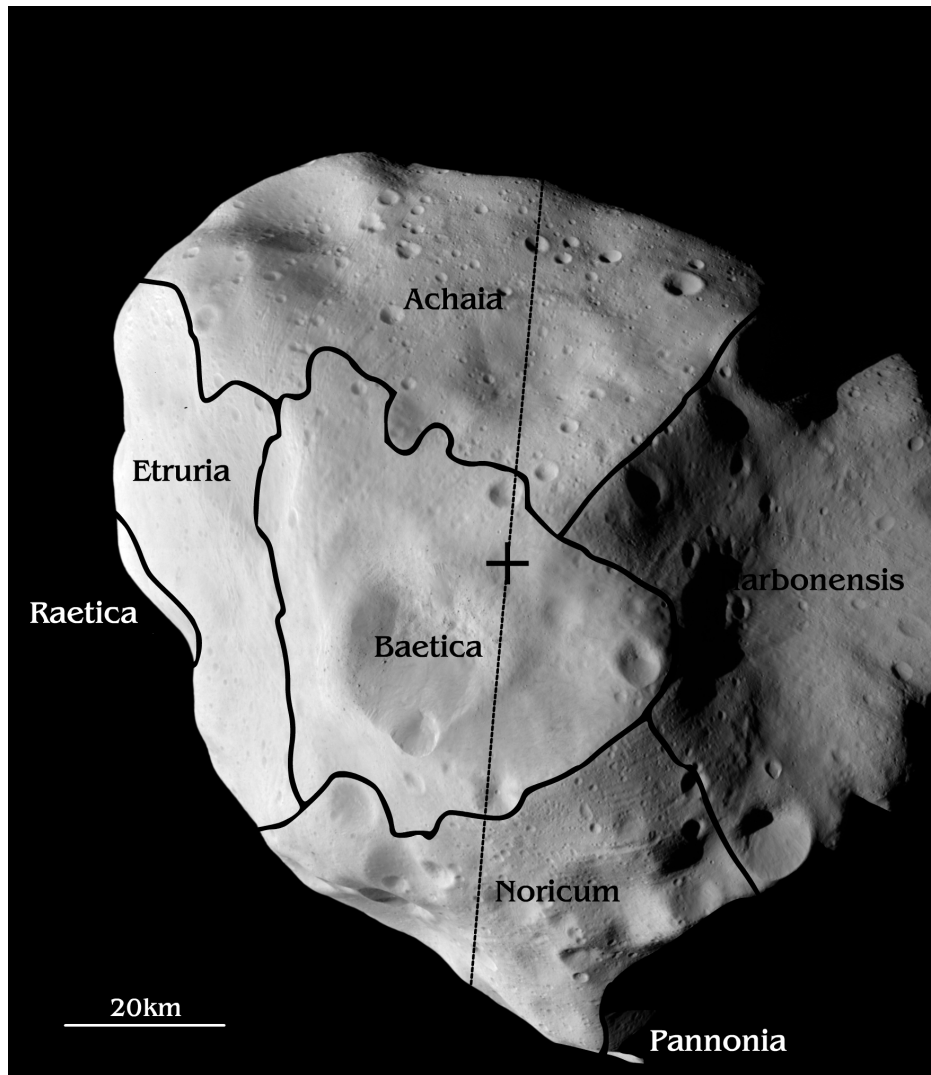


Figure 4.5: (21) Lutetia geological map as defined in Sierks *et al.* (2011), Massironi *et al.* (2012), Thomas *et al.* (2012). The five main units are visible together with small parts of the other two in this OSIRIS image (NAC 15:42:41.240): *Achaia*, *Baetica*, *Etruria*, *Narbonensis*, *Noricum* and *Pannonia*, *Raetica*. The cross “+” indicates the position of the north pole. The dashed line represents the prime meridian.

Table 4.3: Ages of geological units from crater size frequency distribution (Marchi *et al.* 2012).

<i>Achaia</i>	3.6 - 3.7 Ga
<i>Baetica</i>	50 - 220 Ma
<i>Narbonensis</i>	0.95 - 1.3 Ga
<i>Noricum</i>	3.4 - 3.7 Ga

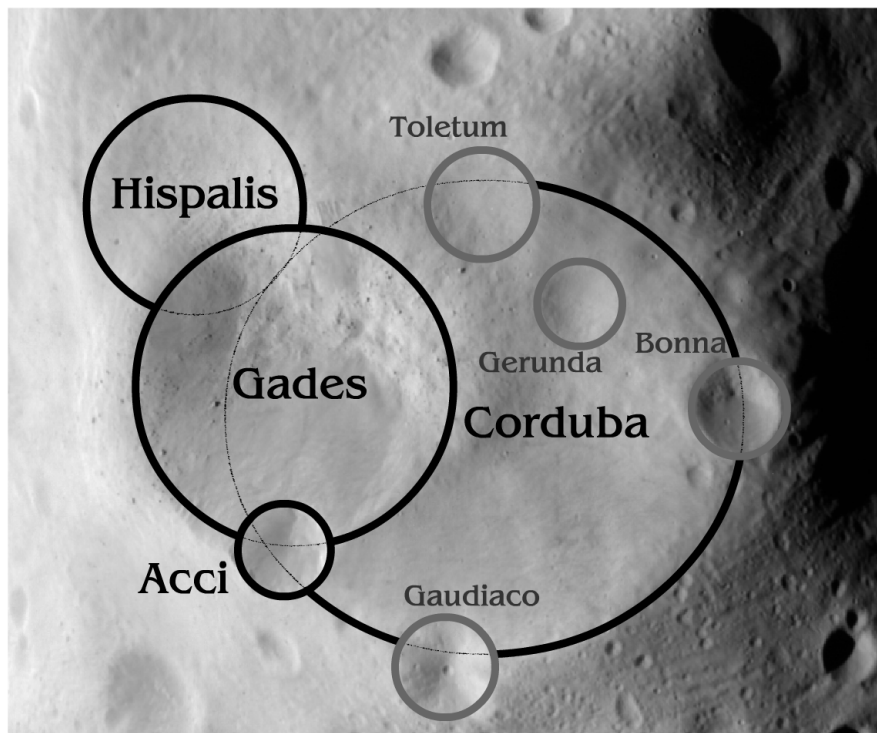


Figure 4.6: The North Polar Crater Cluster (NPCC). Zoom of OSIRIS image (NAC 15:42:41.240). Shown are the four main craters of the NPCC: *Corduba* ($D = 33$ km), *Gades* ($D = 21$ km), *Hispalis* ($D = 14$ km), and *Acci* ($D = 6$ km). Also indicated are *Bonna*, *Gaudiaco*, *Gerunda*, and *Toletum*. (Crater locations and names adapted from Thomas *et al.* 2012).

layer of rock is also supported by the presence of grooves and lineaments over the entire surface (Thomas *et al.* 2012).

The *Narbonensis* region contains the 57 km crater *Massilia*, that was created by an impactor of 7.5 km diameter that impacted with a velocity of the order 4.3 km/s. This impact most likely created the fractured layer as impact simulations of this event that incorporated an already fractured (21) Lutetia failed to reproduce the observed depth-to-diameter-ratio (d/D) of the *Massilia* crater (Cremonese *et al.* 2012). The impact most likely occurred early in (21) Lutetia's history. The probability of an impact of this size happening within the age of the solar system is 25 %⁴ (Marchi *et al.* 2012) and it is therefore likely that it happened early when the impact rate in the asteroid belt was more intense by a factor of 2 – 4 (Morbidelli *et al.* 2010). The young age of *Narbonensis* is in disagreement with this hypothesis. The early impact could thus only be valid if a later event (or events) resurfaced the *Narbonensis* region (Thomas *et al.* 2012).

An accumulation of craters, called the North Polar Crater Cluster (NPCC), can be found in *Baetica* region close to the north pole. It consists of four large craters of 6, 14, 21 and 33 km diameter, respectively, and several smaller craters, partly overlapping one another. Names and locations of the respective craters are given in figure 4.6.

⁴This means that an impact of this size happens once every 9 Ga.

200 Boulders of sizes from 300 m down to the resolution limit of 60 m were found close to the NPCC and one other crater on (21) Lutetia. The boulders were most likely created by an impact (or impacts) that penetrated through the regolith layer (see below) and fractured the underlying bedrock, i.e. the boulders are ejecta blocks (Massironi *et al.* 2012, Küppers *et al.* 2012). The irregular spatial distribution of the boulder is most likely due to the limited lifetime of the blocks, which is estimated by Küppers *et al.* (2012) to be between 80 and 160 Ma. This can be used to infer the age of the boulder forming crater in the NPCC (*Gades*) to be of the order 300 Ma.

4.3.2.4 Regolith and granular flow on (21) Lutetia

The presence of regolith on the surface of (21) Lutetia can be derived from the ROSETTA data in several different ways.

Thermal inertia. The MIRO instrument on ROSETTA measured not only the temperature of the body. The data recorded was used to derive the thermal inertia of the body to be less than $20 \text{ J/K/m}^2/\text{s}^{1/2}$ in the upper 1 – 3 cm. Such a low value points to a lunar like regolith that covers almost the entire surface (Gulkis *et al.* 2012).

Slope angles. The slope angles relative to the local gravity vector across (21) Lutetia were derived from the shape model and the assumption of a homogeneous interior structure. Only 5 % of the slopes exceed the angle of repose for sand (33°), and only 0.1 – 1 % exceed that of Talus (i.e. poorly sorted angular fragments, $\sim 40^\circ$). Such low slope angles can be most easily explained by a surface that is deeply covered with regolith (Vincent *et al.* 2012, Weiss *et al.* 2012).

Avalanches and flow-like features. Direct observations of collapsed crater walls and rims as well as asymmetric craters that display flow features towards the local gravitational minimum suggest that (21) Lutetia is covered with a dry granular medium (Vincent *et al.* 2012).

Vincent *et al.* (2012) estimate the depth of this regolith layer to be up to 600 m close to NPCC, using the depth-to-diameter-ratios of craters.

5 Experiments on Avalanche Triggering

One of the main drivers of this theses was to gain an understanding of the importance of one of the avalanche trigger mechanisms mentioned in section 3.3: the impact of small objects at low velocity. This chapter will describe the suite of experimental campaigns that has been devised in order to answer whether this scenario is a viable trigger for avalanches on an asteroid.

5.1 Introduction

To gain an insight into the dynamical behavior of granular material on asteroids, an experiment was designed to investigate small scale low velocity impacts as a possible trigger for avalanches or landslides.

(21) Lutetia is among the largest asteroids in the main belt, yet not big enough to maintain an atmosphere. The mean gravitational acceleration at the surface is $g_L = 0.047 \text{ m/s}^2 \approx 5 \cdot 10^{-3} g_0$. The acceleration is modified by centrifugal forces.^{12 3}

The negligible gas pressure and the low gravity level make it challenging to perform experiments investigating events taking place on the asteroid's surface. The experiment described in this chapter was therefore performed in vacuum during the fall of a capsule in a drop tower (for further details, see section 5.3.1).

The impact velocity for primary impacts on asteroids in the present-day main belt is about 5 km/s (Davis *et al.* 2002), way faster than what can be achieved in the framework of a drop tower campaign.

The velocity regime investigated here is relevant for secondary (or tertiary) impacts, i.e. material excavated by a primary impact falling back onto the surface of the target with speeds well below those of the primary impactor.

The investigation of an avalanche on a big scale is not possible experimentally if one wants to consider airless bodies with low gravitational acceleration. Therefore the experiment was designed to probe the early stages of avalanches very close to the impact point shortly after impact.

¹ $g_0 \approx 9.81 \text{ m/s}^2$ is the mean gravitational acceleration on the surface of the Earth.

²This value is calculated as the surface gravity of (21) Lutetia's equivalent sphere which has a radius of $r = 49 \text{ km}$ and a mass of $m_L = 1.7 \cdot 10^{18} \text{ kg}$ (Sierks *et al.* 2011). The equivalent sphere of an irregular body is the sphere of diameter $2 \cdot r$ that has the same volume as that body.

³The centrifugal acceleration on the equator of (21) Lutetia's equivalent sphere that is rotating with a rotational period of 8 h and 10 min amounts to 0.002 m/s^2 , less than 5% of the gravitational acceleration.

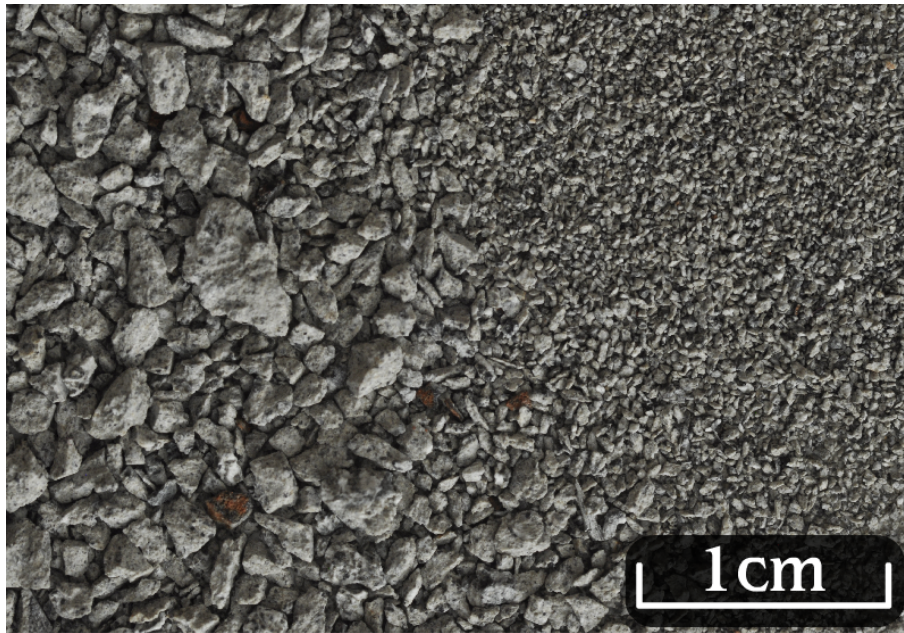


Figure 5.1: Image of the ground HED showing the irregular shape of the grains.

To further the understanding of the process underlying the onset of an avalanche, simulations of the experiment were conducted using the ESyS-Particle software package, which utilizes the discrete element method to simulate granular materials (see chapter 6).

5.2 Material Analysis

Different materials have been used during this experimental investigation to get more diverse results in the context of changing material properties, grain sizes and grain shapes. Both materials and their properties will be described in the following sections.

5.2.1 HED

The Howardites, Eucrites and Diogenites (HEDs) are members of a class of basaltic, achondritic meteorites. They are spectrally similar to (4) Vesta, a 516 km diameter main belt object, and are believed to originate from this body and its collisional family (e.g. McSween and Stolper 1980, Binzel and Xu 1993, Kelley *et al.* 2003, Russell *et al.* 2012). (4) Vesta has a mantle density of about 3000 kg/m^3 which coincides with the density of the HED meteorites (Konopliv *et al.* 2013). Mineralogical mapping of (4) Vesta by DAWN also shows a surface composition that is consistent with that of the HED meteorites (De Sanctis *et al.* 2012).

Meteoritic material is used as a direct proxy for the behavior of asteroidal material. The material brought to Earth via meteorites samples the surface of an asteroid and leaves grain size and shape as an unknown parameters for interpretation of the experiment's results.

A part of an HED meteorite was ground down to grain sizes between $100\ \mu\text{m}$ and $\sim 4\ \text{mm}$. The grains have a highly irregular shape as can be seen in figure 5.1. Regolith of small atmosphereless bodies can be expected to be more edgy in shape than their planetary counterparts as there is no atmosphere or liquid that could abrade the grains to a more spherical shape. The behavior of grains with a more spherical shape is investigated with the MARS-1 sand described in the following section.

The HED mass fraction (a proxy for the grain size distribution) is plotted in figure 5.2.

5.2.2 JSC MARS-1 Martian Soil Simulant

The *Johnson Space Center* MARS-1 Martian Soil Simulant is a palagonitic tephra (glassy volcanic ash altered at low temperatures) sampled at the Pu'u Nene cinder cone on Hawaii, sieved to grain sizes below 1 mm. It is in spectral appearance similar to Martian bright regions. The material has a bulk density of $1600 \pm 400\ \text{kg/m}^3$ (Morris *et al.* 1993). The MARS-1 mass fraction (a proxy for the grain size distribution) is plotted in figure 5.2.

The MARS-1 is used as test case for larger planetary bodies with grains of a more spherical nature. It is not only used in its unsieved form but also in coarser sievings as listed in table 5.1.

Table 5.1: Diameter ranges used in the experiments with MARS-1.

Unsieved		$d < 1000\ \mu\text{m}$
Rather fine	$250\ \mu\text{m}$	$< d < 1000\ \mu\text{m}$
Rather coarse	$800\ \mu\text{m}$	$< d < 1000\ \mu\text{m}$

Different levels of coarseness can be expected due to different mechanisms of sorting that can act in both, vacuum (small bodies) and atmosphere (planet sized bodies). These effects include size segregation in granular flow (e.g. Ottino and Khakhar 2000, Félix and Thomas 2004), seismic shaking leading to the “Brazilian nut effect” (e.g. Kudrolli 2004) or sorting due to the influence of atmospheric winds (Jerolmack *et al.* 2006).

5.2.3 Determining the angle of repose

To determine the angle of repose of the HED and the MARS-1, the tumbler setup described in chapter 3.1.1 was used. The tumbler used for the measurements presented here had a diameter of 82 mm and a depth of 20 mm. The outer walls had been covered with rough sandpaper (grit size P60) to prevent the material from slipping down the wall. It was rotated moderately fast at 150 deg/min. An exemplary time series of the measured angle as a function of frame is plotted in figure 5.3, yielding a distribution for the angle of repose and angle of rest given in figure 5.4.

The measurements yielded the results given in table 5.2.

The angle of repose for the HED has to be interpreted with caution. The highly irregular shape of the HED grains causes strong variations in the highest tilt angle possible due to mechanical interlocking between the grains.

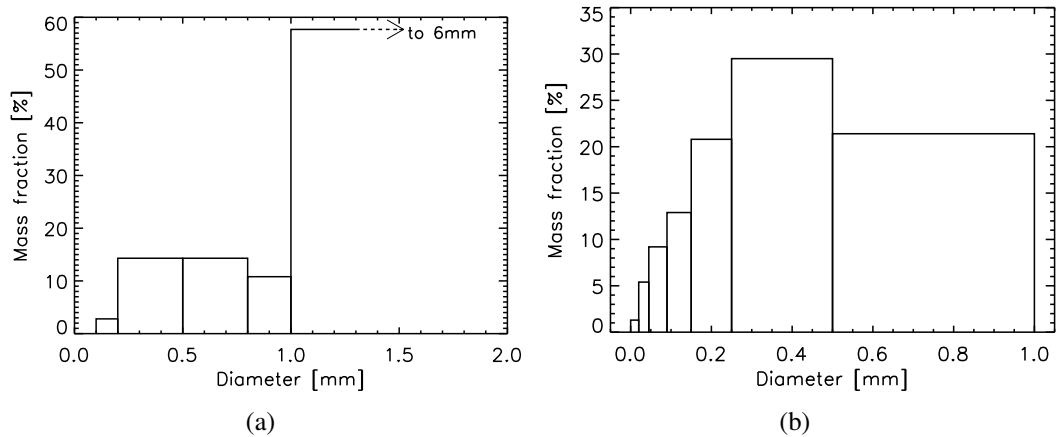


Figure 5.2: Mass fraction of the ground HED and the JSC MARS-1 Martian Soil Simulant. The plotted MARS-1 values were taken from Morris *et al.* (1993).

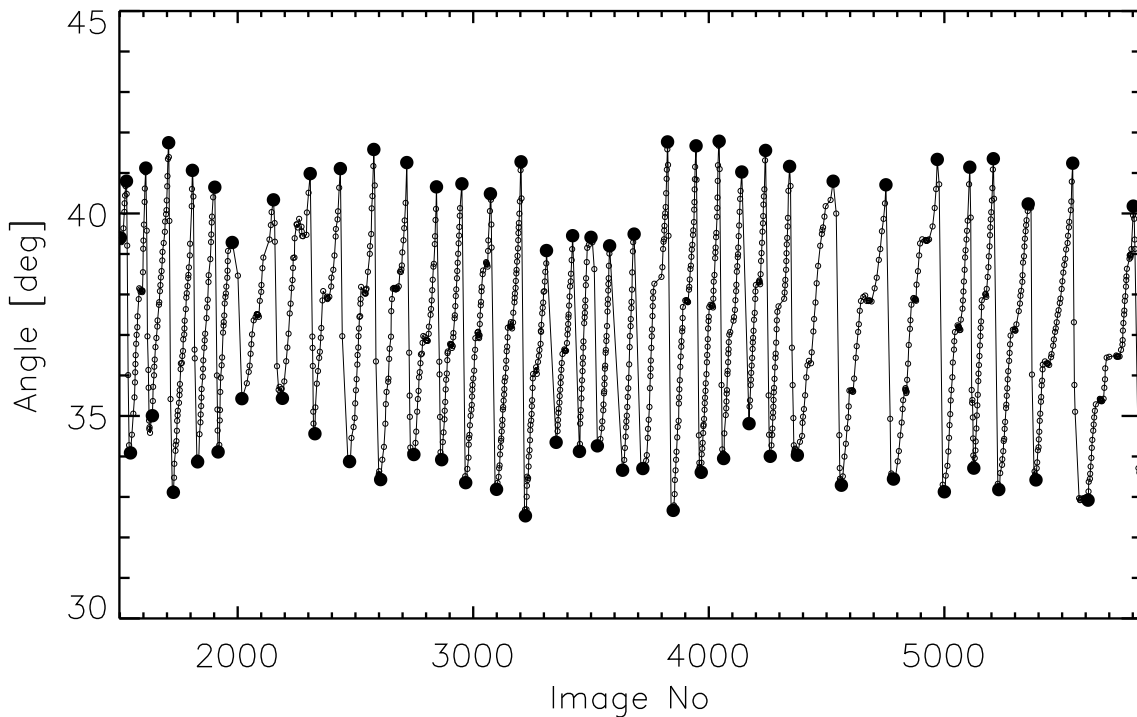


Figure 5.3: An exemplary time series of the tilt angle of MARS-1 sand with $d > 250 \mu\text{m}$ in a tumbler rotated with 150 deg/min . An open circle indicate an angle measurement. The filled big circles denote the static angle of repose (upper filled circles) or the angle of rest after a slope failure (lower filled circles).

5.3 Experimental Campaign

The experiments described in this chapter had to be carefully designed, conducted and analyzed in order to answer questions about the significance of minor impacts on asteroidal

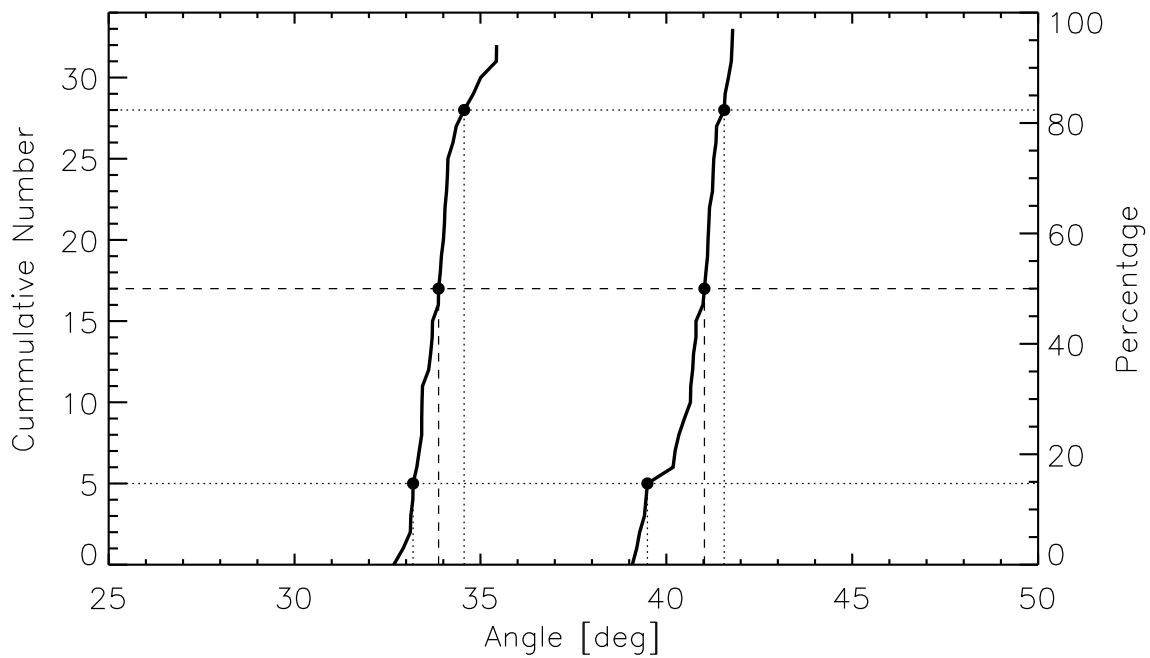


Figure 5.4: An exemplary distribution of angles of rest (left curve) and angles of repose (right curve) retrieved from the measurement plotted in figure 5.3. The dashed line indicates the median value of the distribution. The dotted lines denote the 1σ error environment.

Table 5.2: Measured static angle of repose and angle of rest.

Material	Sieving	Static angle of repose	Angle of rest
HED		$42.95^{+2.21}_{-3.38}$	$36.11^{+2.01}_{-1.71}$
MARS-1	0 – 1000 μm	$40.95^{+0.96}_{-1.14}$	$36.0^{+1.86}_{-1.27}$
MARS-1	250 – 1000 μm	$41.02^{+0.53}_{-1.53}$	$33.87^{+0.69}_{-0.69}$
MARS-1	800 – 1000 μm	$44.17^{+1.55}_{-0.97}$	$35.45^{+1.47}_{-0.76}$

surfaces. The following sections will describe the key aspects of the experimental setup, the data analysis and the interpretation of the data.

5.3.1 Accomplishing low gravity

There are different ways to create an environment of reduced gravity for an experiment.

1. Parabolic flight in an aircraft
2. Parabolic flight in a rocket
3. Space flight
4. Drop in a Vacuum Drop Tower

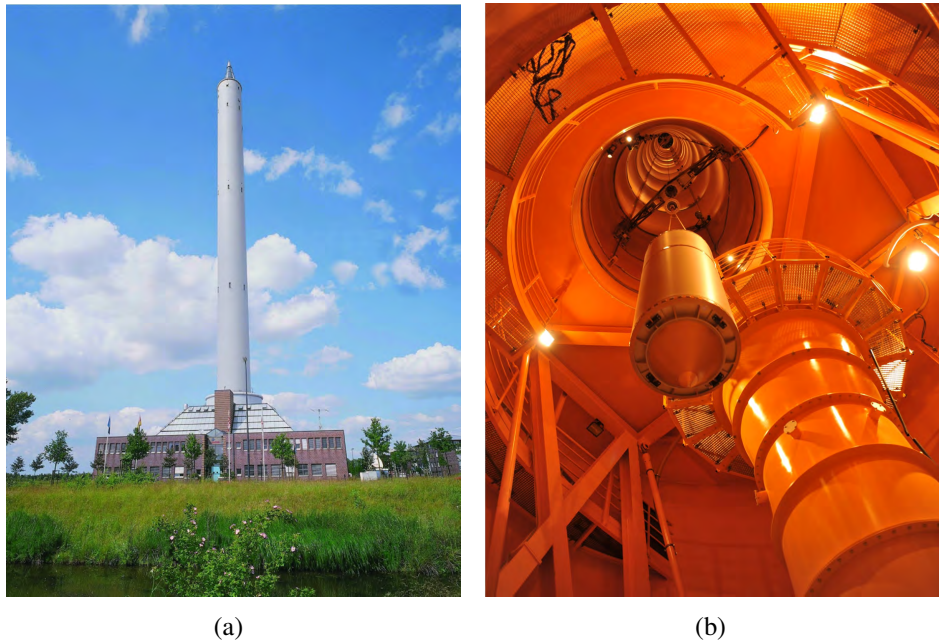


Figure 5.5: (a) Photo of the ZARM Drop Tower (Source: ZARM) and (b) drop capsule inside the tower.

The experiment presented here was conducted at the Drop Tower of the *Center of Applied Space Technology and Microgravity ZARM* (“*Zentrum für angewandte Raumfahrttechnik und Mikrogravitation*”) at the University of Bremen, Germany.

The Tower (see figure 5.5(a)) stands 146 m tall and has a dropping height of 110 m, allowing for 4,74 s of microgravity⁴. Additional use of the catapult system can provide microgravity for up to 9,5 s, but the centrifuge, necessary for this experiment, was at the time not cleared for use with the catapult system.

In preparation for a drop, the drop tube (which is encompassed by the tower) is evacuated down to pressures of about 10^{-2} mbar to avoid air drag during the drop.

The drop capsule (see figure 5.5(b)) with the centrifuge has a usable diameter of 540 mm and a usable height of roughly 600 mm. The inside of the drop capsule is pressurized to one atmosphere during drop, to ensure mechanical stability during deceleration. Any experiment working in vacuum has to be evacuated pre-launch or connected to a vent line linked to the drop tower’s vacuum.

The capsule is stopped in a deceleration chamber filled with polystyrene pallets. During deceleration the capsule experiences peak accelerations of up to 50 g. Appropriate mechanical stability of the experimental setups is therefore imperative.

The experiment is set to investigate low gravity levels. To create this environment inside the drop capsule the setup itself is mounted on a centrifuge with adjustable rotation rate (for details see the following section).

⁴While other means of achieving lower gravity levels allow only for “reduced gravity” (residual accelerations, caused by e.g. spin of the rocket or air drag, can be several percent of Earth’s normal gravity), the drop tower capsule experiences residual accelerations of 10^{-6} g₀, qualifying for the designation “micro”-gravity.

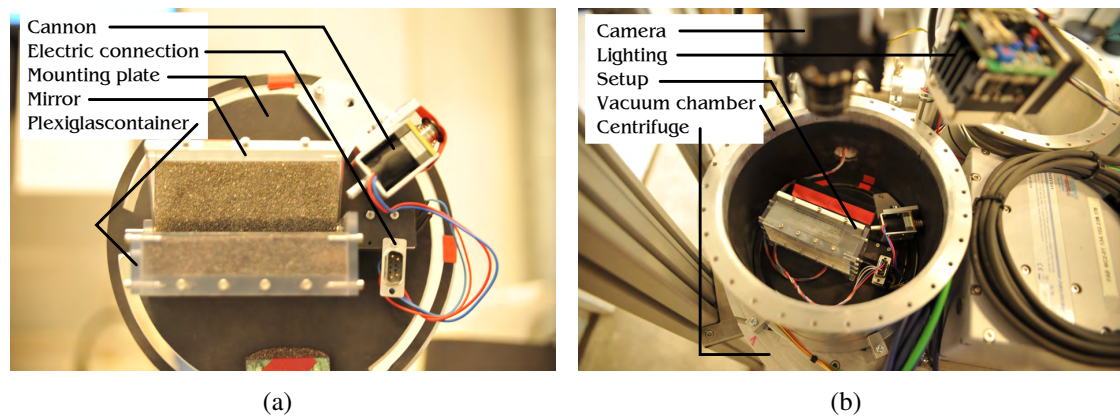


Figure 5.6: Photos of (a) the experimental setup for the MARS-1 material and (b) the setup in the context of the centrifuge.

5.3.2 Design of the experiment

The experimental setup is depicted in figure 5.6(a). It consists of a Plexiglas box of $10 \times 4 \times 2$ cm (length \times depth \times height). The volume of the Plexiglas container is filled with the material to be investigated (for details on the materials see section 5.2). Due to the fairly small amount of HED material, an inlay with dimensions $6 \times 2 \times 1.5$ cm was fashioned to be inserted into the bigger box to hold the HED material. The Plexiglas used for the box is coated with an electrically conductive layer to counteract static charging of the box and avert sticking of the material to the walls.

The box is covered with a mirror that allows observation of the material from the side as well as from the top within a single camera frame.

The mirror is mounted on the shaft of a *Faulhaber* Series 1016G DC-Micromotor with a Series 10/1 *Planetary Gearhead* (reduction ratio 256:1) to enable the mirror to function as a lid when preparing the experiment.

The entire setup is attached to an aluminum plate ($\varnothing = 195$ mm) that was designed to fit into a custom-made vacuum chamber (see figure 5.6(b)). This was done to allow removal of the setup from the centrifuge without dismounting the vacuum chamber.

The vacuum chamber is sealed with a Plexiglas lid that permits the camera, which is attached overhead, to record the entire setup. The seal is not perfect leading to pressure inside the chamber being as high as 40 mbar.

Lighting is provided by two LED panels attached next to each camera. The experiments were recorded using high speed cameras with 2000 FPS⁵ or above at varying resolution.

The projectile is accelerated using a *Tremba* HMA-2622d.001 electromagnet with an attached barrel to hold the bullet (details, see figure 5.7). If supplied with a voltage, the plunger will be pulled into the magnet pushing the projectile out of the barrel at the speed of the plunger, which is controlled by the applied voltage.

⁵Frames per second

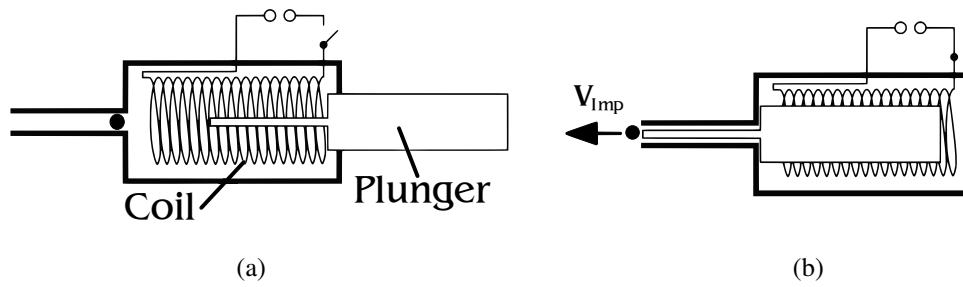


Figure 5.7: Cannon used to accelerate the impactor. If no voltage is supplied (a) the plunger is outside the coil and the bullet rests inside the barrel. If the voltage is connected (b) the plunger gets drawn into the coil and the rod on the plunger pushes out the impactor.

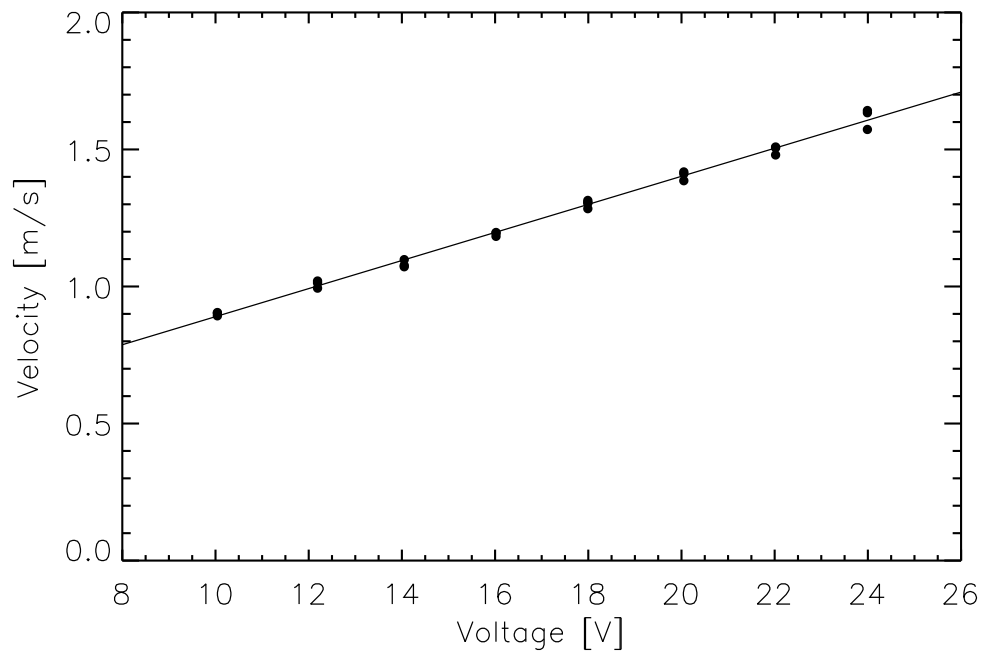


Figure 5.8: Calibration plot of the magnet cannon for a 2 mm-sized impactor.

Figure 5.8 depicts the result of the gauging measurement done in Braunschweig during the ground based campaign (see also table 5.4).

The relationship found was

$$v_{\text{Imp}}(U_B) = 0.0512 \cdot U_B + 0.3779 \quad (5.1)$$

with U_B in V and v_{Imp} in m/s.

To improve upon the experiment during the 1 g measurements, the cannon was removed and, instead, the projectile was dropped into the granular material guided by a narrow tube to avoid vibrations caused by the magnet cannon. A detailed description on the influence of these vibrations is given in section 5.3.6.

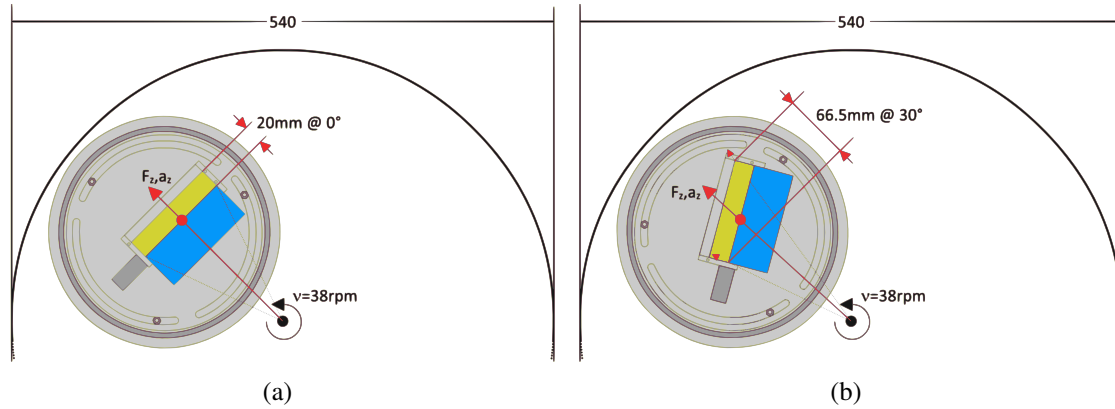


Figure 5.9: Variation of centrifugal force due to changes in the distance from rotation center for 0° (a) and 30° (b) tilt. The big red point denotes the *nominal point*.

The two chambers, each containing one experimental setup, are fixed to the centrifuge platform. By carefully choosing the rotation rate ω of the centrifuge, the centrifugal force and thus the centrifugal acceleration

$$F_c = m \cdot a_{c,0} = m \cdot \omega^2 r_0 \quad (5.2)$$

$$a_{c,0} = \omega^2 r_0 \quad (5.3)$$

acting on the granular materials within the chamber can be tuned to match the gravitational acceleration found on the surface of (21) Lutetia. The center of the granular surface was at approximately $r_0 = 125$ mm distance from the rotation axis. At a rotational frequency of $\omega = 38$ rpm⁶ the centrifugal acceleration at this *nominal point* (defined in figure 5.9) according to equation (5.3) is

$$a_{c,0} = 0.050 \frac{\text{m}}{\text{s}^2} \approx g_L. \quad (5.4)$$

The small diameter of the centrifuge leads to the unwanted effect of a fairly large change in acceleration from the part of the experiment that is closest to the axis of rotation to that part which is farthest from it.

The change in centrifugal acceleration at different points on the surface of the material (depicted in Fig 5.9), relative to the nominal acceleration, is given in table 5.3. The mean tilt angles ($\bar{\alpha}_{\text{HED}} = 34.6^\circ$, $\bar{\alpha}_{\text{MARS-1}} = 23.4^\circ$) were used to calculate the tabulated values.

To minimize the consequences of this effect, the point of impact of the projectile was chosen to be as close as possible to that area corresponding to the planned artificial gravity level. The onset of an avalanche would thus happen as close as possible to the desired value of gravitational acceleration.

The Coriolis force

$$F_C = -2m(\vec{\omega} \times \dot{\vec{r}}) \quad (5.5)$$

can deflect the projectile from its intended path (see figure 5.10).

⁶rpm = Rotations per Minute = 1/60 Hz.

Table 5.3: The change in centrifugal acceleration due to different distances from the rotation center for different positions on the granular surface.

	r [mm]	a_c [m/s ²]	$a_c/a_{c,0}$
Nominal Point	125	0.050	100 %
HED			
Closest Point	113	0.045	73 %
Farthest Point	144	0.058	115 %
JSC MARS-1			
Closest Point	118	0.047	70 %
Farthest Point	152	0.061	122 %

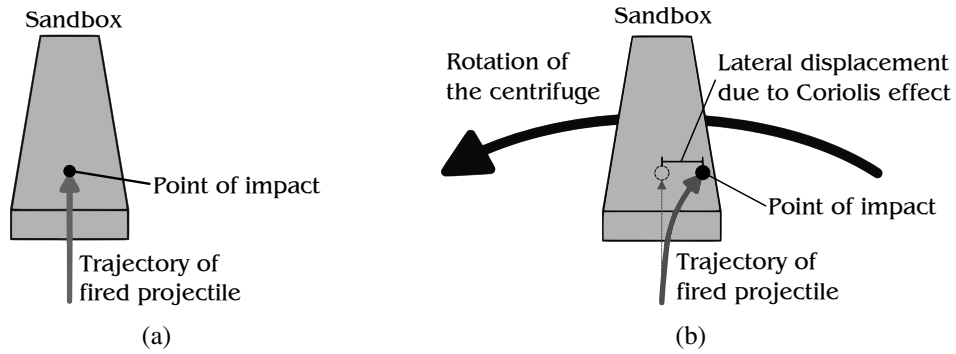


Figure 5.10: Trajectory of the projectile without Coriolis force (a) and with Coriolis force (b).

The distance from the cannon to the granular surface is about $l = 5$ cm. At a given velocity v the projectile experiences the Coriolis acceleration for a time $t = l/v$. Putting in the highest and lowest measured impactor velocities of $v_{Low} = 0.93$ m/s and $v_{High} = 2.15$ m/s, calculating the deflection in the two extreme cases, yields a lateral displacement of the projectile of

$$d_{High} = 0.3 \text{ mm} \quad (5.6)$$

$$d_{Low} = 1.4 \text{ mm.} \quad (5.7)$$

When the cannon is carefully adjusted it is possible to hit the intended target.

5.3.3 Schedule

The Drop Tower Campaign consisted of 10 drops spread out over a week in August 2012. During each drop two experiments (one for each material) were conducted giving a total of 20 low gravity measurements.

Additionally, eight ground based experimental campaigns at the Technical University of Braunschweig were launched in December 2012 (*BS-1*) and February 2013 (*BS-2* through *BS-8*) to investigate the behavior of both materials at 1 g, with a total of 366 measurements. Further details are given in table 5.4.

Table 5.4: Details on the different Seasons of the Experimental Campaign

Season	Purpose
<i>HB</i>	Effect of small scale impacts in reduced gravity
<i>BS-1</i>	Similar to <i>HB</i> in 1g
<i>BS-2</i>	Calibration measurement for magnet
<i>BS-3</i>	Effect of cannon induced vibration on MARS-1 (unsieved)
<i>BS-4</i>	Effect of cannon induced vibration on HED
<i>BS-5</i>	Free fall impact in MARS-1 (unsieved)
<i>BS-6</i>	Free fall impact in MARS-1 ($> 250 \mu\text{m}$)
<i>BS-7</i>	Free fall impact in MARS-1 ($> 800 \mu\text{m}$)
<i>BS-8</i>	Free fall impact in HED

5.3.4 Data analysis

To quantitatively analyze the recorded videos, an image subtraction algorithm was devised.

The 8-bit (gray scale) images (e.g. figure 5.11(a); *BS-3*, No. 27, Im. 12250) are read into an IDL-program one by one and then subsequent images are subtracted from one another. The resulting images are black everywhere except for those pixels that have changed their gray value from the first to the second image. The color of these pixels is set to the absolute of the gray scale value (the subtraction can lead to negative values that cannot be displayed by an 8-bit device) corresponding to the difference between the pixel in the first and second image⁷⁸.

The differences are very subtle even when the image is stretched. To enhance the visibility of motion, the images are digitized, i.e. every non-zero pixel is set to a byte value of 255. This is demonstrated in figure 5.11(b). After doing this it becomes apparent that the difference images are very noisy, making it almost impossible to see the motion.

The images have to be cleaned in order to see the motion properly. This is done by setting all the pixels that have a gray value below the noise level of the image to 0.

To determine the noise level for the measurements, a series of images at the beginning of each measurement with no change in the scenery is taken and subsequent images are subtracted from one another. All the pixels that appear to be moving pixels in these measurements are *a priori* noise. The sum histogram of 5 of these images is created and

⁷Pixels with a non-zero gray value are imaging a part of the physical scenery that has undergone a change from one image to the next. These pixels are henceforth called *moving pixels*.

⁸Moving pixels are denoted to have a non-zero gray value and pixels at rest have the gray value 0 (black). Contrary to this, in all the images shown in this work the color has been inverted for better visibility and ink saving printing.

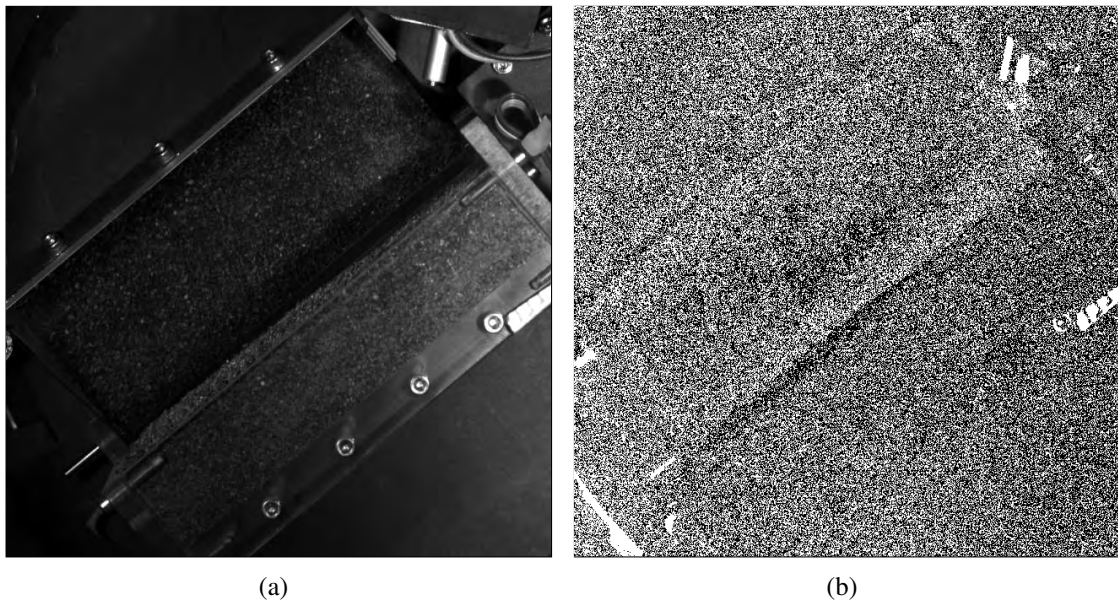


Figure 5.11: The difference image method is illustrated with frame 12250 from *BS-3*, Video No. 27. (a) Original Image1. The image that is subtracted from this one is not shown as the difference between the two are not visible without further processing. (b) Digitized difference between Image1 and Image2, this image was produced by subtracting Image2 from Image1 and setting all pixels that had a non-zero value after subtraction to a gray value 255.

a Gaussian bell curve is fitted to the data, the half width of which is the 1σ noise of the measurement. Figure 5.12 depicts an exemplary noise measurements (Campaign *HB*, Measurement 5 in the HED chamber).

If one discards all the pixels with a gray scale value below the noise level before digitizing it one obtains figure 5.13(a).

Obviously a large number of the moving pixels that are removed are, in fact, *not* noise but belong to the signal. This is caused by the small differences from one image to the immediate next. One can try to remedy the situation by not subtracting immediate neighbors but images that are separated by several time steps.

Figures 5.13(b) and 5.13(c) depict differences of images after five (Im. 12255) and twenty (Im. 12270) time steps, respectively. The gain in signal is apparent as the increased time step leads to a larger change in the scenery resulting in higher gray scale numbers from moving pixels in the un-digitized difference image.

While the neighboring images yield gray scales up to 26 after subtraction (several pixels changed their gray scale color by as much as 26), the 5x time stepping yields a maximum of 71 gray scales and the 20x time stepping yields a maximum of 111. This means that far less pixels are located inside the signal lie below the noise threshold, resulting in a better signal to noise ratio.

The gain in signal comes with a loss of time resolution. A compromise has to be made in order to get the best of both. A time stepping of 5x was selected to give the best results after some trial and error.

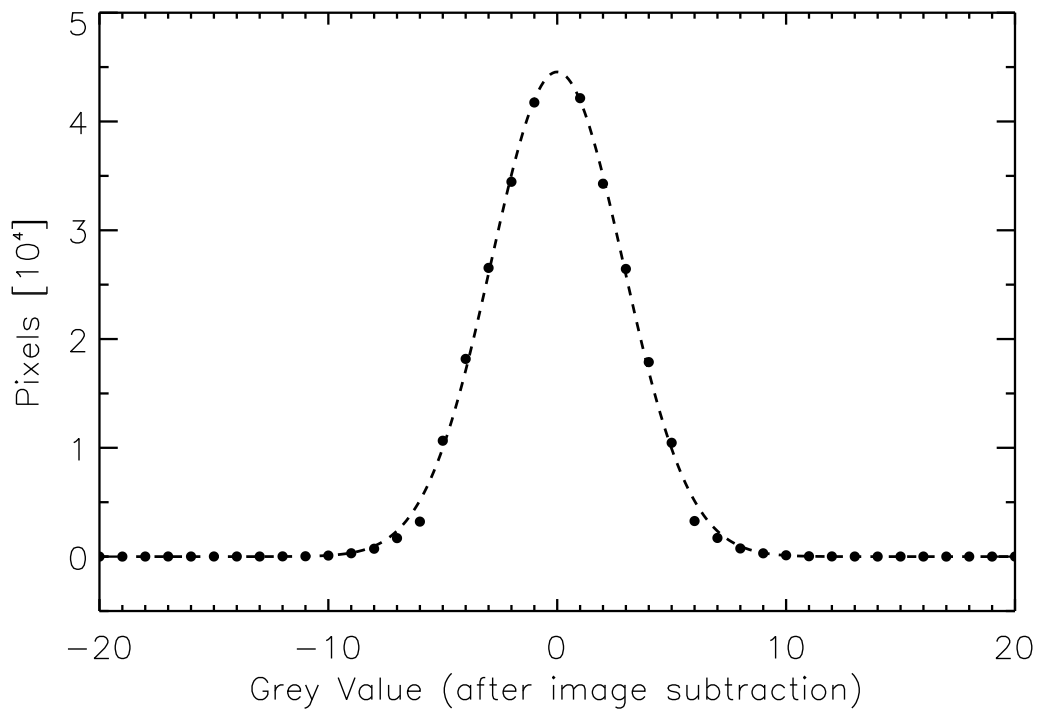


Figure 5.12: Noise for the fifth drop of the HED chamber during the *HB*-Campaign. Shown is the sum histogram of 5 difference images that should not contain a signal at all. Plotted as black dots are the number of pixels in one difference frame corresponding to the given gray value difference. The dashed line is a Gauss fit to that data. The number of pixels with zero gray value is omitted as it does not reflect the noise in the frame.

The next processing step is to rotate the images so that the physically tilted set-up is aligned with the lower edge of the frame. The mirror and the box are then cropped as shown in figure 5.14 to allow for separate analysis.

A video is produced for both areas displaying the time sequence of the subsequent difference images.

To get an estimate on the magnitude of the moving granular material a simple counting of the moving pixels is not sufficient as the cleaning process removes some of the moving pixels which would lead to a fairly gross underestimation. Therefore a smoothing algorithm was applied. The details are described in Appendix A.2. The results are shown in figure 5.15.

To convert the derived quantities from frame units (pixels) to physical units (meters) the known length of the box is measured in pixel units and by comparison to the physical size, the mm per pixel ratio is calculated. It is of the order of 0.2 mm/px varying slightly with the different set ups.

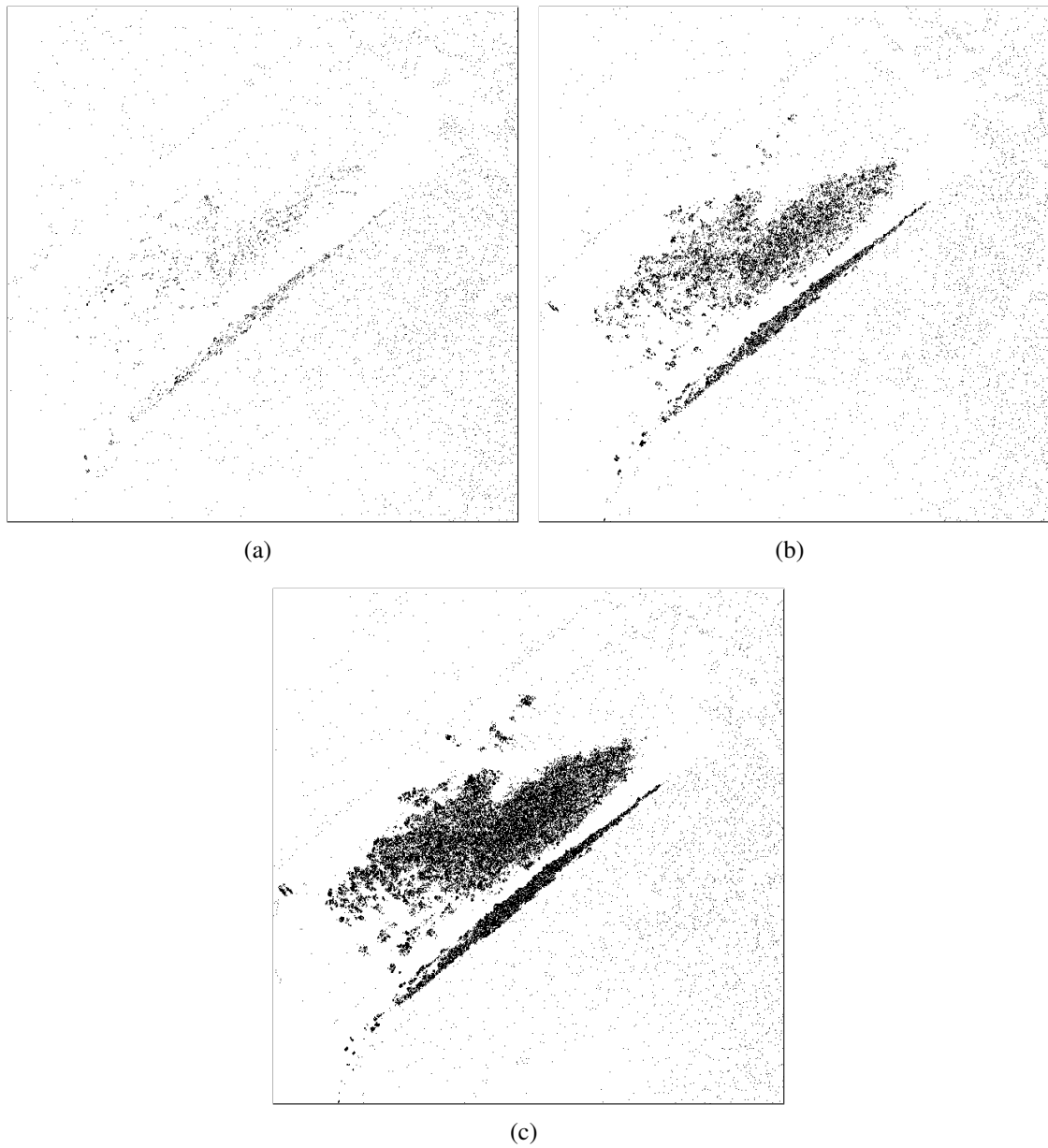


Figure 5.13: Digitized difference between Image1 and (a) Image2, (b) Image5, (c) Image20 with 1σ noise removed. The increase in moving pixels is obvious and caused by the longer time that passed between the images, leading to a greater change in the physical scenery.

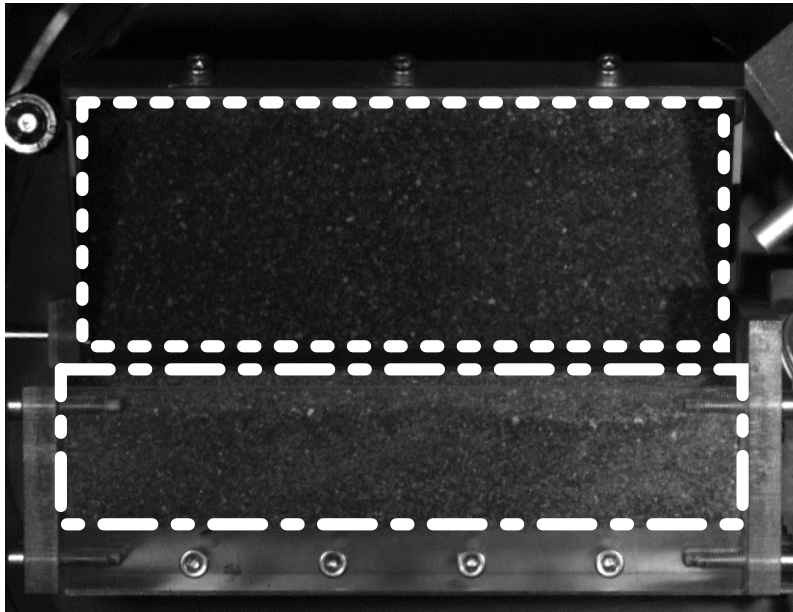
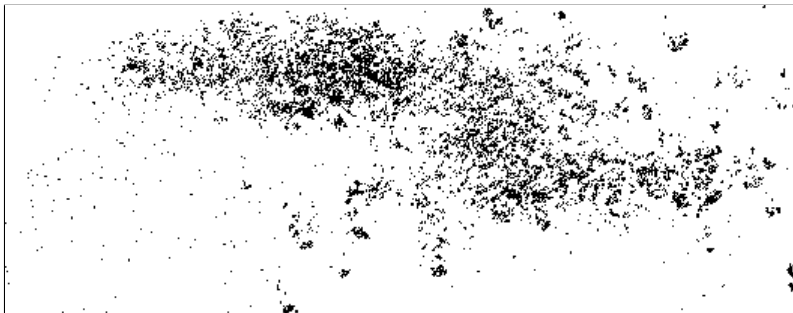
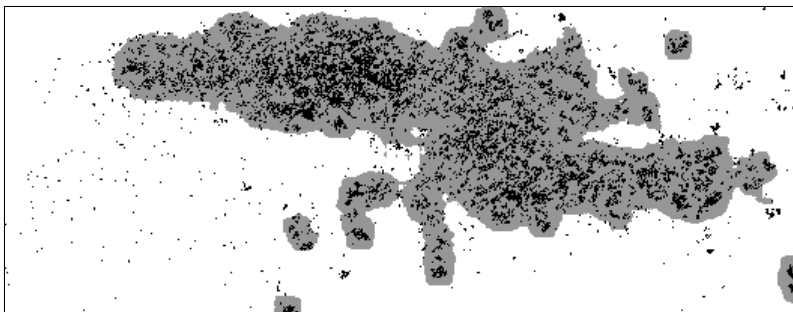


Figure 5.14: Rotated image with crop outlines for mirror (dotted box) and direct (dash-dotted box) view.



(a)



(b)

Figure 5.15: The result of the smoothing algorithm on the noise cleaned 5x difference image of *BS-3*, No. 27, (Im. 384): (a) before, (b) after.

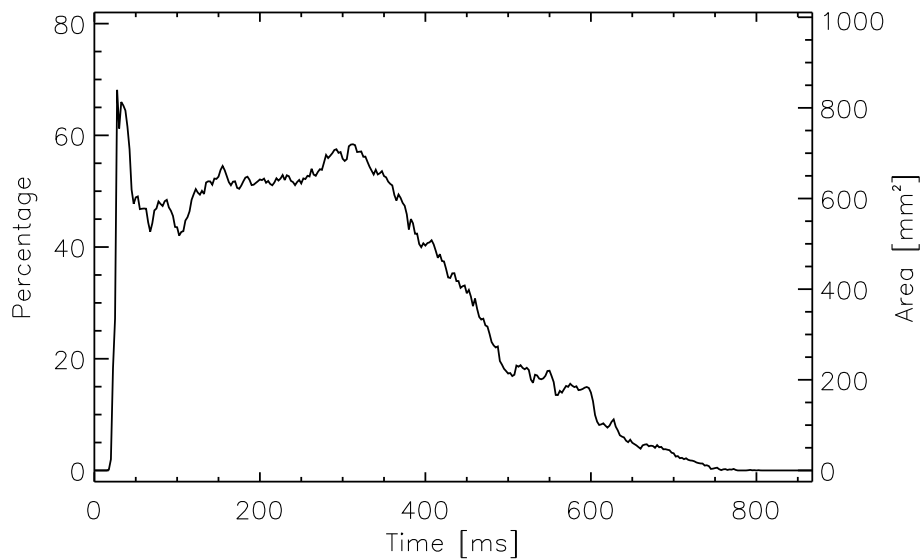


Figure 5.16: Exemplary time series of the surface area that is covered by moving grains (*BS-1*, No. 9).

5.3.5 Results

5.3.5.1 Avalanche Dynamics

To characterize the size and evolution of an avalanche in the experiment the surface of the granular material (as seen in the mirror) is analyzed. The visible area that is covered with moving grains is reconstructed as a function of time, an example is plotted in figure 5.16.

There are several features visible:

- The peak at ~ 40 ms corresponds to the cannon vibrations agitating the material. The effects of this will be discussed in the section 5.3.6.
- Starting at ~ 325 ms the area begins to decrease quickly as this is the time at which the first moving grains reach the bottom of the container leaving the area that is visible via the mirror.

The time after the cannon induced agitation of the material has subsided but before the first grains of the moving bulk reach the bottom of the observable area is of particular interest. If an increase in area is observed during that time, it is reasonable to assume that this trend would continue on. Measurements where such an increase in area is observed shall therefore be treated as indicative of an onsetting avalanche.

Applying this method of identification for an avalanching event on the data set at hand, yields a total of 12 avalanches for the HED and 20 avalanches for the MARS-1 material. Figures 5.17 and 5.18 illustrate the occurrence of avalanches in the context of varying tilt angle and impactor velocity in relation to the cases where no avalanching occurred.

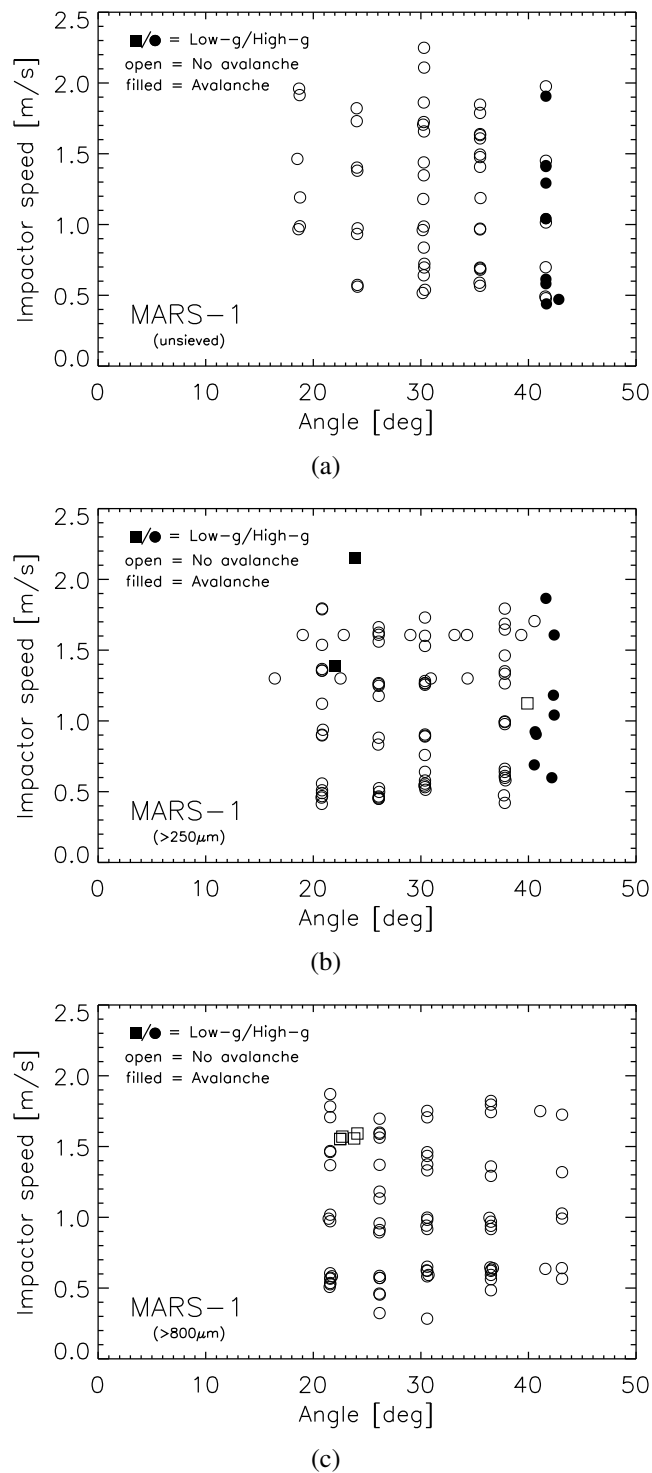


Figure 5.17: Plot showing whether an experiment induced an avalanche or not in the context of varying tilt angle and impactor velocity. Diamonds/Squares denote measurements in reduced/normal gravity, filled/open symbols denote avalanche/no avalanche. Results for MARS-1 (a) unsieved, (b) with grains larger than $250\ \mu\text{m}$, (c) with grains larger than $800\ \mu\text{m}$.

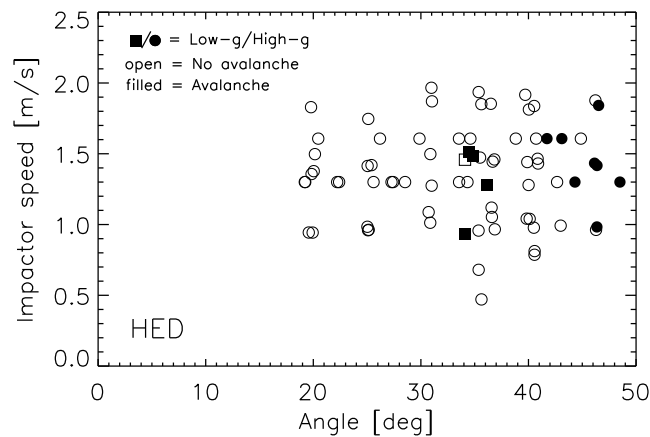


Figure 5.18: Plot showing whether an experiment induced an avalanche or not in the context of varying tilt angle and impactor velocity. Diamonds/Squares denote measurements in reduced/normal gravity, filled/open symbols denote avalanche/no avalanche. Results for HED.

Several trends are obvious in the HED data:

- The avalanching probability is independent of the impactor speed at the observed velocities.
- Avalanches are more likely at higher tilt angles.
- Avalanches occur at lower tilt angles for reduced gravity.

The percentage of avalanches in measurements for tilt angles larger than 40° is 34.8 % (8 out of 23 measurements). For angles between 30° and 40° the percentage is 62.5 % (5 out of 8) considering only reduced gravity measurements and 12.9 % (4 out of 31) considering all measurements.

This observation is not surprising as a slope will naturally become more unstable against perturbations the higher the tilt angle gets. It comes as a surprise though that the material is avalanching at lower angles during the reduced gravity experiments.

The same trends as well as another one can be observed for the MARS-1 data:

- The avalanching probability is independent of the impactor speed at the observed velocities.
- Avalanches are more likely at higher tilt angles.
- Avalanches occur at lower tilt angles for reduced gravity.
- The avalanching probability is a function of the coarseness of the material, with higher probability for finer material.

While there were three cases of avalanches at fairly low tilt angles (all of which in reduced gravity), these measurements have to be treated with caution since the material started flowing already before the cannon was fired. The tilt angle is also well below the static angle of repose making it difficult to explain how an avalanche could happen on its own at all.

A possible explanation could be the release of gas trapped in interstitial pores. The chambers containing the experimental setups were connected to the vacuum of the drop tower via a valve that was only opened shortly before the release of the capsule. This short time might not have been enough for all the gas, trapped in between the grains, to escape. When the mirror was opened the gas had more degrees of freedom to escape from the sand and by doing so it possibly triggered an avalanche.

The dependence of the avalanching probability on the grain size distribution for tilt angles above 40° is given in table 5.5.

Table 5.5: Avalanche frequency for the different sievings of the MARS-1 material for tilt angles between 40° and 50° .

Grain size	Percentage	Total Numbers
Unsieved	57.1%	8/14
> 250 μm	72.7%	8/11
> 800 μm	0%	0/8

The coarser grains lead to a more stable packing which is reflected also in the static angle of repose (see table 5.2). The coarser grains are also similar in size to the impactor. This makes an agitation of a large number of grains more difficult and thus an avalanche less likely.

5.3.6 Performance

The performance of the experiment did not fully meet the expectations due to several circumstances both of which will be described in detail in the following sections.

5.3.6.1 Mechanical limitations

Due to the design of the mounting mechanism for the removable plate, the tilt angle of the box relative to the artificial gravity vector could not be adjusted to the desired values. The tilt angles that could be achieved with this mounting were $\alpha_{\text{HED}} \lesssim 35^\circ$ and $\alpha_{\text{MARS-1}} \lesssim 26^\circ$. Both ranges are below the respective static angle of repose.

In addition, the mirror got stuck during the opening phase on several occasions. This was caused by small grains that entered the rotation axis of the mirror creating additional friction that could not be overcome by the motor. As a result, the projectile ricocheted off the frame of the mirror, missing the target.

5.3.6.2 Cannon induced vibrations

The design of the firing mechanism was subject to certain restrictions. The cannon had to allow for a fast and controlled acceleration of the projectile while being small enough to fit into the vacuum chamber.

The cannon used in the experiments accelerates the projectile via a plunger that gets drawn into the corpus of the magnet and pushes out the projectile in the front (see section

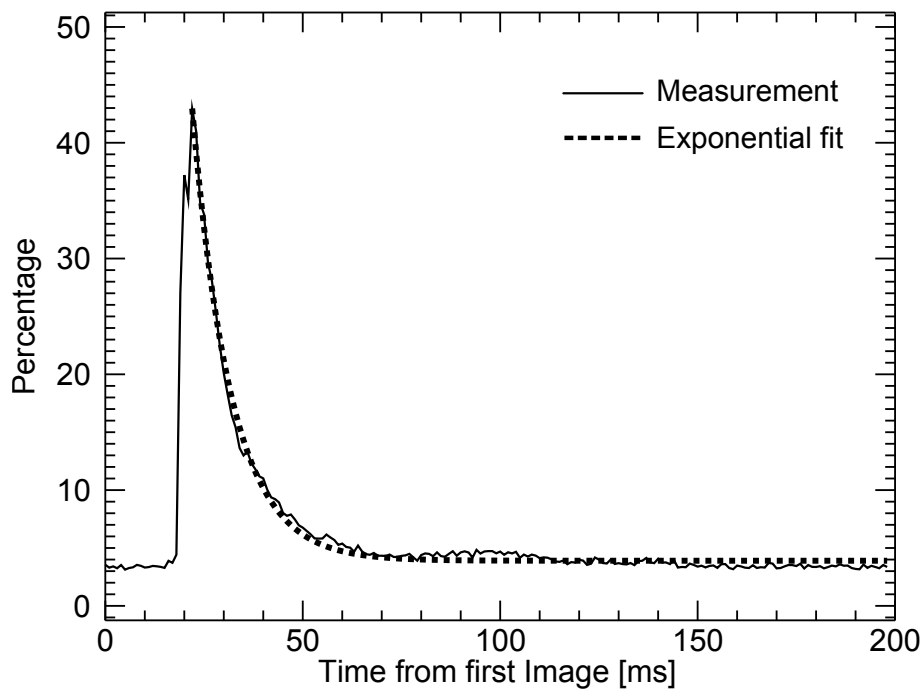


Figure 5.19: Exemplary time series of percentage of moving pixel in the side view of the box (*BS-4*, No. 35). No projectile was fired during this measurement. All the motion is caused by mechanical waves that were excited during the cannon fire. The solid line is the measured data, the dashed line is the exponential fit.

5.3.2 for details). To accommodate the desired acceleration characteristics the cannon had the disadvantage of an abrupt stopping of the plunger that was providing the thrust, i.e. the plunger was driven into the magnet until it was stopped mechanically by the hull of the magnet.

This abrupt stop causes vibrations that are translated via the mounting of the cannon onto the entire setup. This causes an undesirable stirrup of the material under investigation. In the worst case these vibrations could even trigger a slope failure in the material.

To characterize the influence of the vibrations, additional measurements were conducted during the second ground based campaign. The experiments were carried out as described above but without projectile. This means that any outcome would be solely due to the influence of the cannon shock.

Once agitated, the material takes some time to come to rest again. This can be seen in figure 5.19. The blue line represents the measurement, the red line is the result of an exponential fit to the data starting at the maximum of the blue line.

The half life of this exponential decay is a measure of how long the cannon induced vibrations can influence the overall performance of the experiment. The half lifes for the *HB* and *BS-1* measurements as well as the reference measurements *BS-3* and 4, which were dedicated to investigating this phenomenon, were extracted by fitting. The results are plotted in figure 5.20.

The mean half lifes for the MARS-1 (reduced gravity measurements and those at 1 g) are

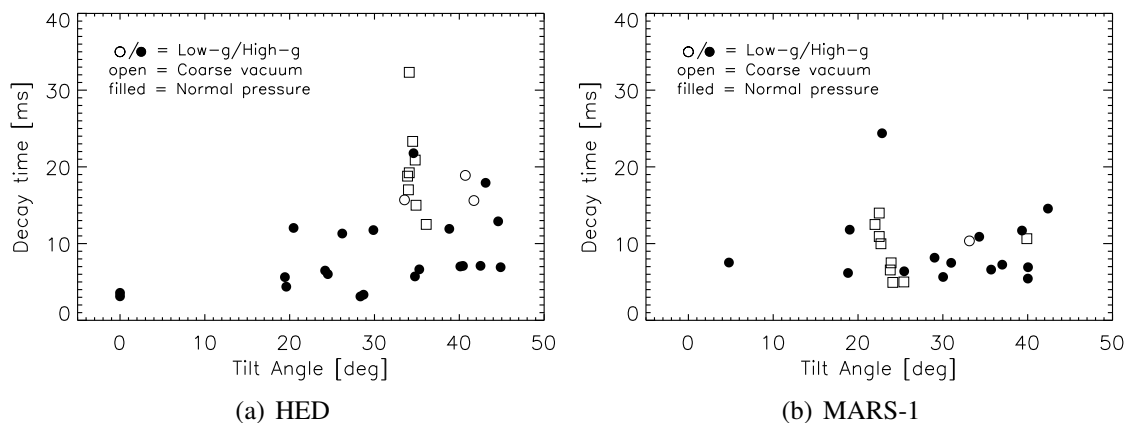


Figure 5.20: Half lives of the exponential curves fitted to the time series of moving pixels in the box view of (a) the HED measurements in Campaigns *HB* and *BS-1* and *BS-4* and (b) the MARS-1 measurements in Campaigns *HB* and *BS-1* and *BS-3*.

$$\begin{aligned}\bar{\tau}_{\text{Red. g}} &= 9.1 \pm 1.0 \text{ ms} \\ \bar{\tau}_{1\text{g, 0bar}} &= 10.41 \text{ ms (single measurement)} \\ \bar{\tau}_{1\text{g, 1bar}} &= 9.4 \pm 1.3 \text{ ms.}\end{aligned}$$

The averaged numbers agree within the error bars, but the value for the vacuum measurement in 1 g is slightly too high. But since this is only a single measurement the statistical significance is minimal.

The mean half lives for the HED (reduced gravity measurements and those at 1 g) are

$$\begin{aligned}\bar{\tau}_{\text{Red. g}} &= 22.1 \pm 5.0 \text{ ms} \\ \bar{\tau}_{1\text{g, 0bar}} &= 16.7 \pm 1.1 \text{ ms} \\ \bar{\tau}_{1\text{g, 1bar}} &= 8.4 \pm 1.1 \text{ ms.}\end{aligned}$$

While the numbers for reduced gravity and normal gravity with coarse vacuum agree within the error bars, the value for normal gravity at ambient pressure is distinctly lower. As this was not observed with the MARS-1 material, it seems to be related to the different shape of the grains. It is possible that the flat shape of the larger grains provide larger friction with the surrounding air, hindering the larger particle to gain to much momentum during the cannon shock phase, making the bulk of the material settle faster.

The half lives for the HED measurements are about two times as long as those for MARS-1. This can most likely be attributed to the smaller amount of HED material that receives the same amount of kinetic energy. This energy, introduced to the system by the cannon, gets very effectively dissipated in granular material through collisions. The larger amount and finer grains of MARS-1 material allow for a faster dissipation of the energy and thus a shorter half life of the agitation.

The measured half lives are short compared to the length of one measurement so the immediate effect of an increased number of moving pixels can be readily handled in the

data analysis. The 1 g reference measurement though showed that for tilt angles close to the static angle of repose the cannon induced vibrations input enough energy into the system to trigger a sliding event. Since all of the measurements in reduced gravity were conducted at tilt angles well below ϑ_c , the vibrations can be considered negligible for the outcome of the measurements. During the ground based experiments where the cannon was used (*BS-1*) care needs to be taken when analyzing the data recorded at high tilt angles.

5.4 Importance of minor impact events

It is obvious that an avalanche in a granular material is more easily excited when material is tilted to an angle that is close to the static angle of repose. The surface grains that are trapped in local potential energy minima need less energy to jump out of their respective troughs. This expectation has been confirmed by the measurements described in this chapter.

It is of interest to find out how this process may influence the surface structure of an asteroid.

Experiments on high speed impacts of mm-sized projectiles into porous and granular material show that a significant fraction of the produced ejecta with masses well below one gram are ejected at velocities below 2 m/s (Cintala *et al.* 1999, Onose and Fujiwara 2004).

The distance that a particle will fly depends for an airless target body only on the ejection velocity v_e and the angle φ_e under which the particle is ejected. Using the formula for the ballistic range D on a small body (equation 6.1.3 in Melosh (1989))

$$D(v_e, \varphi_e) = 2 \cdot R \cdot \tan^{-1} \left(\frac{(v_e^2/R/g) \cdot \sin(\varphi_e) \cdot \cos(\varphi_e)}{1 - (v_e^2/R/g) \cdot \cos^2(\varphi_e)} \right) \quad (5.8)$$

where R is the radius of (21) Lutetia's equivalent sphere ($R_{\text{Lut}} = 49$ km), one obtains ranges for ejecta of up to 86 m. The ranges obtained with equation 5.8 are plotted in figure 5.21.

This means that on a body like (21) Lutetia, these particles will fly far enough from their primary impact site to fall into material that is undisturbed by the primary impact.

Keeping this slow impactor production mechanism in mind, one can estimate, how many secondary impacts per m^2 are needed in order to resurface a patch of $1 \times 1 \text{ m}^2$ tilted close to the angle of repose.

From the experiments an average length-to-width ratio of 8.2 for the induced avalanches was derived⁹.

A set of Monte Carlo simulations where secondaries impact into a steeply tilted slope were done. Each impact happened at a random position and could trigger an avalanche with a probability of 57% (taken from table 5.5). The resulting avalanche was assumed to have a triangular shape with the above mentioned dimension ratio.

⁹This means that an avalanche that traveled 8.2 m from its origin, will have a width of one meter.

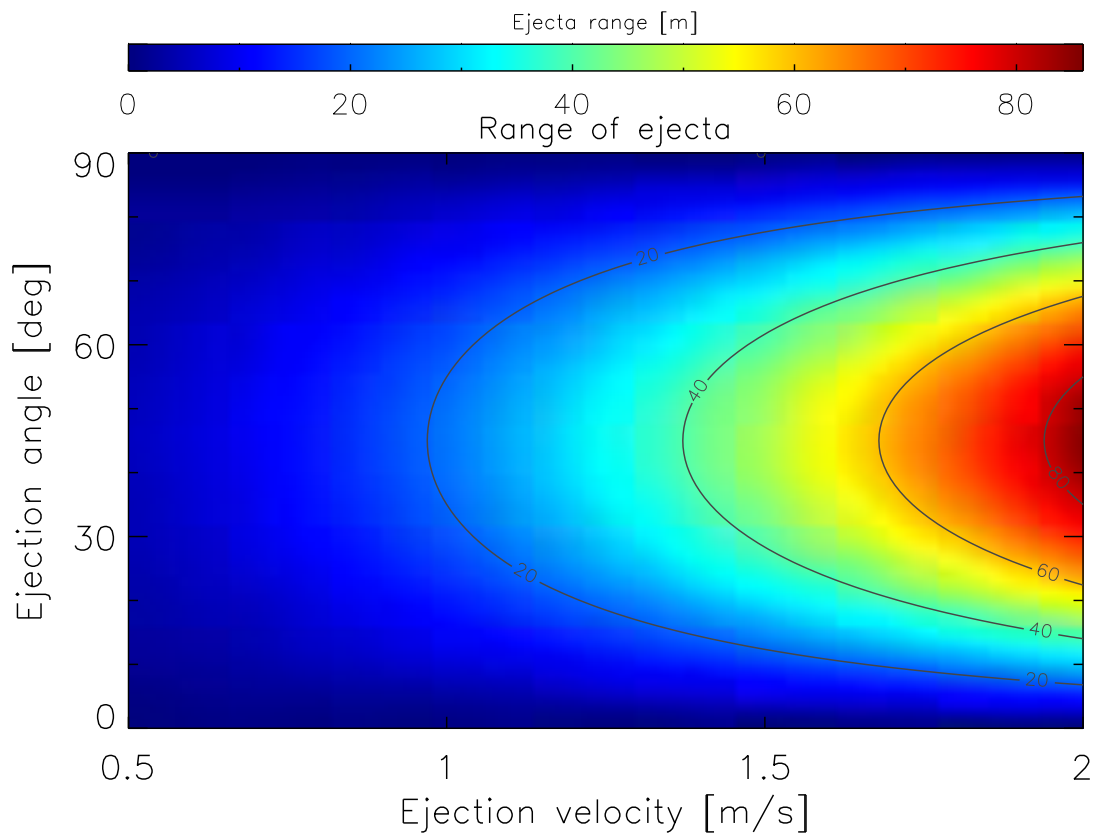


Figure 5.21: The range of impact ejecta, ejected at angles φ_e between 0 and 90° and velocities v_e between 0.5 and 2 m/s calculated with equation 5.8 (equation 6.1.3 in Melosh (1989)).

The number of impacts per square meter¹⁰ necessary to resurface a 1 m² patch strongly depends on how close the patch is to the ridge of the hillside. Monte Carlo simulations for patches located at the ridge and 1 to 4 m below the ridge were carried out. An exemplary simulation result for a patch located at the ridge and 3 m below the ridge are shown in figure 5.22.

To extrapolate how long a complete resurfacing of the patch would take, the simulations were carried out in such a way that the number of impacts per m² necessary to resurface 25%-75% (in 5% steps) of the patch was recorded for 10000 simulation runs. For each simulation run, a histogram illustrating how many impacts were necessary was created. Exemplary histograms for 50% resurfacing ratio for patches at the ridge and 3 m below are plotted in figure 5.23.

The mean number of impacts as a function of distance from the ridge for different resurfacing ratios are given in figure 5.24(a) together with exponential fits to the data to extrapolate to larger distances from the ridge.

¹⁰The simulations were set up in way that only an area where avalanches could actually go across the observed patch was created. The number of impacts into this area was afterwards normalized by the size of the area to get a meaningful number.

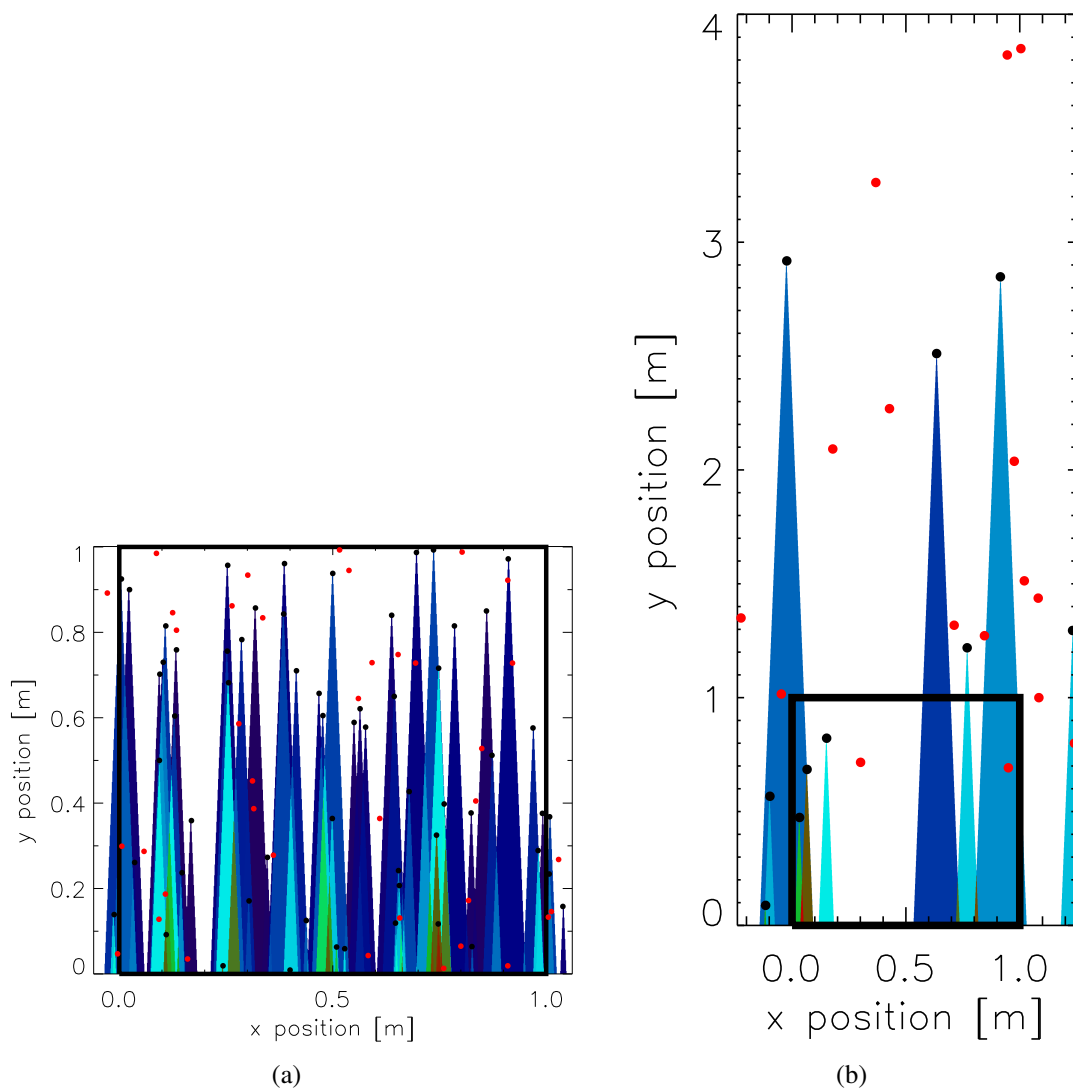


Figure 5.22: Monte Carlo simulations of impact events triggering avalanches. The area resurfaced by an avalanche has a color other than white (the color shade is supposed to guide the eye and has no physical meaning). The filled circles indicate a simulated impact: black/red circles represent impacts that did/did not trigger an avalanche. Sub-figures (a)/(b) show the results for a simulated patch located right beneath the ridge/3 m below the ridge. The simulations were stopped when more than 50% of the framed area had been covered by avalanches. For these specific simulations it took 97/26 impacts into a total resurface of 1.12 m²/8.01 m².

The exponential function

$$f(x) = a_0 \cdot e^{a_1 x} + a_2 \quad (5.9)$$

and especially the fit parameter a_2 are used to find the number of impacts that are necessary to resurface different ratios of the patch at very large distances, where the impact number no longer depends on the distance to the ridge.

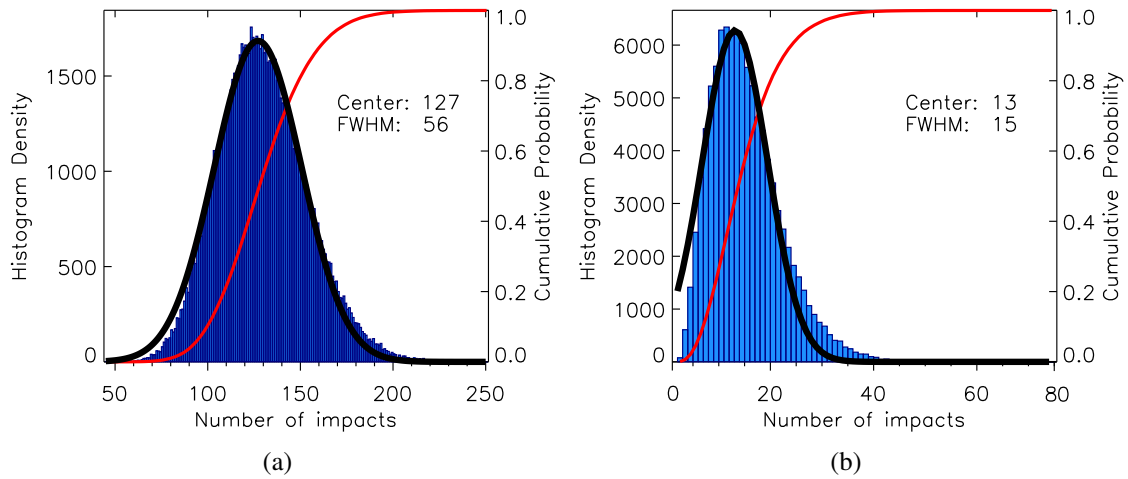


Figure 5.23: Exemplary histograms for the number of impacts needed to resurface 50% of the patch by avalanches for a patch located (a) at the ridge, (b) 3 m below the ridge. The gray line shows the histogram in cumulative form. Also plotted is a Gaussian fit to the histogram to measure the mean number of impacts for this parameter variation.

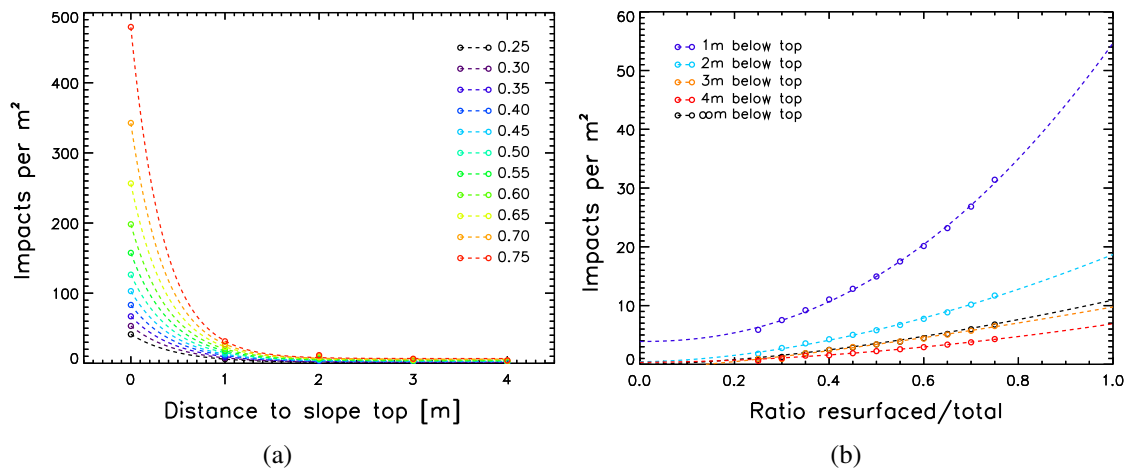


Figure 5.24: Mean number of impacts per m^2 for different (a) distances to the ridge and (b) resurfacing ratios. The circles are the data values, the dashed lines are fits of an (a) exponential decay function and (b) a geometric function. The black circles and line in sub-figure (b) are data points that come from the exponential decay functions in sub-figure (a).

The extrapolated data as well as the respective data from the Monte Carlo simulations are plotted in figure 5.24(b). A geometric function of the form

$$f(x) = a_0 \cdot a_1^x + a_2 \tag{5.10}$$

was found to be a best fitting function to that data set.

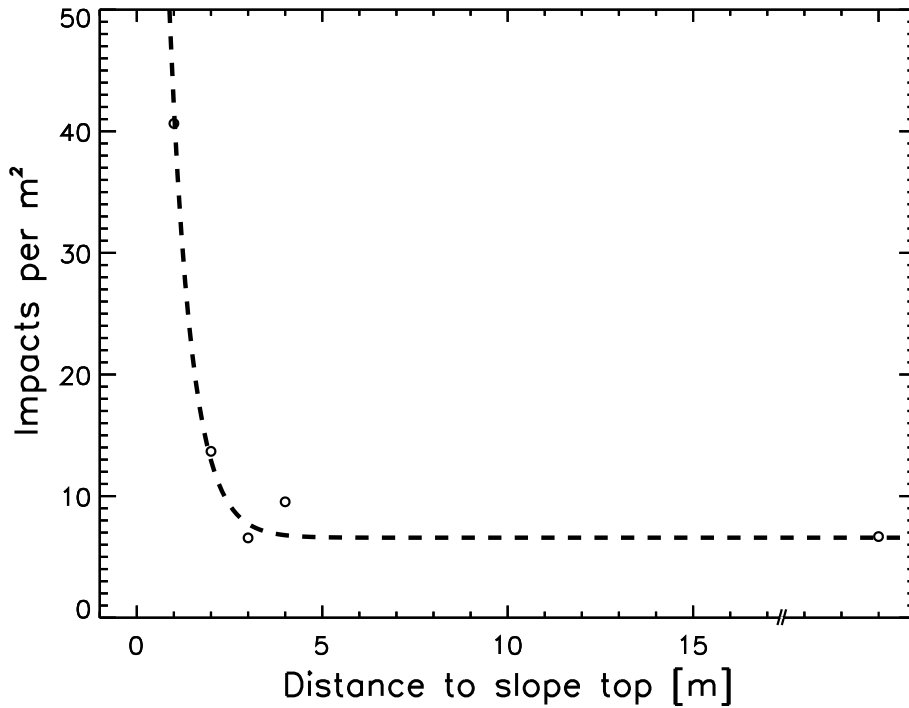


Figure 5.25: Mean number of impacts per m^2 for 100% resurfacing ratio as a function of the distance from the ridge. The data points extrapolated from figure 5.24(b) are fitted with an exponential function in order to estimate the number of impacts at any given distance from the ridge.

The extrapolated mean number of impacts to resurface the entire patch (100%) are shown in figure 5.25. Again an exponential function is fitted to the data points. The best fitting curve is

$$f(x) = (197 \pm 11) \cdot e^{(-1.72 \pm 0.04)x} + (7 \pm 0). \quad (5.11)$$

This means that for large distances from the ridge an average of 7 impacts per m^2 suffice to resurface an area of 1 m^2 .

Using the flux of interplanetary particles with masses of about 10^{-2} g $F \approx 10^{-12} \text{ m}^{-2}\text{s}^{-1}$ from a model by Grün *et al.* (1985) as a proxy for the meteoroid flux in the main belt and the estimate that any impact will create up to 500 large enough spalls (Onose and Fujiwara 2004) any square meter on a slope of high enough steepness would be resurfaced within 1 to $6 \cdot 10^4$ yr, depending how close it is to the ridge. As the upper portion of any slope will take the longest to get covered by avalanches, the assumption can be made, that a slope of any size will be completely resurfaces within 10^5 yr.

This estimate is based on a number of assumptions but should suffice to show the importance of these minor events on the global surface structure and surface evolution of an atmosphereless, planetary body.

6 Simulations of Avalanches

6.1 DEM Simulation

The experiments summarized in the previous chapter allow the study of macroscopic effects of minor impacts into granular material. To understand the dynamics of impacts on a microscopic level, computer simulations need to be carried out and analyzed. The behavior of particles in terms of kinetic energy and velocity distribution can be studied most effectively with the help of *Discrete Element Method* (DEM) modeling.

DEM codes simulate any granular system by creating an ensemble of spherical particles of a user-defined size or size distribution with specified locations and initial velocities within a simulation volume. Forces acting on each particle include e.g. gravity, particle-wall repulsion and inter-particle friction. The net force of all integrated interactions acting on a particle at a given time step can then be used to calculate the position and velocity of the particle at the next time step.

To simulate the minor impacts investigated in the experiments, the parallel DEM software *ESyS-Particle*¹ was used.

The goal of these simulations is to quantify how the energy introduced to a system of particles by an impact event is distributed within the ensemble. Questions to be answered are:

1. How much energy gets dissipated due to friction?
2. What is the direction of energy transport?
 - Is the energy equally distributed?
 - How much energy gets transported into deeper layers?
 - How much energy is retained near the surface?
 - Is the energy flow close to the surface correlated to the direction of gravity or the direction of the impactor velocity?
3. Does the system dilate (i.e. does the porosity change)?

¹www.launchpad.net/esys-particle

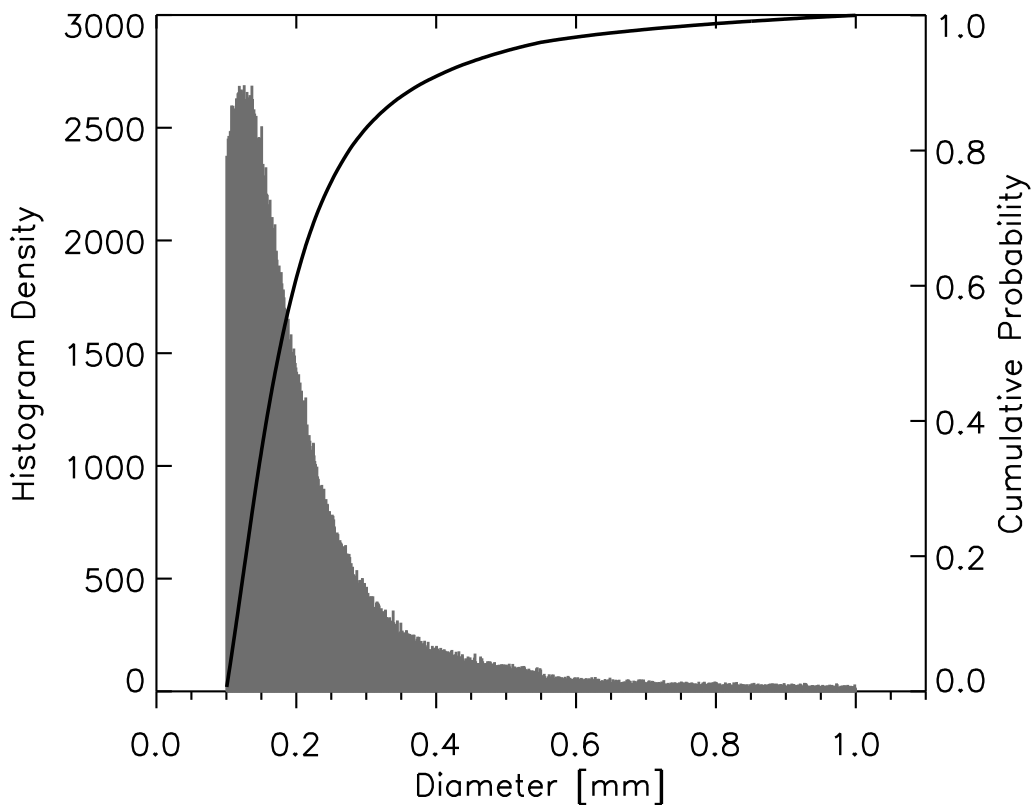


Figure 6.1: Cumulative and differential grain size histogram from *RadomBoxPacker*.

6.2 Setup of Simulation Environment

The first step in order to simulate a small scale impact into granular matter is to create an ensemble of particles that act as the target material. To ensure that the simulation results can be applied to the impact experiments, the target material was modeled to resemble the JSC MARS-1 material introduced in chapter 5.2.

Particle ensembles for *ESyS-Particle* Simulations can be created via the *GenGeo*² library. The tool can create arrangements of particles and allows specification of the minimum and maximum radius of the particles. A random packing of the particles was chosen to represent the mixed state of the granular material in the experiment.

Given a certain range of particle radii, the packing algorithm (called *RadomBoxPacker*) creates a grain size distribution (GSD) that follows a power law (see figure 6.1).

Morris *et al.* (1993) give the mass fraction for different particle size ranges for the MARS-1 material. Figure 6.2 shows a plot of the data given in table 2 in Morris *et al.* (1993) together with the mass distribution corresponding to the GSD coming from the *RandomBoxPacker*.

In order to make the simulation as accurate as possible, the particle size distribution needs to be modified to resemble the actual data more closely. To accomplish this, four different volumes were packed with grain sizes given in table 6.1.

The resulting particle ensemble comprises roughly 50,000 particles and has a grain

²<https://launchpad.net/esys-particle/gengeo>

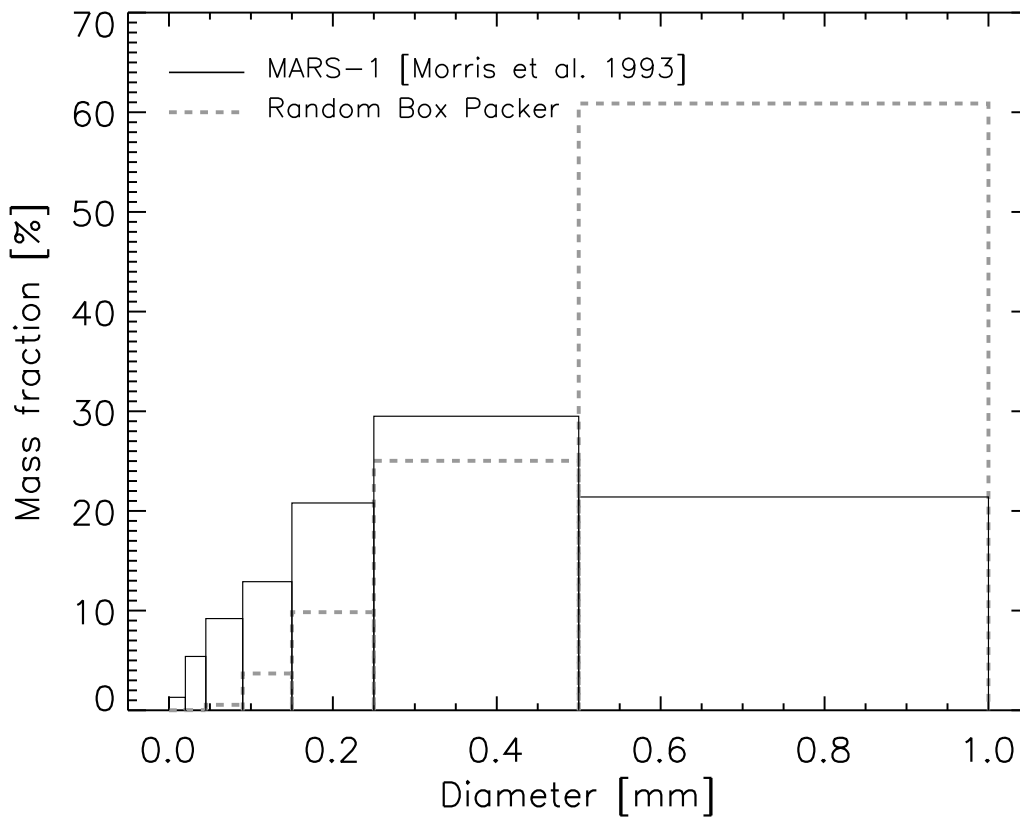


Figure 6.2: Mass fraction for different grain size ranges. The solid black lines correspond to the data of (Morris *et al.* 1993) for MARS-1. The dashed lines correspond to the GSD produced by the *RandomBoxPacker*.

Table 6.1: Diameter ranges used to create the particle mixing.

100 μm	$< d_1 <$	150 μm
150 μm	$< d_2 <$	250 μm
250 μm	$< d_3 <$	500 μm
500 μm	$< d_4 <$	1000 μm

size distribution that accurately reproduces the mass fraction from Morris *et al.* (1993).

Simulating a box equivalent to the one described in the previous chapter would have been computationally very expensive. To allow for the generation of physically meaningful results in a reasonable time frame, the size of the simulation box was reduced to 10x10 mm with a height of about 3.5 mm, with a surface impact in the center.

The mixing of the different particle sizes was achieved through repeated shaking of the simulation box. Figure 6.3 plots the cumulative depth histograms for all four diameter ranges.

The slope for all the lines is almost the same, indicating an even mixture of the different size regimes.

After the mixing process, the particle ensemble has to settle. This means the simu-

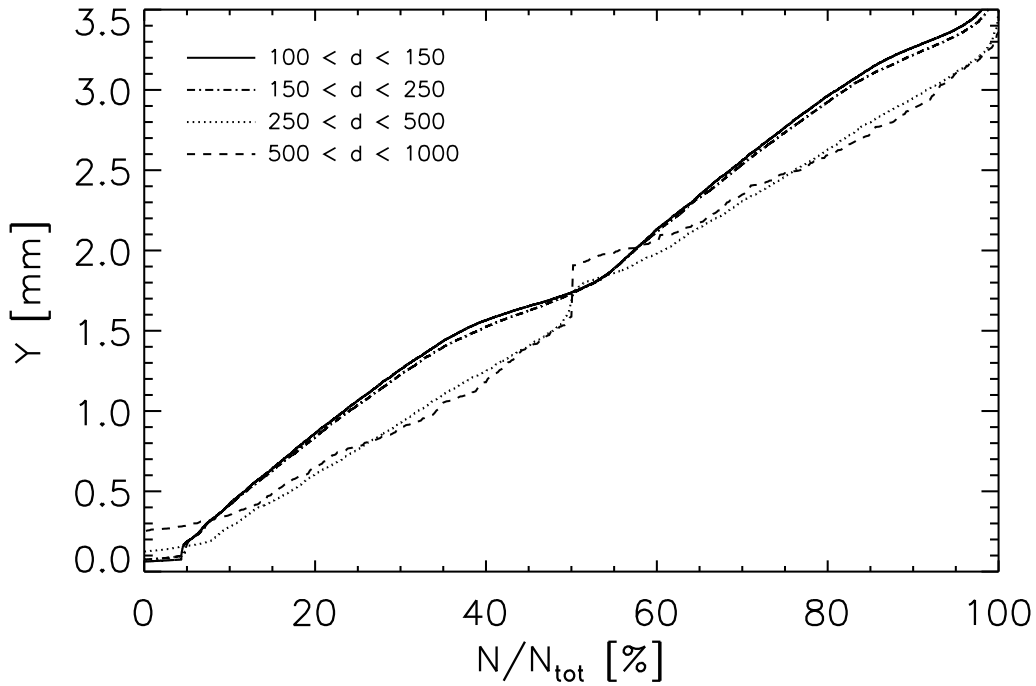


Figure 6.3: Cumulative depth histograms of the different particle sizes after the mixing process. Lines with the same slope indicate even mixtures of the respective particle ensembles.

lation is run without impact event so that the particles move solely due to the influence of gravity. This results in a geometry where all particles have moved to their respective minimum of potential energy, i.e. the particles will no longer move as long as there is no outside interference.

The particles have been allowed to settle with different orientations (slope angles) relative to the direction of the gravity vector. This is done because the minimum potential energy configuration differs for different orientations of the gravity vector.

A simulation specific problem occurred during this settling process: *ESyS-Particle* does not allow for frictional interaction between particles and walls. This results in an unhindered motion of boundary particles (i.e. particles in contact with the wall) in any direction dictated by the net force acting upon them. A particularly undesirable effect of this is that particles at the lower end of the slope can easily be pushed upward along the wall without resistance. Figure 6.4 illustrates this uphill motion.

An artificial friction has therefore been introduced for the wall limiting the downward motion of the particles. The friction was realized by attaching the boundary particles to their respective wall via an unbreakable elastic spring. Those particles attached to the wall can no longer move away from their contact point but still undergo frictional interaction with the other particles.

The settling process reduces the porosity of the particle ensemble to its final value of $\phi \approx 31\%$, which is slightly below the porosity for a random close packing of monodisperse spheres $\phi_{\text{RCP}} \approx 36\%$.

The static angle of repose for this block of particles has been determined to be $\sim 31^\circ$.

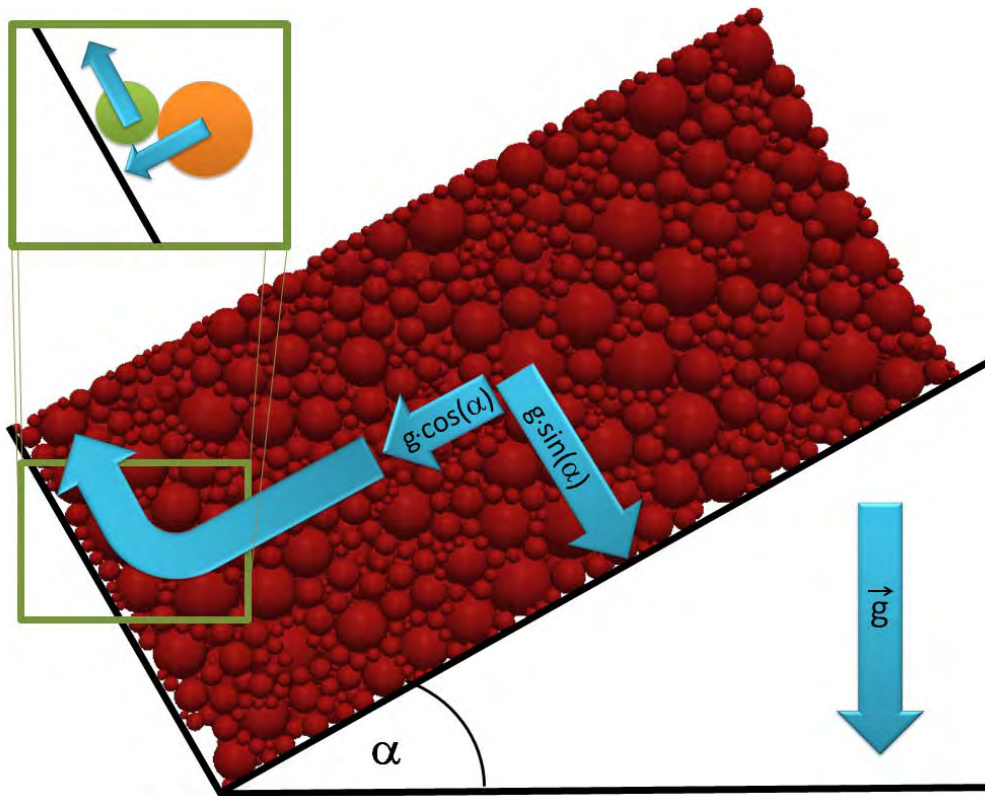


Figure 6.4: Influence of wall friction on the motion of particles. The blue arrows indicate the direction of forces. The gravitational attraction points downward and can be split into two components: one perpendicular to the tilted floor of the box ($F_{\perp} = g \cdot \sin(\alpha)$) and one parallel to it ($F_{\parallel} = g \cdot \cos(\alpha)$), where α is the tilt angle of the box. The force parallel to the floor will push all particles towards the sidewall at the lower end of the box. Any particle that is in contact with the frictionless wall (we shall call these particles *boundary particles*) but has no other particle on top of it (green sphere in the inlay) will experience not only the force pushing it against the wall but also a force exerted by the particles farther up the box (orange sphere in the inlay) that tends to push the boundary particles up the wall.

This was accomplished by tilting the box of particles to ever higher angles (or to be more precise by changing the direction of the gravity vector within the simulation environment) until the topmost layer of particles started moving down the slope.

After the particles have been settled, the impact simulations were started. These simulations consist of the previously described set of particles (henceforth referred to as “target”) and a particle (“impactor”) that will impact into the target. The impact geometry can be seen in figure 6.5.

The impact will take place at different incidence angles i , i.e. angle between the local normal to the surface and the impactor velocity vector. i is varied between -75° and 75° in 25° steps. The tilt angle of the target material is varied between 0° and 30° in 10° steps. For those 28 orientation permutation simulations were conducted for a gravitational acceleration of $1 \cdot g_0$ and $5 \cdot 10^{-3} g_0$ giving a total of 56 simulations.

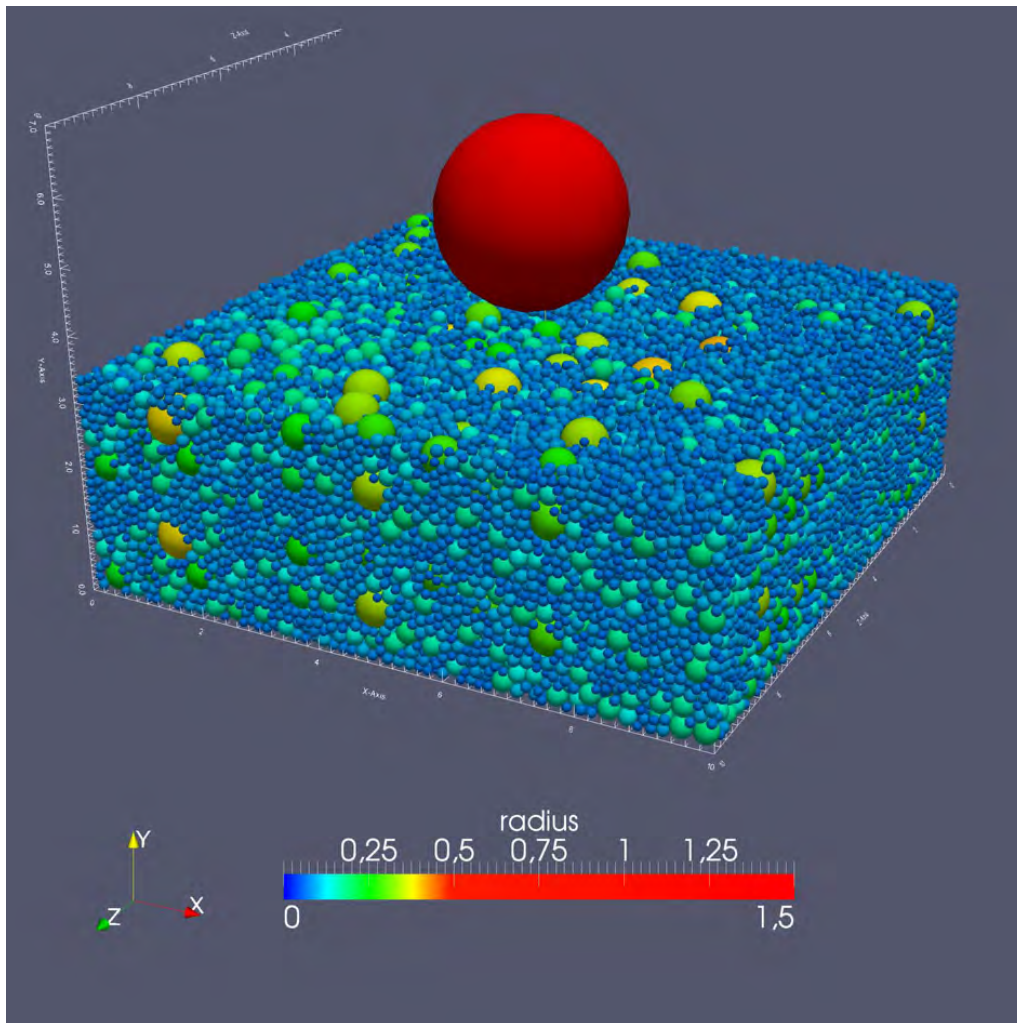


Figure 6.5: Impact geometry consisting of the target particles which are at rest and the impactor which has a speed of 1 m/s. The radii are given in Millimeters.

6.3 Analysis

ESyS-Particle has the option of producing so-called snapshots of the simulation at regular intervals. These snapshot files contain all important parameters (see below) of all the particles within the simulation. Additionally, the total kinetic energy (translation and rotation) for each particle can be printed to file for any given time step.

For every time step t the snapshot files contain, for every particle i of the target block and the impactor,

1. the radius r_i ,
2. the mass m_i ,
3. the Cartesian coordinates x_i, y_i, z_i
(in accordance with *ESyS-Particle* nomenclature y will be the vertical coordinate, $+y$ being upward),

4. the velocity components $v_{x,i}$, $v_{y,i}$ and $v_{z,i}$ and
5. the rotational frequency $\omega_{x,i}$, $\omega_{y,i}$ and $\omega_{z,i}$.

In a supplementary file, the energy E_i for every particle (including the impactor) is stored. Individual particles can be traced using their unique particle ID. If it is desired any particle can be given one particle tag identifying it as member of a user defined group. This was done during the mixing of the different particle sizes to easily differentiate between particles of different size regimes.

To quantify the amount of energy the impactor introduces to the system, several variables were calculated for every snapshot and shall be described in the following section.

- Energy as a function of time for
 - the impactor,
 - the target,
 - and the total energy (sum of both)
- Energy penetration depth
- Velocity orientation
- Porosity
- Energy area density

6.3.1 Description of analysis variables

6.3.1.1 Energy time series

Different variables are used to characterize how the impactor transfers its energy into the target ensemble. The most straightforward way to analyze the energy transfer is by looking at the behavior of the total kinetic energy of all the particles in the target, together with the impactor kinetic energy and the sum of both.

$$E_{\text{kin,tot}} = E_{\text{kin}}^{(\text{Impactor})} + \sum_i E_{\text{kin}}^{(\text{Target } i)} \quad (6.1)$$

An example plot of a time series like this is given in figure 6.6 which displays a representative behavior. In the beginning of the simulation, the target particles are at rest (zero kinetic energy) while the impactor holds the entire kinetic energy of the system. The energy is then transferred in discrete collision event, first from the impactor to a limited number of target particles, later also in collisions between different target particles. Through these collisions energy is transported away from the impact site to other parts of the target. These impact events are inelastic due to friction, resulting in a decrease of the sum kinetic energy in the system.

6.3.1.2 Energy depth histogram and penetration depth

The energy time series allows only a one dimensional analysis of a four dimensional problem. As a second dimension (besides time) the vertical distribution of energy shall be examined. This can be done with an energy depth histogram. In this scheme every

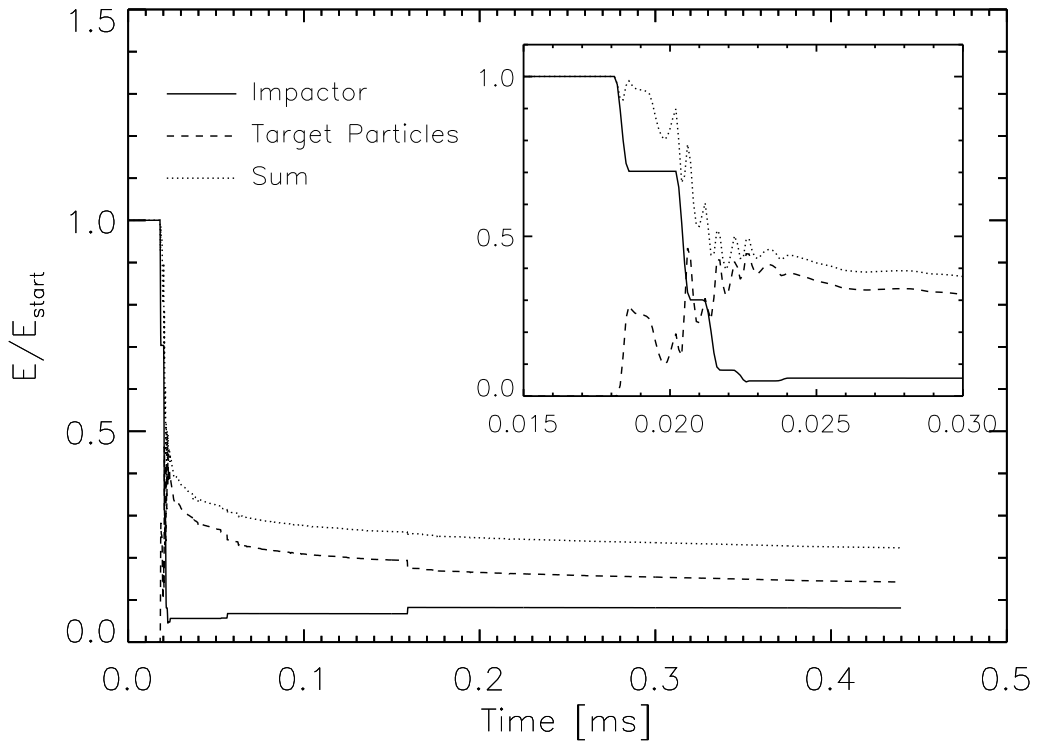


Figure 6.6: Exemplary time series of the energy of the impactor (black), the total kinetic energy in the target (red) and the sum of both (blue). Energy is transferred in discrete collision events, first only from the impactor to the target, later on also in collisions between target particles. Note the decrease of sum kinetic energy due to frictional losses in collisions.

particle with a given kinetic energy has a corresponding elevation above the ground level. The energy depth histogram plots the energy of particles below a given elevation.

$$E_{\text{kin}}(y) = \sum_{y_i < y} E_{y_i} \quad (6.2)$$

An exemplary histogram of the total kinetic energy of particles below a given height is plotted in figure 6.7.

The plot shows very little increase in energy content for particles in the bulk of the target. The major part of the kinetic energy is located in a shallow surface layer. The vertical extent of this surface layer dy_{50} (dy_{90}) can be characterized by a depth below the surface where particles above that depth hold 50% (90%) of the total kinetic energy in the target. Using the notation from equation 6.2 and the definition of y_{max} as the elevation of the surface of the target, one can describe this depth as follows.

$$E_{\text{kin}}(y_{\text{max}} - dy_{50}) = 0.5 \cdot E_{\text{kin,tot}} \quad (6.3)$$

$$E_{\text{kin}}(y_{\text{max}} - dy_{90}) = 0.1 \cdot E_{\text{kin,tot}} \quad (6.4)$$

This depth will vary over the course of the simulation as energy is being transported to particles embedded deeper within the target. The location of the penetration depth gives insight into how well the energy transfer works in the vertical direction.

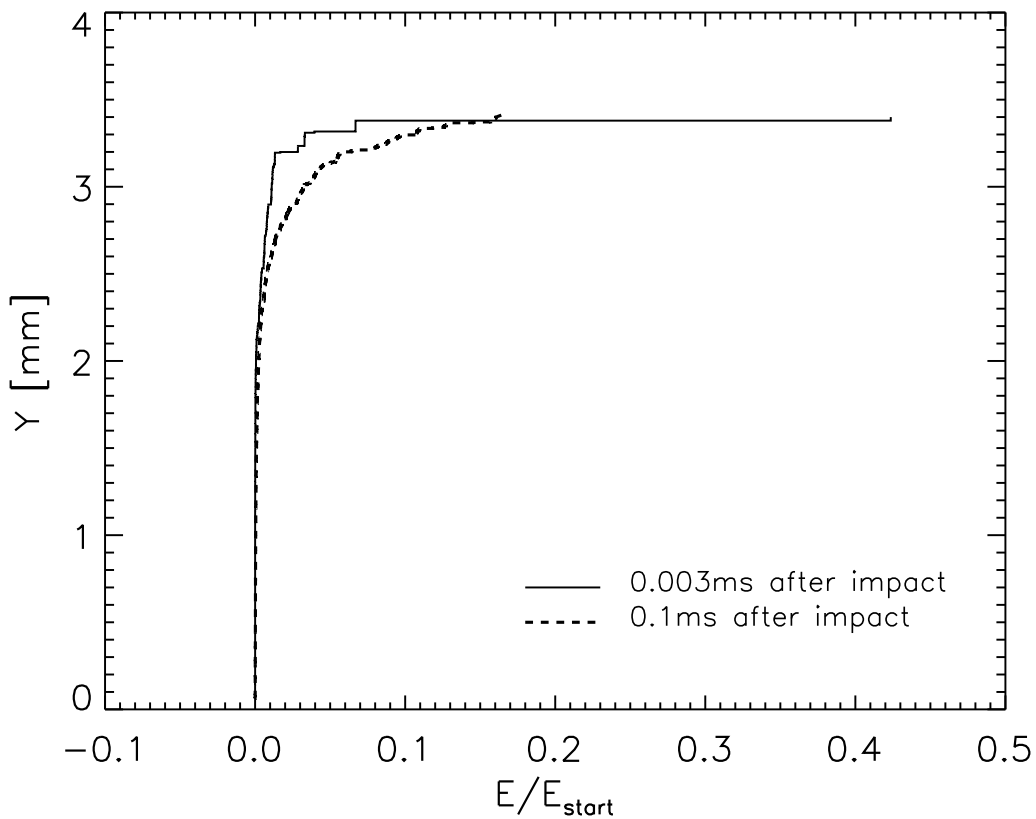


Figure 6.7: Exemplary energy-depth-histogram. The histogram has a very steep slope in the beginning indicating very little kinetic energy in the lower layers of the target. The shallow slope closer to the target surface corresponds to a fast increase of energy content for the particles close to the surface. Shortly after the impact the histogram has a step-like appearance because only a limited number of particles hold considerable amounts of kinetic energy leading to jumps in the histogram at the heights belonging to these particles. After some time the energy gets distributed among the target particles via collision leading to a smoother histogram.

6.3.1.3 Mean velocity vector

The behavior of the particles in this surface layer is of high interest. Considering how the energy is vertically confined to the surface the question arises how the energy spreads horizontally. One way to do that is to determine the direction of the mass weighted mean velocity of this surface layer (Eqn. 6.5).

$$\bar{\mathbf{v}} = \frac{\sum_i m_i \cdot \mathbf{v}_i}{\sum_i m_i} \quad (6.5)$$

An exemplary plot of the mean velocity over time is shown in figure 6.8. There the x- and z-components of the mean velocity vector for the surface layer are plotted for all analyzed time steps for a tilt angle of 30° and a vertical impact with normal and reduced gravity. The main difference between both lies in the fact, that for normal gravity the mean velocity is dictated by the downslope direction while for reduced gravity the particle

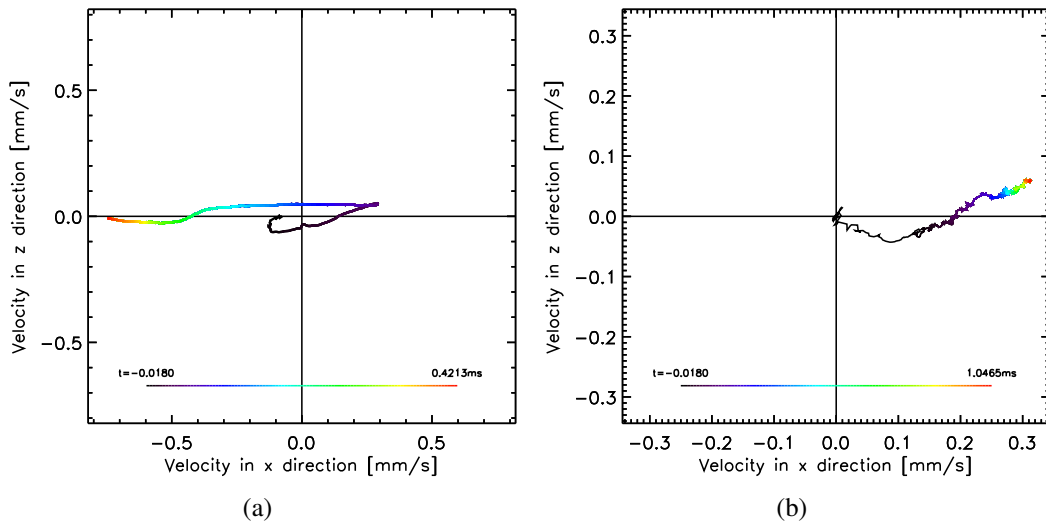


Figure 6.8: Exemplary mean velocity vector as a function of simulation time. The rainbow colored line traces the position of the the tip of the velocity vector (v_x, v_z). The change of color indicated the time after the start of the simulation. The mean velocity for simulations at 1 g (a) is mainly dictated by the slope (which is in negative x-direction). For reduced-g simulations (b) the particle geometry is the governing factor.

geometry plays a larger role.

6.3.1.4 Energy surface density

It is interesting to see how the energy is penetrating through the surface layer. Much like a drop of water that creates expanding circular waves on the surface of a pond, the energy, introduced into the system be the impactor, “expands” from the point of impact through the surface layer. Unlike in a liquid, in granular matter the energy inherent to the system is localized in the grains and can therefore be attributed a specific spatial coordinate.

For illustration purposes, the following considerations will focus on the top layer of the target defined by the energy penetration depth. In the following example the surface layer contains about 20,000 particles. The particles’ positions shall be projected onto the x-z-plane creating a map of their 2D position as is shown in figure 6.9. Note the voids that are created by the largest particles.

To make further calculations less computationally expensive the 2D positions of the particles are shifted onto a regular grid of dimensions 100×100 . This grid size was chosen because the division of the physical space into 100 equal parts creates a grid point distance that corresponds to the minimum particle size, i.e. the maximum positional error is less or equal to positional flexibility that any random particle has due to the grain size distribution, i.e. the minimum particle radius r_{\min} .

After moving the particles onto the grid, several grid points are now occupied by more than one particle. This poses no problem as each particle is still distinguishable by its unique ID.

So far the particle position is described by a point at the location of the spheres center. Since the particles are three dimensional object the energy they hold is not concentrated

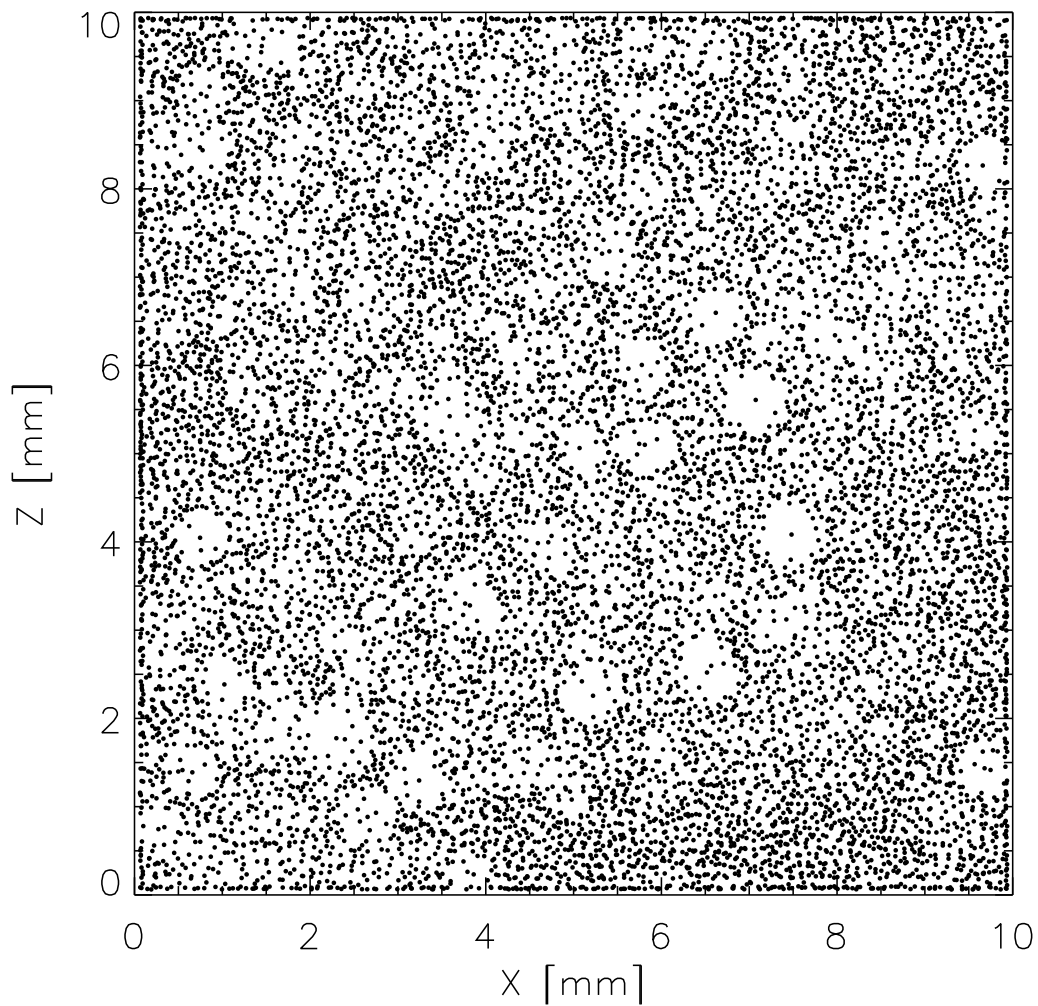


Figure 6.9: Positions of particle centers of an exemplary surface layer projected onto the x-z-plane. Every point represents one particle of this layer.

on a point at their center but rather spread out homogeneously over their volume, i.e. they have a fixed energy density.

Projecting the spheres onto a plane will create a circle. This circle, however, will not have a uniform energy surface density. The projection of the sphere will have a lower energy density at the rim and the highest density at the center. This is illustrated in figure 6.10.

This fact needs to be taken into account when creating the projected energy surface density. The grid points that, so far, represent the energy contained in the particles are therefore smeared out over the respective radial distance of the particle. For a particle with at grid position (x_g, z_g) with radius r and energy E this is done by creating an array $A_{i,j}$ of the same dimensions as the regular grid, that has the value E at A_{x_g, z_g} and zero everywhere else. This array is then convolved with a kernel of the same shape as seen in figure 6.10 that has a width of $2r$.

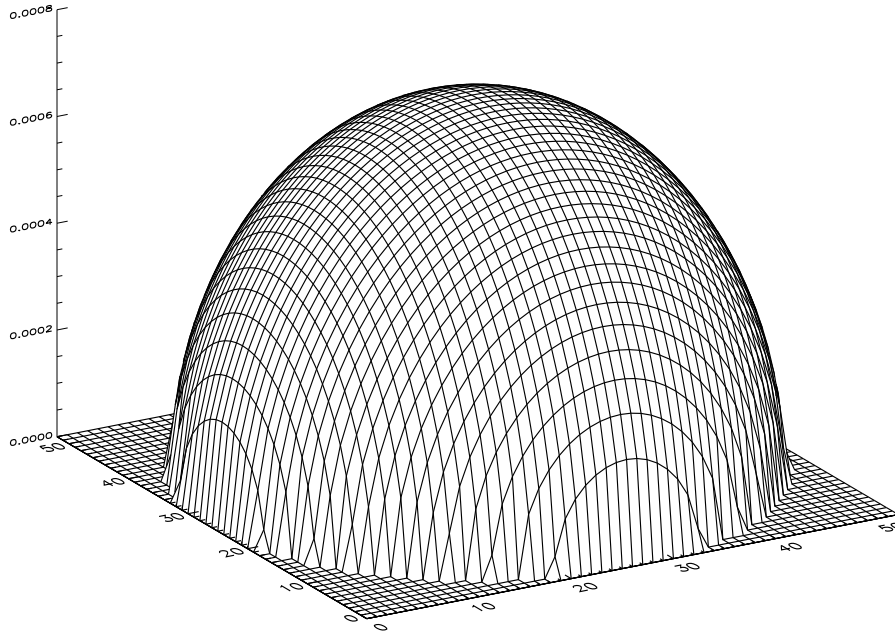


Figure 6.10: Projection of a sphere with a fixed energy density onto a plane. The energy distribution that was homogeneous in 3D is radially symmetric after the projection.

To decrease the computational demands, particles were not treated individually. Groups of particles within a given range of radii of width $dr = r_{\min}$ were all convolved with a kernel of the same width. The array $A_{i,j}$ is in this case created by adding all the energies E_i of particles with radius within said range

$$r_{\text{threshold}} < r_i < r_{\text{threshold}} + dr \quad (6.6)$$

at their respective positions x_i, z_i . If one grid position is occupied by more than one particle, the energies are summed up. This array is then convolved with a kernel of width $r_{\text{threshold}}$.

The error introduced by this is of the same order as the one created by the placement of the particles on the regular grid, as the error in radius is again of the order r_{\min} .

The convolved arrays for all ten radii ranges are then added on top of one another to create the final map of the energy area density, an example of which can be seen in figure 6.11.

6.3.1.5 Porosity

A possible consequence from an impact into granular material is that the material can dilate as described in Ch. 3.1.2. The dilation would result in an increase of porosity. This effect however is very small. The porosity will consequently change only negligibly.

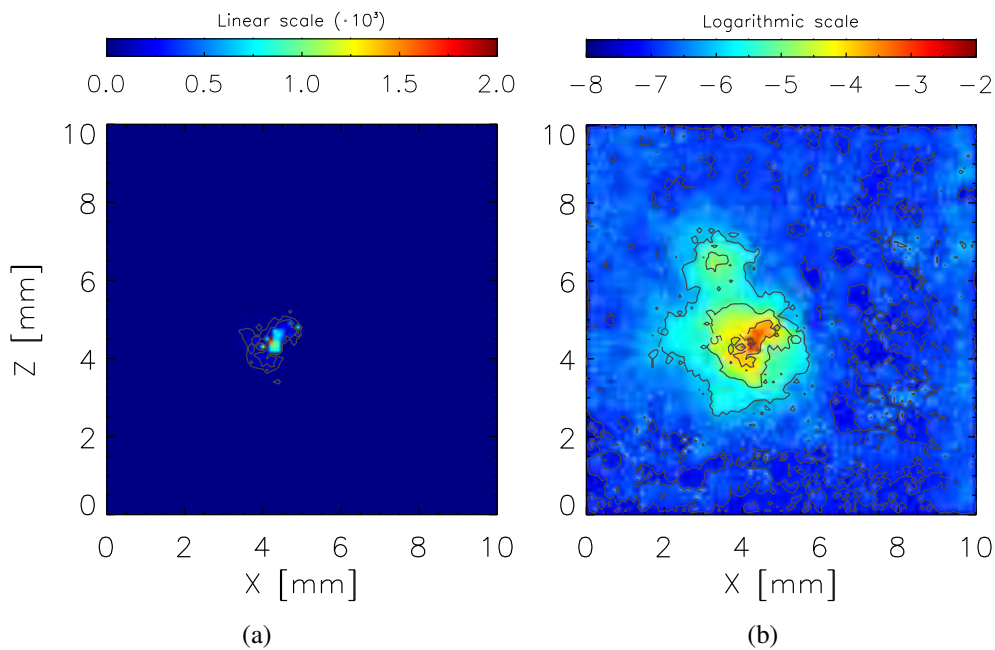


Figure 6.11: The resulting energy area density field. (a) on a linear scale and (b) on a logarithmic scale. This allows to see the more subtle variations, farther away from the impact site.

6.4 Results

To compare the results from the different simulations, different key quantities like the ones described in the previous section, are extracted from the data for a time step corresponding to $t = 8$ ms after the first contact between impactor and target. This time was chosen as a compromise. On the one hand it was important to let as much time pass between the impact and the time of evaluation while on the other hand the computations were very time consuming.

Plotted in figure 6.12 is the total energy in the target block 8 ms after the impact. The x-axis indicates the tilt angle of the box, the y-axis indicates the impactor's inclination to the surface normal. Plotted on the z-axis and traced also by the color scale is the energy.

The energies for the reduced gravity show a clear trend. The energy retained in the target block is higher for higher tilt angles and lower inclinations.

The energies in the 1 g case behave principally the same with one prominent exception: the perpendicular impact leads to substantially lower energies for higher tilt angles than the impacts that have 25° inclination. This may be caused by the way the energy is transmitted in the target block by force chains. When the impactors velocity vector has zero inclination to the surface normal the particles that get hit by the impactor will mostly start moving downward. This favors energy transport into the lower layers of the material where energy is more easily dissipated.

This fact can be easily illustrated. When two particles collide inelastically they lose energy due to frictional interaction during the contact. The more collisions a particle undergoes the faster it loses its energy. The number of collisions is mainly dominated by

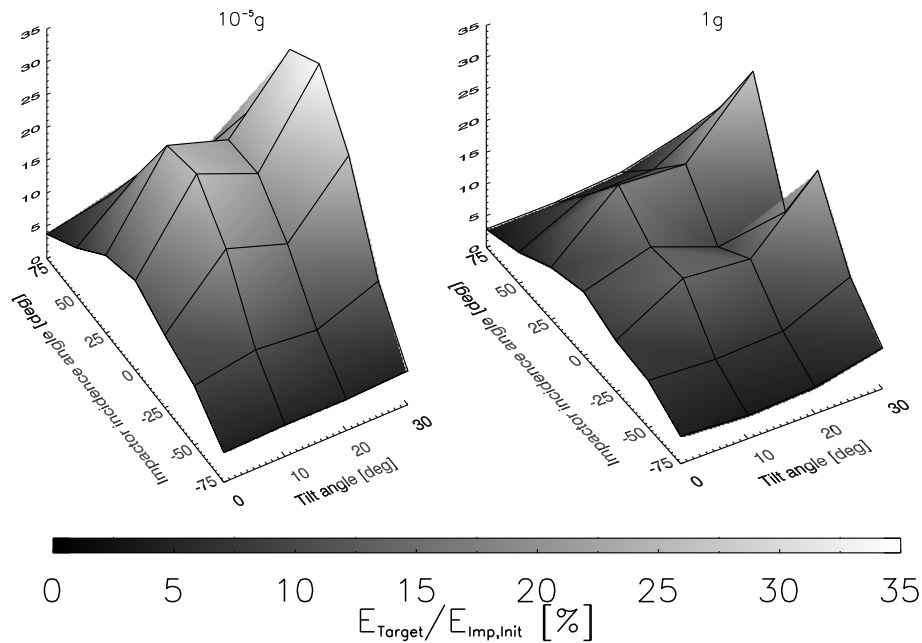


Figure 6.12: The energy in the target 8 ms after first contact for reduced (left) and normal (right) gravity as a function of tilt angle (x-axis) and impactor incidence angle (y-axis).

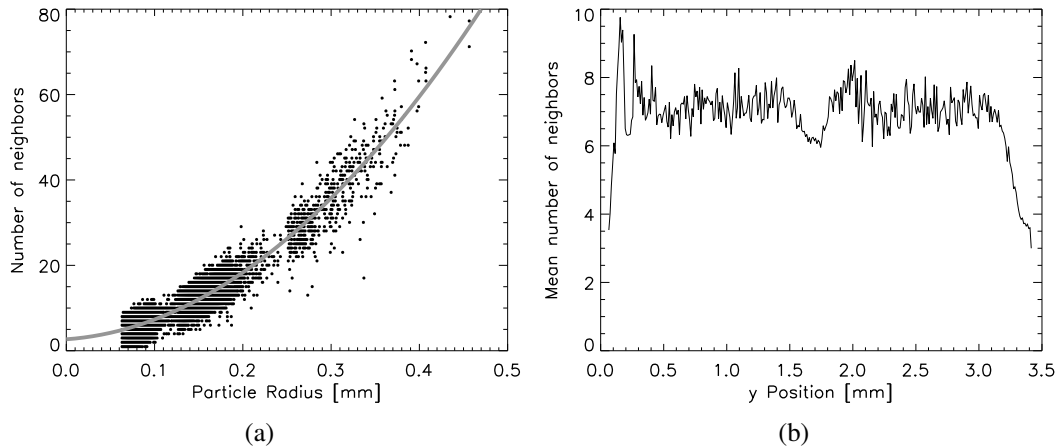


Figure 6.13: Number of neighbors in the target block as a function of (a) the particle radius and (b) the vertical position inside the target block. The gray line in (a) is a fitted parabola to the data points.

the number of collision partners available. This number of collision partners (or neighboring particles) is mainly a function of the size of the particle. This is illustrated in figure 6.13(a). The number of neighbors increases with the radius of the particle as r^2 because the surface of the sphere directly limits the number of particles in contact.

But the number of neighbors also varies with the vertical position within the target block (figure 6.13(b)). The mean number of neighbors decreases substantially close to

the surface and close to the bottom of the block because above the surface particles (and also below the bottom particles) is a half space that is void of any particles that could act as a collision partner.

A consequence of this is that energy is dissipated faster in lower layers of the block where collisions are more frequent because of the increased number of collision partners. Conversely the energy in the surface layers is more easily retained because the number of collision partners and therefore the number of collisions is lower.

During a vertical impact energy gets primarily transferred into the lower layers of the target where it is easily dissipated, reducing the total amount of energy in the target block.

This is not observed in the low gravity case because the lack of substantial downward acceleration leads to slow upward motion of the target block (a small jump). When the impactor hits the target particles the energy is transferred via force chains into the target. The particles first have a velocity vector that points downwards. The low lying particles are reflected from floor and travel upwards again (at an already drastically reduced speed) and collide again with particles above them. Since gravity is small, particles will slowly move upwards with a decreased number of inter-particle collisions. This is most effective in the vertical impact case.

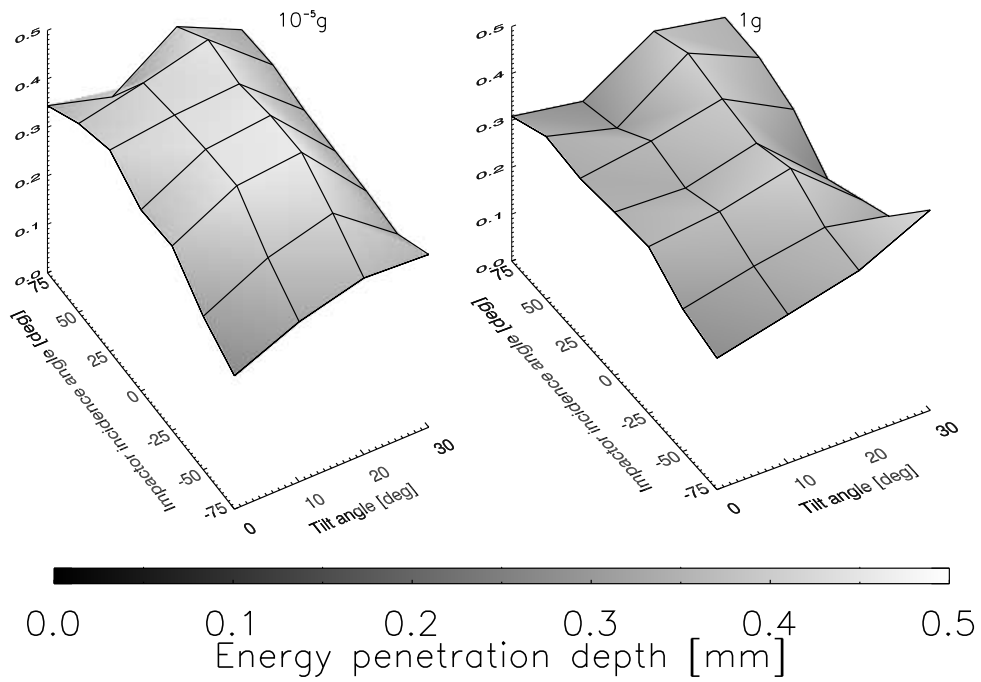
The 50% energy penetration depth (figure 6.14(a)) shows no clear trend for either angle but is generally close to the surface. It appears to be rather insensitive to gravity. Half of the energy is therefore retained in the surface layer regardless of the gravity level, the tilt angle of the material or the incidence angle of the impactor.

Similar findings hold true for the 90% energy penetration depth (figure 6.14(b)) in case of reduced gravity. For normal gravity, however, the 90% energy penetration depth is much more sensitive to both the tilt angle and the incidence angle. The data shows an increase in penetration depth for increasing tilt angle indicating a higher amount of energy in the lower layers of the target. Since this increase is not very drastic it can be assumed that it is caused by not perfectly settled material that now falls into place and builds up momentum in the process.

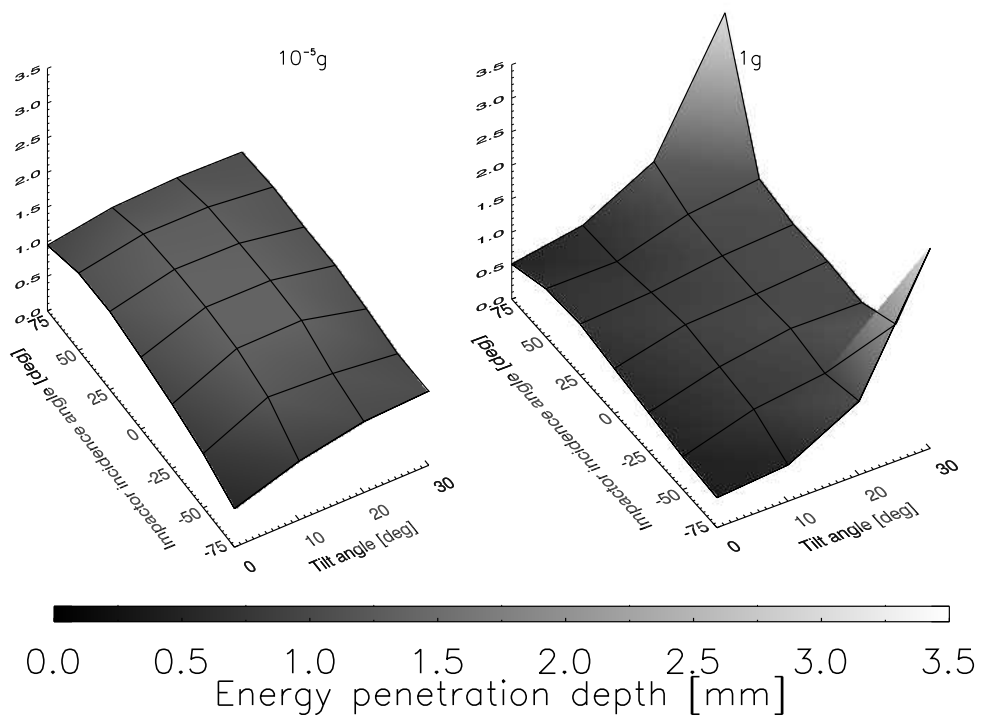
The steep increase in the 90% penetration depth for large incidence angles at 30° tilt is caused by the overall low energy levels in these simulations (see also figure 6.12). The impactor introduces only a very limited amount of energy into the system. Those particles that did not completely settle in the bulk of the target start falling into the potential energy wells and gain energy (because of the larger gravitational acceleration) that becomes comparable to the energy deposited by the impactor, thus increasing the energy penetration depth, at least for the 90% case.

The mean downhill velocity in the surface layer shows no dependence on either the tilt angle or the incidence angle for the low gravity simulations and is considerably lower than the corresponding 1 g velocities. This is shown in figure 6.15.

Since an avalanche is driven by gravity this is to be expected. Low gravity will take longer to accelerate agitated particles and thus trigger the avalanche (the impact creates velocity vectors that can point in any direction). The velocities in the simulations with normal gravity show the expected behavior that a steeper tilt angle will lead to higher downhill velocities.



(a)



(b)

Figure 6.14: The energy penetration depth ((a) 50%, (b) 90%) 8 ms after first contact for reduced (left) and normal (right) gravity as a function of tilt angle (x-axis) and impactor incidence angle (y-axis).

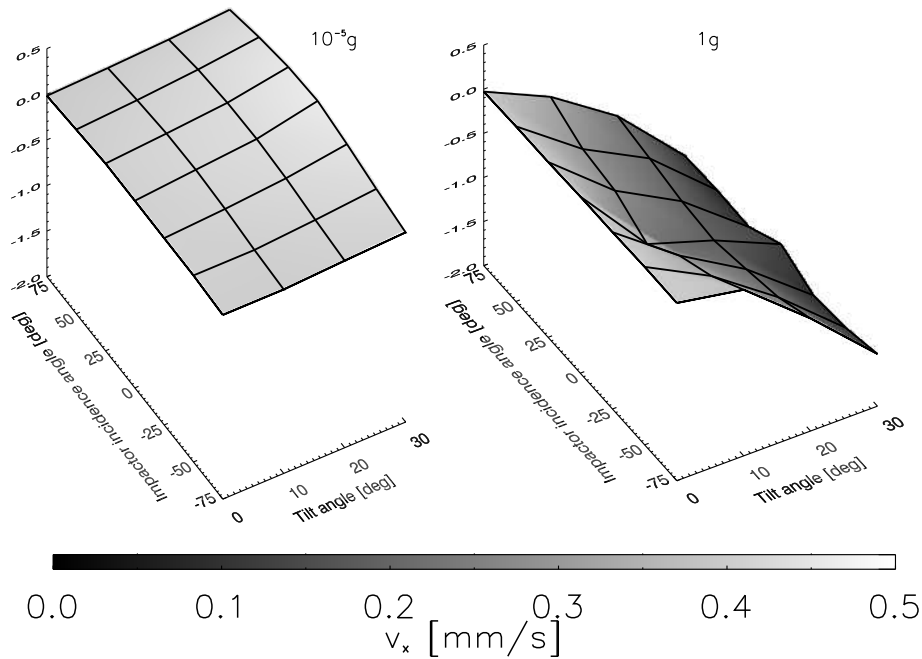


Figure 6.15: The mean downhill velocity in the surface layer 8 ms after first contact for reduced (left) and normal (right) gravity as a function of tilt angle (x-axis) and impactor incidence angle (y-axis).

It is possible to get an estimate of how fast the energy of the impactor gets spread in the surface layer by fitting an ellipse to the contour of a given energy level (figure 6.11(b)). This was done with the 10^{-4} contour in the logarithmic energy density plots yielding the results plotted in figure 6.16.

The semimajor axis appears to be independent of the gravity level. This implies that the spread of energy in the surface level is dominated by particle interaction. A slight trend towards higher semimajor axes for higher tilt angles is present, demonstrating at least a small influence of the global gravity on the energy distribution. But the main influencing factor is the incidence angle of the impactor. The highest semimajor axes, i.e. the widest spread of energy in the surface layer, are measured during vertical and almost vertical impacts. It is possible that the semimajor axis distribution would be uniform if, during the steeply inclined impacts, a larger amount of energy had been transferred into the target. The inefficient transfer would then naturally lead to smaller contours in the energy density plot.

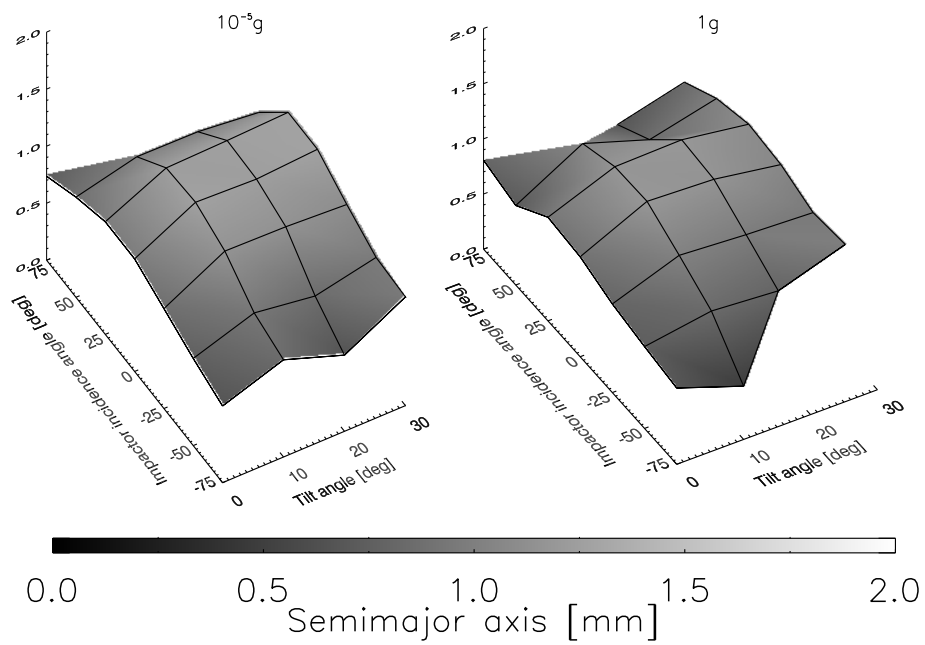


Figure 6.16: Comparison of the semimajor axis of the ellipse fit to the 10^{-4} energy contour 8 ms after first contact for reduced (left) and normal (right) gravity as a function of tilt angle (x-axis) and impactor incidence angle (y-axis).

7 Summary and conclusions

Asteroids are known to be covered with particulate material called regolith (chapter 2). Different processes are permanently at work that create or alter this regolith layer. Among these processes are landslides or avalanches that have been frequently observed (chapter 3). On the surface of (21) Lutetia, several prominent landslides have been identified (chapter 4). The question arises which processes could trigger such kind of avalanches in a low gravity, atmosphereless environment. One theoretically possible way is the impact of a millimeter sized body at several meters per second velocity.

This type of impact has been experimentally investigated in chapter 5. An extensive set of small scale impact experiments, both in vacuum and normal pressure as well as reduced gravity and normal gravity, has been conducted to determine how this process could influence asteroidal surfaces. Two different granular materials have been investigated:

- a ground HED meteorite that acts as a proxy for real asteroidal regolith
- and the JSC MARS-1 Martian soil simulant used as a proxy for regolith of larger bodies.

Their respective static angle of repose has been measured in a tumbler setup (table 5.2). For the MARS-1 different sievings have been used to analyze the influence of coarseness.

The main experiment investigated their response to the impact of a metal sphere of 2 and 3 mm diameter at velocities varying between ~ 0.5 and ~ 2 m/s for varying tilt angles of the material relative to the vector of gravity. High speed videos of the impact event have been analyzed with an image subtraction algorithm (chapter 5.3.4) to quantify the material's response.

Both materials showed avalanching as a result of the impacts at very high tilt angles (Figure 5.17) with the exception of the coarsest sieving of the MARS-1 sand.

One conclusion from this is, that the described type of impact can trigger an avalanche under laboratory conditions, if the mean particle diameter is notably smaller than the impactor.

A set of Monte Carlo simulations has been carried out to estimate a timescale over which this type of impact could alter a unit area of high enough tilt angle on the surface of an asteroid (chapter 5.4). Assuming that the avalanches observed are representative for avalanches on an asteroid, an impactor density of seven impacts per square meter has been calculated to be sufficient to cover the above mentioned unit area with avalanching material. Based on assumptions on the meteoroid flux in the main belt (which is used to estimate the number of secondary impacts of appropriate type), a time of 1.6 Myr can be estimated to reach that kind of impactor density.

As a second approach to the question, a suite of simulations with the DEM software package *ESyS-Particle* has been carried out (chapter 6). This was done to understand the microphysical processes at work during a small scale slow impact. Different configurations, varying the tilt angle of the target material as well as the angle between the impactors velocity vector and the normal to the target surface, were simulated.

The setup of the simulations (chapter 6.2) was designed in a way that it could be compared to the impact experiments done with the MARS-1 material. Due to computational restraints the size of the simulation as well as the simulated timespan had to be reduced to a $10 \times 10 \text{ mm}^2$ box during the first few milliseconds after the impact.

The output of the simulations was used to synthesize certain key variables of the granular system (chapter 6.3.1). These variables were evaluated with respect to energy transport and dissipation in the target and enhancement of movement near the surface.

The simulations show (chapter 6.4) that, as expected, gravity is the main driver of an avalanche. Key variables like downhill velocity in the sliding surface layer and energy content in the target strongly depend on gravity as well as the tilt angle.

Energy dissipation works through inelastic collision which occur more frequently in the bulk of the target, leading to a faster loss of energy there than near the surface.

Energy transfer in the surface layer appears to be independent of the variables of the simulations but seems to be governed by particle arrangement.

8 Outlook

Although a lot of effort has been put into this work, there is still room for improvement.

The experiment described in chapter 5 was not running at peak efficiency. An additional campaign at the Drop Tower or even during a parabolic flight is highly desirable to improve upon the findings.

Investigating a broader palette of materials in the experiment would most likely further our understanding of the observed effects, especially the change in avalanching rate with coarseness of the material. Using mono-disperse spheres of different size and composition would make a good addition to the dataset already taken. The use of non-spherical grains of quantifiable shape should allow to broaden the dataset in terms of the influence of shape on the avalanching behavior. A new campaign would also allow to investigate a broader range of tilt angles.

In addition, an improvement on the experimental setup itself can be deployed. A new cannon can be designed that allows for a wider range of impact velocities while reducing the magnitude of mechanical waves in the setup.

The simulations can be expanded in size in order to reduce the possible effect of boundary conditions on the outcome. The performance of the used software and hardware needs to be sorted out in order to create a simulation environment that is as close as possible to the real conditions of the experiment. The use of other software packages can be included if deemed useful.

The use of the iSALE simulation code that utilizes hydrodynamics to describe the behavior of granular matter could, because of time constraints, not be performed in the course of this PhD project. Expanding the simulation volume to larger proportions is readily done with this software and should definitely be pursued in order to link the experimental and numerical investigation of the early phases of a landslide to its later development.

A Appendix - Experiments on Avalanche Triggering

A.1 Details on experimental campaigns

Table A.1: Details on the *HB*-Campaign (HED).

Drop Number	p_{Tower} [Pa]	ω [rpm]	α [deg]	v_{Imp} [m/s]	Noise [grey value]
1	16.0	38	54.6	0.000	6
2	18.0	38	61.6	0.000	6
3	16.0	38	36.1	1.279	6
4	18.0	38	34.9	0.000	6
5	17.9	38	33.9	0.000	7
6	19.0	38	34.1	0.933	7
7	19.5	38	34.8	1.487	7
8	16.6	48	34.0	0.000	7
9	15.1	27	34.1	1.458	7
10	15.5	48	34.5	1.509	7

The impactor diameter is 2 mm, the frame rate is 2000 FPS, the voltage on the cannon is 24 V. The variation of the impact speed is due to mechanical problems of the setup. 0 m/s impactor speed indicates that the bullet missed (see Ch. 5.3.6 for details).

Table A.2: Details on the *HB*-Campaign (MARS-1).

Drop Number	p_{Tower} [Pa]	ω [rpm]	α [deg]	v_{Imp} [m/s]	Noise [grey value]
1	16.0	38	39.9	1.124	6
2	18.0	38	59.9	0.000	6
3	16.0	38	23.9	2.150	6
4	18.0	38	22.0	1.385	6
5	17.9	38	22.7	1.570	6
6	19.0	38	22.5	1.552	6
7	19.5	38	22.5	1.554	6
8	16.6	48	23.8	1.557	6
9	15.1	27	25.4	1.474	6
10	15.5	48	24.1	1.592	6

Impactor diameter is 2 mm, frame rate is 2000 FPS, voltage on the cannon is 24 V. The variation of the impact speed is due to mechanical problems of the setup. 0 m/s impactor speed indicates that the bullet missed (see Ch. 5.3.6 for details).

Table A.3: Details on the *BS-I*-Campaign.

Number	Material	p [mbar]	α [deg]	U_B [V]	Noise [grey value]
1	HED	8	19.21	18	3
2	HED	20	22.40	18	3
3	HED	28	22.22	18	3
4	HED	40	27.42	18	3
5	HED	4	27.27	18	3
6	HED	3	28.53	18	3
7	HED	20	25.60	18	3
8	HED	9	34.33	18	3
9	HED	10	44.32	18	3
10	HED	8	48.50	18	3
11	HED	3	33.55	18	3
12	MARS-1	9	16.42	18	3
13	MARS-1	5	22.53	18	3
14	MARS-1	25	30.92	18	3
15	MARS-1	11	34.34	18	2
16	MARS-1	3	33.13	24	2
17	HED	3	33.54	24	3
18	HED	5	40.71	24	3
19	HED	2	41.72	24	3
20	HED	1000	20.46	24	3
21	HED	1000	19.25	18	3
22	HED	1000	26.20	24	3
23	HED	1000	29.87	24	3
24	HED	1000	34.60	24	3
25	HED	1000	38.82	24	3
26	HED	1000	43.10	24	3
27	HED	1000	44.87	24	3
28	HED	1000	42.66	18	3
29	HED	1000	42.99	12	3
30	MARS-1	1000	19.02	24	3
31	MARS-1	1000	22.83	24	3
32	MARS-1	1000	29.02	24	3
33	MARS-1	1000	34.29	24	3
34	MARS-1	1000	39.33	24	3
35	MARS-1	1000	42.39	24	3
36	MARS-1	1000	37.79	12	3

All MARS-1 measurements were conducted with the sieving 250 – 1000 μm . The impactor diameter is 2 mm and the frame rate is 2000 FPS.

Table A.4: Details on the *BS-2*-Campaign.

Number	U_{textrmB} [V]
1	12.19
2	10.04
3	10.04
4	10.04
5	12.19
6	12.19
7	14.05
8	14.05
9	14.05
10	16.02
11	16.02
12	16.02
13	17.99
14	17.99
15	17.99
16	17.99
17	20.05
18	20.05
19	20.05
20	22.02
21	22.02
22	22.02
23	23.99
24	23.99
25	23.99

The frame rate is 2000 FPS.

Table A.5: Details on the *BS-3*-Campaign.

Number	α [deg]	U_B [V]	Noise [grey value]
1	4.71	12	2
2	4.75	18	2
3	4.78	24	2
4	18.78	12	2
5	18.86	18	2
6	18.82	24	2
7	25.59	12	2
8	25.55	18	2
9	25.44	24	2
10	30.25	12	2
11	30.29	18	2
12	30.04	18	2
13	29.95	12	2
14	30.03	24	2
15	30.98	24	2
16	35.29	12	2
17	35.67	12	2
18	35.16	12	2
19	35.83	18	2
20	36.80	18	2
21	37.00	24	2
22	35.69	24	2
23	39.76	12	2
24	40.61	12	2
25	40.25	18	2
26	39.60	18	2
27	40.04	24	2
28	40.02	24	2

The frame rate is 3000 FPS.

Table A.6: Details on the *BS-4*-Campaign.

Number	α [deg]	U_B [V]	Noise [grey value]	Frame rate [FPS]
1	0.00	12	2	5000
2	0.00	12	2	5000
3	0.00	12	2	5000
4	0.00	12	2	5000
5	0.00	18	2	5000
6	0.00	18	2	5000
7	0.00	24	2	5000
8	0.00	24	2	5000
9	18.77	12	2	5000
10	19.61	12	3	5000
11	19.44	18	3	5000
12	19.82	18	3	5000
13	20.28	18	3	5000
14	19.44	24	3	5000
15	19.60	24	3	5000
16	23.70	12	3	5000
17	24.19	12	3	5000
18	24.12	18	3	5000
19	23.85	18	3	5000
20	24.50	24	3	5000
21	24.18	24	3	5000
22	29.12	12	3	5000
23	28.60	12	3	5000
24	28.79	18	3	5000
25	28.67	18	3	5000
26	28.71	24	3	5000
27	28.34	24	3	5000
28	34.49	12	3	5000
29	33.17	12	3	5000
30	34.09	18	3	5000
31	34.86	18	3	5000
32	35.28	24	3	5000
33	34.77	24	3	5000
34	39.96	12	3	5000
35	39.43	12	3	5000
36	40.24	12	3	5000
37	40.36	18	3	5000
38	40.26	18	3	5000
39	40.43	24	3	4000
40	40.12	24	3	4000

Table A.7: Continued: Details on the *BS-4*-Campaign.

Number	α [deg]	U_B [V]	Noise [grey value]	Frame rate [FPS]
41	43.89	12	3	4000
42	43.21	12	3	4000
43	43.20	18	3	4000
44	43.64	18	3	4000
45	42.50	24	3	4000
46	44.58	24	3	4000

Table A.8: Details on the *BS-5*-Campaign.

Number	α [deg]	v_{Imp} [m/s]	Noise [grey value]	Impactor \varnothing [mm]	Frame rate [FPS]
1	18.75	0.988	3	2	4000
2	18.62	0.967	3	2	4000
3	18.52	1.464	3	2	4000
4	18.77	1.192	3	2	4000
5	18.68	1.960	3	2	4000
6	18.73	1.914	3	2	4000
7	24.11	0.561	3	2	4000
8	24.10	0.573	3	2	4000
9	24.12	0.973	3	2	4000
10	24.07	0.934	3	2	4000
11	24.06	1.402	3	2	4000
12	24.09	1.380	3	2	4000
13	24.03	1.822	3	2	4000
14	24.04	1.730	3	2	4000
15	30.17	0.516	3	2	4000
16	30.38	0.539	3	2	4000
17	30.17	0.961	3	2	4000
18	30.29	1.658	2	2	5000
19	30.22	1.181	2	2	5000
20	30.21	1.706	2	2	5000
21	30.29	2.249	2	2	5000
22	30.30	2.109	2	2	5000
23	30.31	0.697	2	3	5000
24	30.32	0.723	2	3	5000
25	30.27	0.641	2	3	5000
26	30.27	0.986	2	3	5000
27	30.27	1.724	2	3	5000
28	30.27	1.348	2	3	5000
29	30.27	1.439	2	3	5000
30	30.27	1.862	2	3	5000

Table A.9: Continued: Details on the *BS-5*-Campaign.

Number	α [deg]	v_{imp} [m/s]	Noise [grey value]	Impactor \varnothing [mm]	Frame rate [FPS]
31	30.27	0.837	2	3	5000
32	35.45	0.589	2	2	5000
33	35.52	0.681	2	2	5000
34	35.54	1.187	2	2	5000
35	35.50	0.567	2	2	5000
36	35.50	1.789	2	2	5000
37	35.50	1.477	3	2	2000
38	35.50	1.639	3	2	2000
39	35.50	1.847	3	2	2000
40	35.50	0.690	3	3	2000
41	35.50	0.695	3	3	2000
42	35.50	0.971	3	3	2000
43	35.50	0.965	3	3	2000
44	35.50	1.495	3	3	2000
45	35.50	1.408	3	3	2000
46	35.50	1.632	3	3	2000
47	35.50	1.608	3	3	2000
48	41.60	0.698	3	3	2000
49	41.57	0.491	3	3	2000
50	41.67	0.439	3	3	2000
51	41.62	1.014	3	3	2000
52	41.62	0.479	3	3	2000
53	41.62	1.450	3	3	2000
54	41.62	1.976	3	3	2000
55	41.62	1.907	3	3	2000
56	41.62	0.582	3	2	2000
57	41.62	0.614	3	2	2000
58	41.62	1.041	3	2	2000
59	41.62	1.042	3	2	2000
60	41.62	1.417	3	2	2000
61	41.62	1.410	3	2	2000
62	41.62	1.293	3	2	2000
63	42.82	0.471	3	2	2000

Table A.10: Details on the *BS-6*-Campaign.

Number	α [deg]	v_{imp} [m/s]	Noise [grey value]	Impactor \varnothing [mm]
1	20.79	0.414	3	2
2	20.77	0.458	3	2
3	20.89	0.937	3	2
4	20.81	0.898	3	2
5	20.81	1.355	3	2
6	20.81	1.356	3	2
7	20.81	1.121	3	2
8	20.81	1.789	3	2
9	20.81	0.510	3	3
10	20.81	0.469	3	3
11	20.81	0.903	3	3
12	20.81	0.491	3	3
13	20.81	1.367	3	3
14	20.81	0.558	3	3
15	20.81	1.794	3	3
16	20.81	1.537	3	3
17	26.11	0.525	2	2
18	26.12	0.499	2	2
19	26.03	0.833	2	2
20	26.08	0.881	2	2
21	26.08	1.248	2	3
22	26.08	1.267	2	3
23	26.08	1.609	2	3
24	26.08	1.623	2	3
25	26.08	0.458	2	2
26	26.08	0.466	2	2
27	26.08	0.451	2	2
28	26.08	0.450	2	2
29	26.08	1.177	2	2
30	26.08	1.260	2	2
31	26.08	1.662	3	2
32	26.08	1.560	3	2
33	30.43	0.514	3	3
34	30.33	0.544	3	3
35	30.37	0.759	3	3
36	30.38	0.532	3	3
37	30.38	1.268	3	3
38	30.38	0.895	3	3
39	30.38	1.265	3	3
40	30.38	1.530	3	3

The frame rate is 2000 FPS.

Table A.11: Continued: Details on the *BS-6*-Campaign.

Number	α [deg]	v_{imp} [m/s]	Noise [grey value]	Impactor \varnothing [mm]
41	30.38	1.730	3	2
42	30.38	0.579	3	2
43	30.38	0.557	3	2
44	30.38	0.904	3	2
45	30.38	0.890	3	2
46	30.38	1.255	3	2
47	30.38	1.282	3	2
48	30.38	0.640	3	2
49	30.38	1.601	3	3
50	37.81	0.598	3	3
51	37.86	0.580	3	3
52	37.72	0.474	3	3
53	37.80	0.977	3	3
54	37.80	1.351	3	3
55	37.80	1.265	3	3
56	37.80	0.611	3	3
57	37.80	1.645	3	2
58	37.80	0.662	3	2
59	37.80	0.640	3	2
60	37.80	0.421	3	2
61	37.80	0.997	3	2
62	37.80	1.462	3	2
63	37.80	1.333	3	2
64	37.80	1.793	3	2
65	37.80	1.686	3	3
66	42.17	0.599	3	3
67	42.39	1.041	3	3
68	42.32	1.182	3	3
69	41.62	1.866	3	3
70	40.54	0.689	3	3
71	40.72	0.905	3	3
72	40.62	0.924	3	3
73	40.56	1.705	3	3

The frame rate is 2000 FPS.

Table A.12: Details on the *BS-7-Campaign*.

Number	α [deg]	v_{imp} [m/s]	Noise [grey value]	Impactor \varnothing [mm]
1	36.69	0.641	3	2
2	36.55	0.630	3	2
3	36.45	0.646	3	2
4	36.37	0.996	3	2
5	36.51	1.359	3	2
6	36.51	0.622	3	2
7	36.51	1.822	3	2
8	36.51	1.796	3	2
9	36.51	0.563	3	3
10	36.51	0.593	3	3
11	36.51	0.969	3	3
12	36.51	0.917	3	3
13	36.51	1.293	3	3
14	36.51	0.485	3	3
15	36.51	1.743	3	3
16	36.51	0.940	3	3
17	41.57	0.636	2	2
18	43.11	1.027	2	2
19	43.10	0.641	2	2
20	41.09	1.750	2	2
21	43.12	0.566	2	3
22	43.12	0.991	2	3
23	43.12	1.319	2	3
24	43.12	1.725	2	3
25	21.73	0.583	2	2
26	21.60	0.573	2	2
27	21.43	0.990	2	2
28	21.52	0.508	2	2
29	21.57	1.468	2	2
30	21.57	1.461	2	2
31	21.57	1.871	3	2
32	21.57	1.708	3	2
33	21.57	0.605	3	3
34	21.57	0.536	3	3
35	21.57	0.566	3	3
36	21.57	0.972	3	3
37	21.57	0.527	3	3
38	21.57	1.368	3	3
39	21.57	1.783	3	3
40	21.57	1.019	3	3

The frame rate is 2000 FPS.

Table A.13: Continued: Details on the *BS-7*-Campaign.

Number	α [deg]	v_{imp} [m/s]	Noise [grey value]	Impactor \varnothing [mm]
41	26.14	0.461	3	2
42	26.19	0.571	3	2
43	26.13	0.894	3	2
44	26.18	0.454	3	2
45	26.16	1.133	3	2
46	26.16	1.371	3	2
47	26.16	1.590	3	2
48	26.16	1.599	3	2
49	26.16	0.586	3	3
50	26.16	0.571	3	3
51	26.16	0.910	3	3
52	26.16	0.957	3	3
53	26.16	1.181	3	3
54	26.16	0.323	3	3
55	26.16	1.697	3	3
56	26.16	1.563	3	3
57	30.54	0.625	3	2
58	30.71	0.593	3	2
59	30.58	0.284	3	2
60	30.52	0.941	3	2
61	30.59	1.373	3	2
62	30.59	1.331	3	2
63	30.59	1.752	3	2
64	30.59	1.706	3	2
65	30.59	0.583	3	3
66	30.59	0.622	3	3
67	30.59	0.982	3	3
68	30.59	0.998	3	3
69	30.59	1.460	3	3
70	30.59	1.434	3	3
71	30.59	0.651	3	3
72	30.59	0.917	3	3

The frame rate is 2000 FPS.

Table A.14: Details on the *BS-8-Campaign*.

Number	α [deg]	v_{imp} [m/s]	Noise [grey value]	Impactor \varnothing [mm]
1	30.72	1.088	3	3
2	30.88	1.498	3	3
3	31.03	1.870	3	3
4	30.87	1.013	3	2
5	31.00	1.275	3	2
6	30.98	1.966	3	2
7	36.60	1.053	3	3
8	36.83	1.460	3	3
9	36.50	1.853	3	3
10	36.87	0.966	3	2
11	36.67	1.444	3	2
12	36.57	1.120	3	2
13	39.83	1.042	3	3
14	39.89	1.441	3	3
15	39.70	1.917	3	3
16	40.11	1.040	3	2
17	40.01	1.279	3	2
18	40.04	1.813	3	2
19	46.36	0.983	3	3
20	46.14	1.433	3	3
21	46.52	1.841	3	3
22	46.28	0.962	3	2
23	46.37	1.417	3	2
24	46.22	1.877	3	2
25	19.58	0.944	3	3
26	20.04	1.377	3	3
27	20.15	1.497	3	3
28	19.94	0.943	3	2
29	19.84	1.357	3	2
30	19.79	1.829	3	2
31	25.03	0.984	3	3
32	25.05	1.414	3	3
33	25.09	0.960	3	3
34	25.15	0.963	3	2
35	25.41	1.420	3	2
36	25.11	1.746	3	2
37	35.63	0.471	3	3
38	35.37	0.680	3	3
39	35.37	1.936	3	3
40	35.36	0.957	3	2

The frame rate is 2000 FPS.

Table A.15: Continued: Details on the *BS-8*-Campaign.

Number	α [deg]	v_{imp} [m/s]	Noise [grey value]	Impactor \varnothing [mm]
41	35.50	1.473	3	2
42	35.62	1.850	3	2
43	40.56	0.787	3	3
44	40.85	1.465	3	3
45	40.57	0.812	3	3
46	40.50	0.978	3	2
47	40.89	1.431	3	2
48	40.53	1.838	3	2

The frame rate is 2000 FPS.

A.2 The smoothing algorithm

Figure A.1(a) displays a difference image cropped to the mirror view (*BS-3*, No. 27). Figure A.1(b) shows the same frame in a 3D plot. Moving pixels are at the bottom of the plot (0), pixels at rest at the top (255). To get a better estimate on the real area that is covered by moving material a smoothing is applied to the image, yielding figure A.1(c).

The sharp spikes are washed out, resulting in a inverse mountain like shape. By setting a threshold for the gray scale value below which a motion is assumed (in the case of figure A.1(d) a level of 20 gray values below 255 was used) one can get a better estimate of the true area of motion. Figure A.1(e) gives the view from the top and figure A.1(f) shows the corresponding frame from the tiff stack produced by the image subtraction algorithm. The moving pixels are shown in black, the area of motion is given in gray, non-moving pixels are white. Pixels not enveloped by the gray area are assumed to be single grains in motion not contributing to the main body of motion.

A similar approach was attempted for the direct view to get an estimate of the height of the moving layer. This was unsuccessful as the motion is mostly confined to the center of the box and therefore not fully visible in its vertical extent from the side. Hence only the surface area visible in the mirror can be given later to characterize the size of an avalanche.

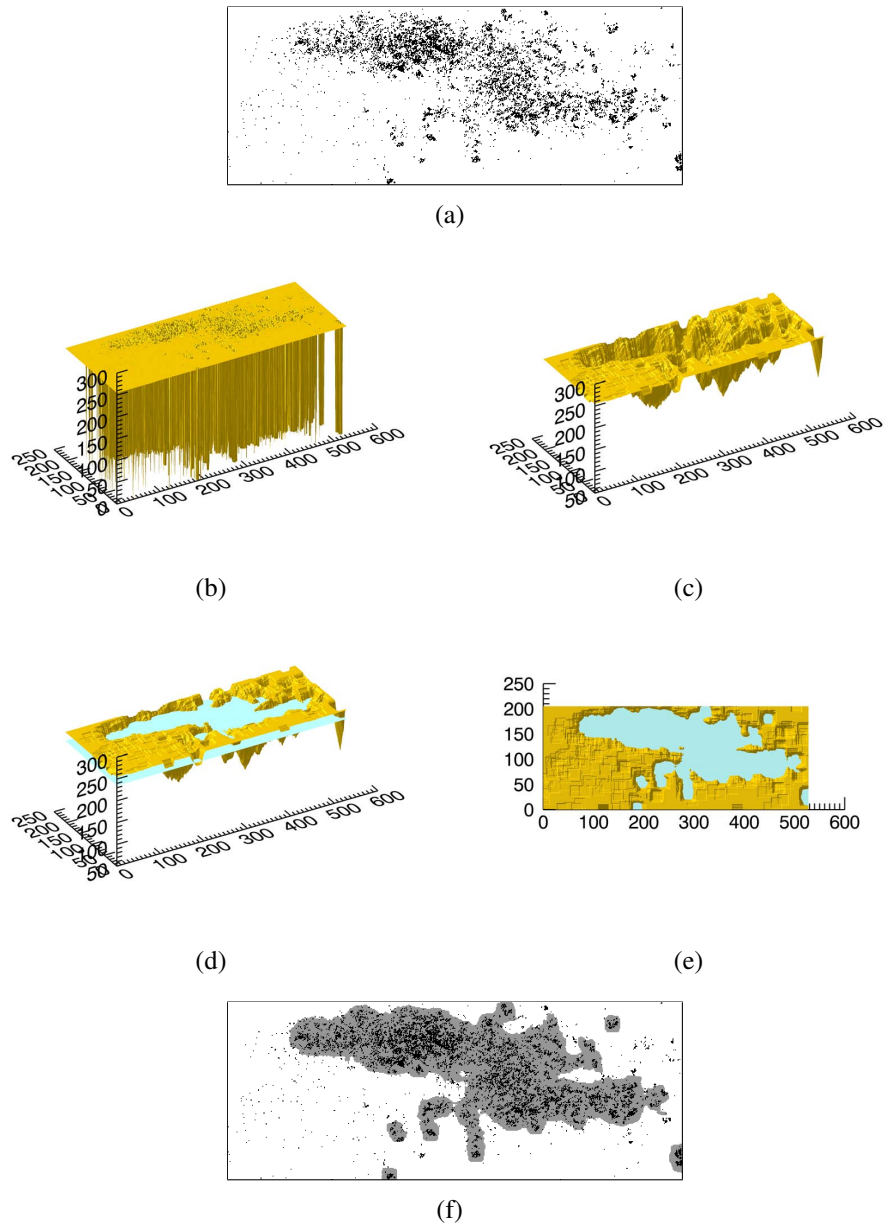


Figure A.1: (a) Noise cleaned difference image between *BS-3*, No. 27, Im. 12250 and Im. 12255. (b) A three-dimensional view of the same difference image. (c) A three-dimensional view of the same difference image after smoothing has been applied. (d) Same as (c), the blue plane shows the threshold for signal detection. (e) Top view of the smoothing image with detection threshold. (f) Resulting two-dimensional frame, similar to A.1(a) but the gray area shows the newly calculated moving pixels.

Bibliography

- A'Hearn, M. F., Belton, M. J. S., Delamere, W. A., Kissel, J., Klaasen, K. P., McFadden, L. A., Meech, K. J., Melosh, H. J., Schultz, P. H., Sunshine, J. M., Thomas, P. C., Veverka, J., Yeomans, D. K., Baca, M. W., Busko, I., Crockett, C. J., Collins, S. M., Desnoyer, M., Eberhardy, C. A., Ernst, C. M., Farnham, T. L., Feaga, L., Groussin, O., Hampton, D., Ipatov, S. I., Li, J.-Y., Lindler, D., Lisse, C. M., Mastrodemos, N., Owen, W. M., Richardson, J. E., Wellnitz, D. D., and White, R. L. (2005). Deep Impact: Excavating Comet Tempel 1. *Science*, **310**, 258–264.
- A'Hearn, M. F., Belton, M. J. S., Delamere, W. A., Feaga, L. M., Hampton, D., Kissel, J., Klaasen, K. P., McFadden, L. A., Meech, K. J., Melosh, H. J., Schultz, P. H., Sunshine, J. M., Thomas, P. C., Veverka, J., Wellnitz, D. D., Yeomans, D. K., Besse, S., Bodewits, D., Bowling, T. J., Carcich, B. T., Collins, S. M., Farnham, T. L., Groussin, O., Hermany, B., Kelley, M. S., Kelley, M. S., Li, J.-Y., Lindler, D. J., Lisse, C. M., McLaughlin, S. A., Merlin, F., Protopapa, S., Richardson, J. E., and Williams, J. L. (2011). EPOXI at Comet Hartley 2. *Science*, **332**, 1396–1400.
- Armitage, P. J. (2010). *Astrophysics of Planet Formation*. Cambridge University Press.
- Bagnold, R. A. (1954). Experiments on a Gravity-Free Dispersion of Large Solid Spheres in a Newtonian Fluid under Shear. *Royal Society of London Proceedings Series A*, **225**, 49–63.
- Bagnold, R. A. (1966). The Shearing and Dilatation of Dry Sand and the 'Singing' Mechanism. *Royal Society of London Proceedings Series A*, **295**, 219–232.
- Barucci, M.-A. and Fulchignoni, M. (2007). *Pre-Fly-by Properties of the Rosetta Asteroids Targets 2867 Steins and 21 Lutetia*, volume 128, chapter 3, pages 55–68. Springer-Verlag.
- Belton, M. J. S., Chapman, C. R., Klaasen, K. P., Harch, A. P., Thomas, P. C., Veverka, J., McEwen, A. S., and Pappalardo, R. T. (1996). Galileo's Encounter with 243 Ida: An Overview of the Imaging Experiment. *Icarus*, **120**, 1–19.
- Bhattacharya, S. K., Goswami, J. N., Lal, D., Patel, P. P., and Rao, M. N. (1975). Lunar regolith and gas-rich meteorites - Characterization based on particle tracks and grain-size distributions. In *Lunar and Planetary Science Conference Proceedings*, volume 6 of *Lunar and Planetary Science Conference Proceedings*, pages 3509–3526.
- Binzel, R. P. and Xu, S. (1993). Chips off of asteroid 4 Vesta - Evidence for the parent body of basaltic achondrite meteorites. *Science*, **260**, 186–191.

- Blum, J. (2010). Astrophysical Microgravity Experiments with Dust Particles. *Microgravity Science and Technology*, **22**, 517–527.
- Bonnet, R. M. (1985). The new mandatory scientific programme for ESA. *ESA Bulletin*, **43**, 8–13.
- Börzsönyi, T., Halsey, T. C., and Ecke, R. E. (2005). Two Scenarios for Avalanche Dynamics in Inclined Granular Layers. *Physical Review Letters*, **94**(20), 208001.
- Bottke, W. F., Nolan, M. C., Greenberg, R., and Kolvoord, R. A. (1994). Velocity distributions among colliding asteroids. *Icarus*, **107**, 255–268.
- Bottke, W. F., Durda, D. D., Nesvorný, D., Jedicke, R., Morbidelli, A., Vokrouhlický, D., and Levison, H. F. (2005). Linking the collisional history of the main asteroid belt to its dynamical excitation and depletion. *Icarus*, **179**, 63–94.
- Brucks, A., Arndt, T., Ottino, J. M., and Lueptow, R. M. (2007). Behavior of flowing granular materials under variable g . *Physical Review E*, **75**(3), 032301.
- Carrigy, M. A. (1970). Experiments on the Angles of Repose of Granular Materials. *Sedimentology*, **14**, 147–158.
- Chandrasekhar, S. (1969). *Ellipsoidal figures of equilibrium*.
- Chapman, C. R. (1972). *Surface Properties of Asteroids*. Ph.D. thesis, Massachusetts Institute of Technology.
- Chapman, C. R. (1976). Asteroids as meteorite parent-bodies - The astronomical perspective. *Geochim. Cosmochim. Acta*, **40**, 701–719.
- Chapman, C. R. (2004). Space Weathering of Asteroid Surfaces. *Annual Review of Earth and Planetary Sciences*, **32**, 539–567.
- Cintala, M. J., Berthoud, L., and Hörz, F. (1999). Ejection-velocity distributions from impacts into coarse-grained sand. *Meteoritics and Planetary Science*, **34**, 605–623.
- Clark, B. E., Hapke, B., Pieters, C., and Britt, D. (2002). *Asteroids III*, chapter 4.4.1 - Asteroid Space Weathering and Regolith Evolution, pages 585–599. University of Arizona Press.
- Coulomb, C. (1773). Essai sur une Application des Règles des Maximis et Minimis a quelques Problèmes de Statique Relatifs à l'Architecture. *Mémoires de Mathématique et de Physique présentés à l'Académie Royale des Sciences par divers Savans, et lûs dans ses Assemblées 1773*, **7**, pp 343–382.
- Cremonese, G., Martellato, E., Marzari, F., Kuhrt, E., Scholten, F., Preusker, F., Wünnemann, K., Borin, P., Massironi, M., Simioni, E., Ip, W., and The Osiris Team (2012). Hydrocode simulations of the largest crater on asteroid Lutetia. *Planet. Space Sci.*, **66**, 147–154.

- Daerr, A. and Douady, S. (1999a). Sensitivity of granular surface flows to preparation. *EPL (Europhysics Letters)*, **47**, 324–330.
- Daerr, A. and Douady, S. (1999b). Two types of avalanche behaviour in granular media. *Nature*, **399**, 241–243.
- Davis, D. R., Durda, D. D., Marzari, F., Campo Bagatin, A., and Gil-Hutton, R. (2002). *Asteriods III*, chapter 4.2.8 - Collisional Evolution of Small-Body Populations, pages 545–558. University of Arizona Press.
- De Sanctis, M. C., Ammannito, E., Capria, M. T., Tosi, F., Capaccioni, F., Zambon, F., Carraro, F., Fonte, S., Frigeri, A., Jaumann, R., Magni, G., Marchi, S., McCord, T. B., McFadden, L. A., McSween, H. Y., Mittlefehldt, D. W., Nathues, A., Palomba, E., Pieters, C. M., Raymond, C. A., Russell, C. T., Toplis, M. J., and Turrini, D. (2012). Spectroscopic Characterization of Mineralogy and Its Diversity Across Vesta. *Science*, **336**, 697–.
- Delannay, R., Louge, M., Richard, P., Taberlet, N., and Valance, A. (2007). Towards a theoretical picture of dense granular flows down inclines. *Nature Materials*, **6**, 99–108.
- Delbo, M., Libourel, G., Wilkerson, J., Murdoch, N., Michel, P., Ramesh, K. T., Ganino, C., Verati, C., and Marchi, S. (2014). Thermal fatigue as the origin of regolith on small asteroids. *Nature*, **508**, 233–236.
- Dollfus, A. (1971). Physical Studies of Asteroids by Polarization of the Light. *NASA Special Publication*, **267**, 95–116.
- Domokos, A., Bell, J. F., Brown, P., Lemmon, M. T., Suggs, R., Vaubaillon, J., and Cooke, W. (2007). Measurement of the meteoroid flux at Mars. *Icarus*, **191**, 141–150.
- Dury, C. M., Ristow, G. H., Moss, J. L., and Nakagawa, M. (1998). Boundary effects on the angle of repose in rotating cylinders. *Phys. Rev. E*, **57**, 4491–4497.
- Evesque, P. and Rajchenbach, J. (1989). Instability in a sand heap. *Physical Review Letters*, **62**, 44–46.
- Fairbridge, R. W. (1967). *Encyclopedia of atmospheric sciences and astrogeology*.
- Farinella, P. and Davis, D. R. (1992). Collision rates and impact velocities in the Main Asteroid Belt. *Icarus*, **97**, 111–123.
- Félix, G. and Thomas, N. (2004). Evidence of two effects in the size segregation process in dry granular media. *Phys. Rev. E*, **70**(5), 051307.
- Forterre, Y. and Pouliquen, O. (2006). Granular Flows. *Séminaire Poincaré IX*, **1**, 1–40.
- GDR MiDi (2004). On dense granular flows. *European Physical Journal E*, **14**, 341–365.
- Glassmeier, K.-H., Boehnhardt, H., Koschny, D., Kührt, E., and Richter, I. (2007). *The Rosetta Mission: Flying Towards the Origin of the Solar System*, chapter 1, pages 1–20. Number 1-4. Springer-Verlag.

- Goldschmidt, H. (1852). Entdeckung eines neuen Planeten von Herrn Goldschmidt in Paris. *Astronomische Nachrichten*, **35**, 343.
- Grün, E., Zook, H. A., Fechtig, H., and Giese, R. H. (1985). Collisional balance of the meteoritic complex. *Icarus*, **62**, 244–272.
- Gulkis, S., Keihm, S., Kamp, L., Lee, S., Hartogh, P., Crovisier, J., Lellouch, E., Encrenaz, P., Bockelee-Morvan, D., Hofstadter, M., Beaudin, G., Janssen, M., Weissman, P., von Allmen, P. A., Encrenaz, T., Backus, C. R., Ip, W.-H., Schloerb, P. F., Biver, N., Spilker, T., and Mann, I. (2012). Continuum and spectroscopic observations of asteroid (21) Lutetia at millimeter and submillimeter wavelengths with the MIRO instrument on the Rosetta spacecraft. *Planet. Space Sci.*, **66**, 31–42.
- Gundlach, B. and Blum, J. (2013). A new method to determine the grain size of planetary regolith. *Icarus*, **223**, 479–492.
- Hartmann, W. K. (1978). Planet formation - Mechanism of early growth. *Icarus*, **33**, 50–61.
- Heiken, G. H., Vaniman, D. T., and French, B. M. (1991). *Lunar sourcebook - A user's guide to the moon*.
- Herschel, W. (1802). Observations on the Two Lately Discovered Celestial Bodies. *Royal Society of London Philosophical Transactions Series I*, **92**, 213–232.
- Hofmeister, P. G., Blum, J., and Heißelmann, D. (2009). The Flow Of Granular Matter Under Reduced-Gravity Conditions. In M. Nakagawa and S. Luding, editors, *American Institute of Physics Conference Series*, volume 1145 of *American Institute of Physics Conference Series*, pages 71–74.
- Hörz, F. and Schaal, R. B. (1981). Asteroidal agglutinate formation and implications for asteroidal surfaces. *Icarus*, **46**, 337–353.
- Hörz, F., Bastien, R., Borg, J., Bradley, J. P., Bridges, J. C., Brownlee, D. E., Burchell, M. J., Chi, M., Cintala, M. J., Dai, Z. R., Djouadi, Z., Dominguez, G., Economou, T. E., Fairey, S. A. J., Floss, C., Franchi, I. A., Graham, G. A., Green, S. F., Heck, P., Hoppe, P., Huth, J., Ishii, H., Kearsley, A. T., Kissel, J., Leitner, J., Leroux, H., Marhas, K., Messenger, K., Schwandt, C. S., See, T. H., Snead, C., Stadermann, F. J., Stephan, T., Stroud, R., Teslich, N., Trigo-Rodríguez, J. M., Tuzzolino, A. J., Troadec, D., Tsou, P., Warren, J., Westphal, A., Wozniakiewicz, P., Wright, I., and Zinner, E. (2006). Impact Features on Stardust: Implications for Comet 81P/Wild 2 Dust. *Science*, **314**, 1716–1719.
- Housen, K. R. and Wilkening, L. L. (1982). Regoliths on small bodies in the solar system. *Annual Review of Earth and Planetary Sciences*, **10**, 355–376.
- Housen, K. R., Wilkening, L. L., Chapman, C. R., and Greenberg, R. (1979). Asteroidal regoliths. *Icarus*, **39**, 317–351.

- Howard, K. A. (1973). Avalanche Mode of Motion: Implications from Lunar Examples. *Science*, **180**, 1052–1055.
- Hunt, M. L., Zenit, R., Campbell, C. S., and Brennen, C. E. (2002). Revisiting the 1954 suspension experiments of R. A. Bagnold. *Journal of Fluid Mechanics*, **452**, 1–24.
- Iverson, R. M., Reid, M. E., and Lahusen, R. G. (1997). Debris-Flow Mobilization from Landslides. *Annual Review of Earth and Planetary Sciences*, **25**, 85–138.
- Jerolmack, D. J., Mohrig, D., Grotzinger, J. P., Fike, D. A., and Watters, W. A. (2006). Spatial grain size sorting in eolian ripples and estimation of wind conditions on planetary surfaces: Application to Meridiani Planum, Mars. *Journal of Geophysical Research (Planets)*, **111**, E12S02.
- Jurgens, R. F. and Goldstein, R. M. (1976). Radar observations at 3.5 and 12.6 CM wavelength of asteroid 433 Eros. *Icarus*, **28**, 1–15.
- Keller, H. U., Barbieri, C., Lamy, P., Rickman, H., Rodrigo, R., Wenzel, K.-P., Sierks, H., A'Hearn, M. F., Angrilli, F., Angulo, M., Bailey, M. E., Barthol, P., Barucci, M. A., Bertaux, J.-L., Bianchini, G., Boit, J.-L., Brown, V., Burns, J. A., Büttner, I., Castro, J. M., Cremonese, G., Curdt, W., da Deppo, V., Debei, S., de Cecco, M., Dohlen, K., Fornasier, S., Fulle, M., Germerott, D., Gliem, F., Guizzo, G. P., Hviid, S. F., Ip, W.-H., Jorda, L., Koschny, D., Kramm, J. R., Kührt, E., Küppers, M., Lara, L. M., Llebaria, A., López, A., López-Jimenez, A., López-Moreno, J., Meller, R., Michalik, H., Michelena, M. D., Müller, R., Naletto, G., Origné, A., Parzianello, G., Pertile, M., Quintana, C., Ragazzoni, R., Ramous, P., Reiche, K.-U., Reina, M., Rodríguez, J., Rousset, G., Sabau, L., Sanz, A., Sivan, J.-P., Stöckner, K., Tabero, J., Telljohann, U., Thomas, N., Timon, V., Tomasch, G., Wittrock, T., and Zaccariotto, M. (2007). OSIRIS The Scientific Camera System Onboard Rosetta. *Space Sci. Rev.*, **128**, 433–506.
- Keller, H. U., Barbieri, C., Koschny, D., Lamy, P., Rickman, H., Rodrigo, R., Sierks, H., A'Hearn, M. F., Angrilli, F., Barucci, M. A., Bertaux, J.-L., Cremonese, G., Da Deppo, V., Davidsson, B., De Cecco, M., Debei, S., Fornasier, S., Fulle, M., Groussin, O., Gutierrez, P. J., Hviid, S. F., Ip, W.-H., Jorda, L., Knollenberg, J., Kramm, J. R., Kührt, E., Küppers, M., Lara, L.-M., Lazzarin, M., Moreno, J. L., Marzari, F., Michalik, H., Naletto, G., Sabau, L., Thomas, N., Wenzel, K.-P., Bertini, I., Besse, S., Ferri, F., Kaasalainen, M., Lowry, S., Marchi, S., Mottola, S., Sabolo, W., Schröder, S. E., Spjuth, S., and Vernazza, P. (2010). E-Type Asteroid (2867) Steins as Imaged by OSIRIS on Board Rosetta. *Science*, **327**, 190–193.
- Kelley, M. S., Vilas, F., Gaffey, M. J., and Abell, P. A. (2003). Quantified mineralogical evidence for a common origin of 1929 Kollaa with 4 Vesta and the HED meteorites. *Icarus*, **165**, 215–218.
- Kleinhans, M. G., Markies, H., de Vet, S. J., in't Veld, A. C., and Postema, F. N. (2011). Static and dynamic angles of repose in loose granular materials under reduced gravity. *Journal of Geophysical Research (Planets)*, **116**, 11004.

Bibliography

- Konopliv, A. S., Asmar, S. W., Park, R. S., Bills, B. G., Centinello, F., Chamberlin, A. B., Ermakov, A., Gaskell, R. W., Rambaux, N., Raymond, C. A., Russell, C. T., Smith, D. E., Tricarico, P., and Zuber, M. T. (2013). The Vesta gravity field, spin pole and rotation period, landmark positions, and ephemeris from the Dawn tracking and optical data. *Icarus*, (In press).
- Krasinsky, G. A., Pitjeva, E. V., Vasilyev, M. V., and Yagudina, E. I. (2002). Hidden Mass in the Asteroid Belt. *Icarus*, **158**, 98–105.
- Kudrolli, A. (2004). Size separation in vibrated granular matter. *Reports on Progress in Physics*, **67**, 209–247.
- Küppers, M., Moissl, R., Vincent, J.-B., Besse, S., Hviid, S. F., Carry, B., Grieger, B., Sierks, H., Keller, H. U., Marchi, S., and OSIRIS Team (2012). Boulders on Lutetia. *Planet. Space Sci.*, **66**, 71–78.
- Lardner, D. (1867). *Handbook of Astronomy*. James Walton, London.
- Lee, L.-H. (1995). Adhesion and cohesion mechanisms of lunar dust on the moon's surface. *Journal of Adhesion Science and Technology*, **9**, 1103–1124.
- Lee, P. (1996). Dust Levitation on Asteroids. *Icarus*, **124**, 181–194.
- Lee, P. C.-C. (1997). *Physical Properties and Processing of Asteroid Regoliths and Interiors*. Ph.D. thesis, Cornell University.
- Lowry, S. C., Fitzsimmons, A., Pravec, P., Vokrouhlický, D., Boehnhardt, H., Taylor, P. A., Margot, J.-L., Galád, A., Irwin, M., Irwin, J., and Kusnirák, P. (2007). Direct Detection of the Asteroidal YORP Effect. *Science*, **316**, 272–274.
- Marchi, S., Mottola, S., Cremonese, G., Massironi, M., and Martellato, E. (2009). A New Chronology for the Moon and Mercury. *AJ*, **137**, 4936–4948.
- Marchi, S., Massironi, M., Vincent, J.-B., Morbidelli, A., Mottola, S., Marzari, F., Küppers, M., Besse, S., Thomas, N., Barbieri, C., Naletto, G., and Sierks, H. (2012). The cratering history of asteroid (21) Lutetia. *Planet. Space Sci.*, **66**, 87–95.
- Massironi, M., Marchi, S., Pajola, M., Snodgrass, C., Thomas, N., Tubiana, C., Baptiste Vincent, J., Cremonese, G., da Deppo, V., Ferri, F., Magrin, S., Sierks, H., Barbieri, C., Lamy, P., Rickman, H., Rodrigo, R., Koschny, D., and Osiris Team (2012). Geological map and stratigraphy of asteroid 21 Lutetia. *Planet. Space Sci.*, **66**, 125–136.
- Matson, D. L., Johnson, T. V., and Veeder, G. J. (1977). Soil maturity and planetary regoliths - The Moon, Mercury, and the asteroids. In R. B. Merrill, editor, *Lunar and Planetary Science Conference Proceedings*, volume 8 of *Lunar and Planetary Science Conference Proceedings*, pages 1001–1011.
- McSween, H. Y. and Stolper, E. (1980). Basaltic meteorites. *Scientific American*, **242**, 54–63.

- Mehta, A. and Barker, G. C. (1994). The dynamics of sand. *Reports on Progress in Physics*, **57**, 383–416.
- Melosh, H. J., editor (1989). *Impact cratering: A geologic process*. Oxford University Press.
- Miyamoto, H., Yano, H., Scheeres, D. J., Abe, S., Barnouin-Jha, O., Cheng, A. F., Demura, H., Gaskell, R. W., Hirata, N., Ishiguro, M., Michikami, T., Nakamura, A. M., Nakamura, R., Saito, J., and Sasaki, S. (2007). Regolith Migration and Sorting on Asteroid Itokawa. *Science*, **316**, 1011–1014.
- Möhlmann, D. (1994). Surface regolith and environment of comets. *Planet. Space Sci.*, **42**, 933–937.
- Morbidelli, A., Bottke, W. F., Nesvorný, D., and Levison, H. F. (2009). Asteroids were born big. *Icarus*, **204**, 558–573.
- Morbidelli, A., Brasser, R., Gomes, R., Levison, H. F., and Tsiganis, K. (2010). Evidence from the Asteroid Belt for a Violent Past Evolution of Jupiter’s Orbit. *AJ*, **140**, 1391–1401.
- Morbidelli, A., Lunine, J. I., O’Brien, D. P., Raymond, S. N., and Walsh, K. J. (2012). Building Terrestrial Planets. *Annual Review of Earth and Planetary Sciences*, **40**, 251–275.
- Morris, R. V., Golden, D. C., Bell, III, J. F., Lauer, Jr., H. V., and Adams, J. B. (1993). Pigmenting agents in Martian soils - Inferences from spectral, Moessbauer, and magnetic properties of nanophase and other iron oxides in Hawaiian palagonitic soil PN-9. *Geochimica et Cosmochimica Acta*, **57**, 4597–4609.
- Murdin, P., editor (2001). *Encyclopedia of astronomy and astrophysics*. Nature Publishing Group.
- Onose, N. and Fujiwara, A. (2004). Mass-velocity distributions of fragments in oblique impact cratering on gypsum. *Meteoritics and Planetary Science*, **39**, 321–331.
- Ottino, J. M. and Khakhar, D. V. (2000). Mixing and Segregation of Granular Materials. *Annual Review of Fluid Mechanics*, **32**, 55–91.
- Pätzold, M., Andert, T. P., Ansmar, S. W., Anderson, J. D., Barriot, J.-P., Bird, M. K., Häusler, B., Hahn, M., Tellmann, S., Sierks, H., Lamy, P., and Weiss, B. P. (2011). Asteroid 21 Lutetia: Low Mass, High Density. *Science*, **334**, 491–492.
- Piazzi, J. (1802). *Della scoperta del nuovo pianeta Cerere Ferdinanda*. Nella Stamperia Reale.
- Pieters, C. M., Taylor, L. A., Noble, S. K., Keller, L. P., Hapke, B., Morris, R. V., Allen, C. C., McKay, D. S., and Wentworth, S. (2000). Space weathering on airless bodies: Resolving a mystery with lunar samples. *Meteoritics and Planetary Science*, **35**, 1101–1107.

- Preusker, F., Scholten, F., Knollenberg, J., Kührt, E., Matz, K.-D., Mottola, S., Roatsch, T., and Thomas, N. (2012). The northern hemisphere of asteroid (21) Lutetia topography and orthoimages from Rosetta OSIRIS NAC image data. *Planet. Space Sci.*, **66**, 54–63.
- Quaide, W. L. and Oberbeck, V. R. (1968). Thickness Determinations of the Lunar Surface Layer from Lunar Impact Craters. *J. Geophys. Res.*, **73**, 5247–5270.
- Reynolds, O. (1885). On the Dilatancy of Media composed of Rigid Particles in Contact. *The London, Edinburgh, and Dublin Philosophical Magazine and Journal of Science*, **5**, 469–481.
- Rimas Vaišnys, J. and Pilbeam, C. C. (1975). Mechanical Properties of Granular Media. *Annual Review of Earth and Planetary Sciences*, **3**, 343–360.
- Rubincam, D. P. (2000). Radiative Spin-up and Spin-down of Small Asteroids. *Icarus*, **148**, 2–11.
- Russell, C. T., Raymond, C. A., Coradini, A., McSween, H. Y., Zuber, M. T., Nathues, A., De Sanctis, M. C., Jaumann, R., Konopliv, A. S., Preusker, F., Asmar, S. W., Park, R. S., Gaskell, R., Keller, H. U., Mottola, S., Roatsch, T., Scully, J. E. C., Smith, D. E., Tricarico, P., Toplis, M. J., Christensen, U. R., Feldman, W. C., Lawrence, D. J., McCoy, T. J., Prettyman, T. H., Reedy, R. C., Sykes, M. E., and Titus, T. N. (2012). Dawn at Vesta: Testing the Protoplanetary Paradigm. *Science*, **336**, 684–.
- Schulz, R. (2012). The Rosetta mission - Exploring solar system formation. *Planetary and Space Science*, **66**, 1.
- Schulz, R., Sierks, H., Küppers, M., and Accomazzo, A. (2012). Rosetta fly-by at asteroid (21) Lutetia: An overview. *Planet. Space Sci.*, **66**, 2–8.
- Schwehm, G. and Schulz, R. (1999). Rosetta Goes to Comet Wirtanen. *Space Sci. Rev.*, **90**, 313–319.
- Shi, X., Willner, K., and Oberst, J. (2013). Evolution of Phobos' Orbit, Tidal Forces, Dynamical Topography, and Related Surface Modification Processes. In *Lunar and Planetary Science Conference*, volume 44 of *Lunar and Planetary Science Conference*, page 1889.
- Sierks, H., Lamy, P., Barbieri, C., Koschny, D., Rickman, H., Rodrigo, R., A'Hearn, M. F., Angrilli, F., Barucci, M. A., Bertaux, J.-L., Bertini, I., Besse, S., Carry, B., Cremonese, G., Da Deppo, V., Davidsson, B., Debei, S., De Cecco, M., De Leon, J., Ferri, F., Fornasier, S., Fulle, M., Hviid, S. F., Gaskell, R. W., Groussin, O., Gutierrez, P., Ip, W., Jorda, L., Kaasalainen, M., Keller, H. U., Knollenberg, J., Kramm, R., Kührt, E., Küppers, M., Lara, L., Lazzarin, M., Leyrat, C., Moreno, J. J. L., Magrin, S., Marchi, S., Marzari, F., Massironi, M., Michalik, H., Moissl, R., Naletto, G., Preusker, F., Sabau, L., Sabolo, W., Scholten, F., Snodgrass, C., Thomas, N., Tubiana, C., Vernazza, P., Vincent, J.-B., Wenzel, K.-P., Andert, T., Pätzold, M., and Weiss, B. P. (2011). Images of Asteroid 21 Lutetia: A Remnant Planetesimal from the Early Solar System. *Science*, **334**, 487–490.

- Stöffler, D., Gault, D. E., Wedekind, J., and Polkowski, G. (1975). Experimental hypervelocity impact into quartz sand - Distribution and shock metamorphism of ejecta. *J. Geophys. Res.*, **80**, 4062–4077.
- Sullivan, R., Thomas, P., Veverka, J., Malin, M., and Edgett, K. S. (2001). Mass movement slope streaks imaged by the Mars Orbiter Camera. *J. Geophys. Res.*, **106**, 23607–23634.
- Sullivan, R. J., Thomas, P. C., Murchie, S. L., and Robinson, M. S. (2002). *Asteroids III*, chapter 3.2 - Asteroid Geology from Galileo and NEAR Shoemaker Data, pages 331–350. University of Arizona Press.
- Tedesco, E. F. and Desert, F.-X. (2002). The Infrared Space Observatory Deep Asteroid Search. *AJ*, **123**, 2070–2082.
- Thomas, N., Barbieri, C., Keller, H. U., Lamy, P., Rickman, H., Rodrigo, R., Sierks, H., Wenzel, K. P., Cremonese, G., Jorda, L., Küppers, M., Marchi, S., Marzari, F., Masironi, M., Preusker, F., Scholten, F., Stephan, K., Barucci, M. A., Besse, S., El-Maarry, M. R., Fornasier, S., Groussin, O., Hviid, S. F., Koschny, D., Kührt, E., Martellato, E., Moissl, R., Snodgrass, C., Tubiana, C., and Vincent, J.-B. (2012). The geomorphology of (21) Lutetia: Results from the OSIRIS imaging system onboard ESA's Rosetta spacecraft. *Planet. Space Sci.*, **66**, 96–124.
- Thomas, P. C., Veverka, J., Sullivan, R., Simonelli, D. P., Malin, M. C., Caplinger, M., Hartmann, W. K., and James, P. B. (2000). Phobos: Regolith and ejecta blocks investigated with Mars Orbiter Camera images. *J. Geophys. Res.*, **105**, 15091–15106.
- Trujillo, L., Peniche, F., and Jia, X. (2011). *Multiple Scattering of Elastic Waves in Granular Media: Theory and Experiments*, chapter 5, pages 127–152. InTech.
- Veverka, J., Belton, M., Klaasen, K., and Chapman, C. (1994). Galileo's Encounter with 951 Gaspra: Overview. *Icarus*, **107**, 2–17.
- Veverka, J., Thomas, P. C., Robinson, M., Murchie, S., Chapman, C., Bell, M., Harch, A., Merline, W. J., Bell, J. F., Bussey, B., Carcich, B., Cheng, A., Clark, B., Domingue, D., Dunham, D., Farquhar, R., Gaffey, M. J., Hawkins, E., Izenberg, N., Joseph, J., Kirk, R., Li, H., Lucey, P., Malin, M., McFadden, L., Miller, J. K., Owen, W. M., Peterson, C., Prockter, L., Warren, J., Wellnitz, D., Williams, B. G., and Yeomans, D. K. (2001a). Imaging of Small-Scale Features on 433 Eros from NEAR: Evidence for a Complex Regolith. *Science*, **292**, 484–488.
- Veverka, J., Farquhar, B., Robinson, M., Thomas, P., Murchie, S., Harch, A., Antreasian, P. G., Chesley, S. R., Miller, J. K., Owen, W. M., Williams, B. G., Yeomans, D., Dunham, D., Heyler, G., Holdridge, M., Nelson, R. L., Whittenburg, K. E., Ray, J. C., Carcich, B., Cheng, A., Chapman, C., Bell, J. F., Bell, M., Bussey, B., Clark, B., Domingue, D., Gaffey, M. J., Hawkins, E., Izenberg, N., Joseph, J., Kirk, R., Lucey, P., Malin, M., McFadden, L., Merline, W. J., Peterson, C., Prockter, L., Warren, J., and Wellnitz, D. (2001b). The landing of the NEAR-Shoemaker spacecraft on asteroid 433 Eros. *Nature*, **413**, 390–393.

- Vincent, J.-B., Besse, S., Marchi, S., Sierks, H., Massironi, M., and Osiris Team (2012). Physical properties of craters on asteroid (21) Lutetia. *Planet. Space Sci.*, **66**, 79–86.
- Walton, O. R., De Moor, C. P., and Gill, K. S. (2007). Effects of gravity on cohesive behavior of fine powders: implications for processing Lunar regolith. *Granular Matter*, **9**(5), 353–363.
- Wang, Z. T. (2004). A note on the velocity of granular flow down a bumpy inclined plane. *Granular Matter*, **6**(1), 67–69.
- Weiss, B. P., Elkins-Tanton, L. T., Antonietta Barucci, M., Sierks, H., Snodgrass, C., Vincent, J.-B., Marchi, S., Weissman, P. R., Pätzold, M., Richter, I., Fulchignoni, M., Binzel, R. P., and Schulz, R. (2012). Possible evidence for partial differentiation of asteroid Lutetia from Rosetta. *Planet. Space Sci.*, **66**, 137–146.
- White, B. R. and Klein, S. P. (1990). Dynamic shear of granular material under variable gravity conditions. *AIAA Journal*, **28**, 1701–1702.
- Wieghardt, K. (1975). Experiments in Granular Flow. *Annual Review of Fluid Mechanics*, **7**, 89–114.

Publications

Conference contributions

Hofmann, M., Sierks, H. and Blum, J., *Granular flow in low gravity space environment* (poster), Rocks 'n' Stars Conference, Göttingen, October 8-11 2012

Hofmann, M., Sierks, H. and Blum, J., *Small scale impacts as trigger for an avalanche in a low gravity environment* (oral), European Planetary Science Congress EPSC 2013, University College London, UK, September 8-13, 2013

Hofmann, M., Sierks, H. and Blum, J., *Small Scale Impacts as trigger for an avalanche in a low gravity environment* (poster), European Geosciences Union General Assembly, Vienna, Austria, April 27 - May 2, 2014

Hofmann, M., Sierks, H. and Blum, J., *Small-scale impacts as a trigger for an avalanche in a low-gravity environment* (oral), Asteroids Comets Meteors 2014, Helsinki, June 30 - July 5, 2014

Acknowledgements

There are so many people that helped me in the past three and a half years and to whom I want to say “Thank you!”.

I want to thank my supervisors Holger Sierks at MPS and Jürgen Blum at TU Braunschweig. Both of them had tremendous impact (Ba Dum Tss) on the work I have been doing. Long and interesting discussions with them helped me to bring my work into the shape that the interested reader now has the pleasure to enjoy.

I want to extend another special “Thank you” to Jürgen Blum for obtaining the funding for my campaign at the ZARM droptower, allowing me to use his lab for additional measurements and inviting me to the Retreat in Bad Schandau.

I thank Prof. Jürgen Oberst for being my second referee and a member of my Promotionskomitee and Prof. Andreas Hördt for being the third member of my committee.

I want to thank the International Max Planck Research School (IMPRS) for Solar System Science at the University of Göttingen for funding my research. Special gratitude I want to express towards both, the former coordinator of the school, the late Dieter Schmitt, and the current one, Sonja Schuh, for helping me in any matter that might have occurred; be it the PhD itself or just stuff.

I received a lot of help from a lot of people at TU Braunschweig when I was preparing and conducting my experiments: Ingo von Borstel who was my go-to guy for questions about everything. Stefan Kothe and Eike Beitz who helped me with the design of parts of my experimental setup. Daniel Heißelmann, Carsten Güttler (now at MPS) and Bastian Gundlach with whom I had very fruitful discussions. And I almost forgot to mention my intern, whom I supervised for half a day during my stay in Braunschweig and whose name I have sadly already forgotten (Stichwort: Personalverantwortung!).

I want to express my gratitude towards Jean-Baptiste Vincent, Nilda Oklay and Cecilia Tubiana, all of whom put a lot of effort into helping me when I had scientific questions or trouble with my software.

Jan Siemer, Fred Oetken and Torsten Lutz at ZARM in Bremen helped me a great deal during my stay there. In a tremendous group effort (I helped a little bit) we managed to finish the construction of my experiment and we were even able fly it! Holla die Waldfee!

I also want to thank our group secretary Fee von Saltzwedel because she did not only helped me organizing business trips and such but also was a good conversationalist during the time we shared an office.

Kok Leng Yeo, who started his PhD at the same time as I, is not only my flat mate but also a very good friend. One who always had an open ear for me and helped me out of trouble on one or another occasion.

My office mates Sebastian Höfner and Jakob Deller deserve a special “Thank you” for being the great people that they are. We had a good time in London and Helsinki although

Curriculum Vitae

Personal Information

Name	Marc Hofmann
Date of birth	29.04.1986
Place of birth	Pinneberg, Germany
Nationality	German

Education

2011 - 2014	Phd student, International Max Planck Research School for Solar System Science at the University of Göttingen, Max-Planck-Institut für Sonnensystemforschung, Göttingen, Germany
2010	M.Sc. (Diplom) in Physics, University of Bonn, Bonn, Germany
2005 - 2010	Study of Physics, University of Bonn, Bonn, Germany

Appointments

2009 - 2010	Student assistant, University of Bonn, Bonn, Germany
2009	Teaching assistant, University of Bonn, Bonn, Germany
2009	Student assistant, University of Bonn, Bonn, Germany

Additional information

Linguistic knowledge	German (native), English (fluent), French (basic)
Computer Skills	Usage of Windows and Linux systems, Proficient in Office applications, IDL programming